Title
From Forcing to Dissipation : Kinetic and Available Potential Energy Pathways in Idealized Models of Ocean Circulation

Author
Barkan, Roy

Publication Date
2015

UNIVERSITY OF CALIFORNIA, SAN DIEGO

From Forcing to Dissipation: Kinetic and Available Potential Energy Pathways in Idealized Models of Ocean Circulation

A dissertation submitted in partial satisfaction of the
requirements for the degree
Doctor of Philosophy

in

Oceanography

by

Roy Barkan

Committee in charge:

Kraig B. Winters, Chair
Stefan G. Llewellyn Smith, Co-Chair
Paola Cessi
Rick Salmon
Sutanu Sarkar
William R. Young

2015

The dissertation of Roy Barkan is approved, and it is acceptable in quality and form for publication on microfilm and electronically:

Co-Chair

Chair

University of California, San Diego

2015

DEDICATION

For My Parents. Who showed me the way.
For Limor. Who followed me across the globe.
For Emma. May I allow you the freedom to choose your own path in life.

TABLE OF CONTENTS

LIST OF FIGURES

LIST OF TABLES

ACKNOWLEDGEMENTS

I would like to begin by thanking my parents for letting me make my own choices from a very young age. Despite the great geographical distance you've made the effort countless times to fly across the globe, only to make me feel home far away from home.

Next, I would like to thank my wife for leaving everything she had back in Israel and moving half way across the world just so I can study ocean eddies. I admire you for the strength you have acquired and the enthusiasm you have maintained through the hard times and most importantly for always staying by my side.

Thank you Kraig Winters for allowing me the freedom to choose my own path throughout the course of my PhD. Thank you for providing guidance and being patient when things were not going smoothly. Thank you Stefan Llewellyn-Smith for for supporting me all these years and for being so constructive in evaluating my research progress.

I would like to thank my committee members Paola Cessi, Sutanu Sarkar, Rick Salmon, and Bill Young. You have all made a huge contribution to my thesis. Paola, thanks a lot for the time spent and for always being so critical. The path I have chosen in my research is highly influenced by our meetings. Rick, you are an inspiration to me. I wish I could be such a creative scientist one day. Bill, every time I leave your office I feel smarter. The way you approach problems is truly a work of art.

Thanks to Mathew Alford, George Carnevale, Jennifer McKinnon and Lynne Talley for providing great insight into my work.

Thanks to my PO class. Sam Billheimer, Magdalena Carranza, Andrew Delman, Kai Hally-Rosendahl, Bonnie Ludka, Ruth Musgrave, Nick Pizzo, Caitlin Whalen, Uriel Zajaczkovski. I have probably learned just as much from you guys as from the professors. Sam and Nick thanks for countless surf/beer sessions. Ruth and Uri thanks for awesome dinners and camping trips.

Thanks to the basement people: Sean Crosby, Timu Gallien, Kai Hally-Rosendahl, Nirnimesh Kumar, Bonnie Ludka, Greg Sinnet, Matt Spydell, and

Ata Sunada for lots of discussions on science and waves. Greg you have been an awesome office mate!

And finally, thanks to all the SIO Community for making Scrips such a fantastic place to study.

Chapters 2, 3 and 4 of the dissertation have been published in peer reviewed journals. Chapter 2 is published in its entirety in:

- Winters, K. B. and **Barkan, R.** (2013). Available potential energy density for Boussinesq fluid flow. *J. Fluid Mech.*, 714, 476-488.

Chapter 3 has been published in its entirety in:

- **Barkan, R.**, Winters, K. B., and Llewellyn Smith, S. G. (2013). Rotating Horizontal Convection. *J. Fluid Mech.*, 723, 556-586.

Chapter 4 has been published in its entirety in:

- **Barkan, R.**, Winters, K. B., and Llewellyn Smith, S. G. (2015). Energy Cascades and Loss of Balance in a Re-entrant Channel Forced by Wind Stress and Buoyancy Fluxes. *J. Phys. Oceanogr.*, 45, 272-293.

VITA

2007	B.S. in Geophysics and Biology, Tel Aviv University, Tel Aviv, Israel
2010	M.Sc. in Oceanography, University of California, San Diego
2015	Ph.D. in Oceanography, University of California, San Diego

PUBLICATIONS

Barkan, R., Winters, K. B., and Llewellyn Smith, S. G. (2015). Energy Cascades and Loss of Balance in a Re-entrant Channel Forced by Wind Stress and Buoyancy Fluxes. *J. Phys. Oceanogr.*, 45, 272-293.

Barkan, R., Winters, K. B., and Llewellyn Smith, S. G. (2013). Rotating Horizontal Convection. *J. Fluid Mech.*, 723, 556-586.

Winters, K. B. and **Barkan, R.** (2013). Available potential energy density for Boussinesq fluid flow. *J. Fluid Mech.*, 714, 476-488.

Barkan, R., and ten Brink, U. (2010). Tsunami simulations of the 1867 Virgin Islands earthquake: Constraints on epicenter location and fault parameters. *Bulletin of Seismological Society of America.*, 100, 995-1009.

Zvuloni, A., Artzy, Y.,Stone, L., Kramarsky, E., **Barkan, R.**, Kushmaro, A., and Loya, Y. (2009). Spatio-Temporal transmission patterns of Black-Band Disease in a coral community. *PLoSONE.*, 4, 1-10.

ten-Brink, U., **Barkan, R.**, Andrews, B.D., and Chaytor, J.D. (2010). Size distribution and failure initiation of submarine landslides and subaerial landslides. *Earth and Planetary Science Letters.*, 287, 31-42.

Barkan, R., ten Brink, U., and Lin, J. (2009). Far field tsunami simulations of the 1755 Lisbon earthquake: Implications for tsunami hazard to the U.S East Coast and the Caribbean. *J. Marine Geology.*, 264, 109-122.

ABSTRACT OF THE DISSERTATION

From Forcing to Dissipation: Kinetic and Available Potential Energy Pathways in Idealized Models of Ocean Circulation

by

Roy Barkan

Doctor of Philosophy in Oceanography

University of California, San Diego, 2015

Kraig B. Winters, Chair
Stefan G. Llewellyn Smith, Co-Chair

The general circulation of the ocean is forced by surface fluxes of momentum, heat, and freshwater at basin scales. The kinetic (E_k) and available potential (E_a) energy sources associated with these external forces drive a circulation which exhibits flow features that vary on a wide range of spatial and temporal scales. Understanding how the different forcing mechanisms lead to the observed large-scale ocean circulation patterns and to what degree do the various smaller scale processes modify them have been long standing problems for oceanographers. The purpose of this dissertation is, first, to examine the role of buoyancy forcing and the associated E_a source in maintaining the observed meridional overturning circulation (MOC) and overall thermal structure of the ocean and, second, to understand the possible E_k pathways in the ocean, from forcing to dissipation scales.

We first derive an exact positive definite available potential energy density $\mathcal{E}_a$ that is connected to well-known temporal evolution equations for both E_k and E_a. $\mathcal{E}_a$ is easily linked to the dynamics of a fluid flow and can be interpreted in a similar manner to the commonly used E_k density. Next, we apply the $\mathcal{E}_a$ framework to the horizontal convection (HC) model, a simple physical construct used to investigate the role of buoyancy forcing in driving the MOC. The basic HC model refers to the flow resulting from a buoyancy variation imposed along a horizontal boundary of a fluid. We study and quantify the effects of rotation on three-dimensional HC with respect to the overall thermal structure and buoyancy transport mechanisms, the overturning circulation, and the flow energetics. Our numerical results show that the steady state solution of rotating horizontal convection (RHC) is substantially different that that of HC. In RHC geostrophic eddies dominate the vertical and horizontal buoyancy fluxes as well as the energy reservoirs and exchange terms, leading to enhanced stratification and a deeper thermal boundary layer compared with HC. Finally, we examine the kinetic energy pathways and cascades in the RHC model as well as in a model externally forced by wind stress. In both models the simulated flow is allowed to reach a statistical steady state at which point it exhibits both a forward and an inverse E_k cascade. We show that the E_k of the 'balanced' geostrophic eddies (EKE) is dissipated preferentially at small scales near the surface via frontal instabilities associated with 'loss of balance' and a forward energy cascade rather than by bottom drag after an inverse energy cascade, typical of *geostrophically turbulent* flows. This is true both with and without forcing by the wind. These results suggest that submesoscale instabilities near the ocean surface could efficiently dissipate EKE, independent of boundary effects.

Chapter 1

Introduction

The general circulation of the oceans, forced by surface fluxes of momentum, heat, and freshwater at basin scales, encompasses a broad range of processes that vary over a wide range of spatial and temporal scales.

At very large scales, phenomena such as the meridional overturning circulation, which stretches over thousands of kilometers and transports about 30 Sv ($1Sv = 10^6 m^3/s$) of water and 2 PW ($PW = 1 \times 10^{15}\, W$) of heat with relatively small variations over the course of decades. At very small scales, isotropic, three-dimensional turbulent processes which occur over millimeter scales and vary rapidly on the order of seconds. In between are a range of fluid motions such as large-scale ocean currents with horizontal spatial scales of $O(1000)$ km and time scales of years; *geostrophicially turbulent* mesoscale eddies which are tens to a few hundred kilometers in diameter and have lifetimes of a few months to a year; and sub-mesoscale oceanic fronts, which are a few kilometers wide and vary on time scales of days.

In addition, various types of wave motions abound in the world oceans. Synoptic-scale, slowly-evolving Rossby waves are on one end of the spectrum and small-scale, fast-evolving, surface gravity waves are on the other. In between are internal gravity waves (IGWs) with spatial scales ranging between meters to tens of kilometers and nominal frequencies ranging between N and f, with N being the buoyancy frequency of $O(10^{-2}\, s^{-1})$ and f the vertical component of the Coriolis force of $O(10^{-4}\, s^{-1})$ at mid-latitudes.

Oceanographers have sought to understand for a long time how the different forcing mechanisms lead to the observed large-scale ocean circulation patterns and overall buoyancy structure, and to what degree do the various smaller scale processes need to be accounted for in order to correctly predict the global transports of momentum, energy and buoyancy.

In this thesis, a rather idealized approach is taken, using lab-scale process studies or 'thought experiments' we try to shed some light on the following aspects of the general problem:

i. To what degree can buoyancy forcing alone drive an overturning circulation?

ii. To what degree can buoyancy forcing alone produce a thermocline and deep stratification?

iii. What are the most important mechanisms by which buoyancy is being transported?

iv. What are the kinetic and available potential energy pathways, from forcing to dissipation, under generic wind and buoyancy forcing?

v. How important are submesoscale processes to the dissipation of kinetic energy?

1.1 Background

1.1.1 Horizontal convection, the meridional overturning circulation and the role of buoyancy forcing

The oceanic meridional overturning circulation (MOC), a measure of the zonally integrated poleward-bound mass transport, has become representative of ocean circulation and its role in climate change (see *Wunsch and Heimbach* 2012 and references therein). The relative roles of buoyancy forces, wind stress, tides and even biology in maintaining the MOC have been debated upon for more than a century.

In the early 1900s *Sandström* (1908, 1916) conducted a series of laboratory experiments and speculated that

> *"A circulation [in the ocean] can develop from thermal [buoyancy] causes only if the [geopotential] level of the heat [positively buoyant] source lies below the [geopotential] level of the cold [negatively buoyant] source."*

This statement, often referred to as *Sandstörm's "theorem"*, has been long recognized as false taken at face value, because in the "proof" Sandstörm did not account for the effects of thermal diffusion (*Jeffreys*, 1925).

For much of the 1900s the MOC was often referred to as the *thermohaline* circulation because it was implicitly assumed that buoyancy differences (due to an uneven distribution of temperature and salinity) account for the observed overturning motions. The most famous of these early models for the *thermohaline* circulation is the Stomel-Arrons model (SAM) (*Stommel et al.*, 1958). In SAM the ocean is modeled as a single layer of abyssal homogeneous fluid which lies below a warmer upper layer separated by a thermocline. A localized source of mass is injected into the abyss at high latitudes, representing deep convection. Away from the localized convection region, mass is extracted from the abyssal layer by upwelling uniformly into the warmer water above it, keeping the averaged thermocline depth constant. The ocean is assumed flat-bottomed and a passive western boundary current can be invoked in order to satisfy mass conservation without affecting the interior flow.

Another simple model used to discuss the role of buoyancy forcing in driving the MOC is horizontal convection (HC). HC describes the flow resulting from a buoyancy variation imposed along a horizontal boundary of a fluid. *Rossby* (1965) performed a set of laboratory experiments of HC by differentially heating a fluid from below. Motivated by his observations at steady state, he derived scaling laws for the thermal boundary layer depth and the strength of the circulation, which suggest that in the oceanic regime HC supports a thinner thermal boundary layer and weaker circulation and abyssal stratification than those observed. These results support *Sandstörm's "theorem"* and indicate that additional physical processes and energy sources are important to obtain a better match with the oceanic regime.

In a seminal paper, *Munk* (1966) argued that if the overturning can be characterized by localized sinking and uniform upwelling, as suggested by SAM, than the vertical profile of buoyancy would be determined by the balance between the upward vertical transport and the mixing due to eddying motion following

$$w\frac{\partial b}{\partial z} = \kappa_e \frac{\partial^2 b}{\partial z^2}, \tag{1.1}$$

where the diffusion coefficient κ_e is an *eddy diffusivity.* The available knowledge of the volume of water sinking into the abyss and the extent of the deep convection regions allows for a rough estimate of the upward return velocity: $w \approx 10^{-7}\, m/s$. This implies an eddy diffusivity $\kappa_e \approx 10^{-4}\, m^2/s$. Munk hypothesized that this value is not generated by the overturning motions alone and is associated with other sources injecting energy into the ocean. He argued that the energy sources are winds and tides, creating IGW propagating into the abyss, that would then break and produce the necessary diapycnal mixing to balance the upwelling. This hypothesis suggests that the MOC is not determined by the *pushing down* of the sinking plumes in the high latitude convection regions, but rather by the *pulling up* of small scale turbulent mixing due to effects unrelated to the distribution of buoyancy. In other words, if the MOC was forced solely by buoyancy forcing as in the HC model, than the upward return velocity would be substantially smaller because it could only be balanced by the molecular diffusivity values, and so

> *"Viewed as a heat engine the ocean circulation is extraordinarily inefficient. Viewed as a mechanically driven system, it is a remarkably efficient transporter of heat energy" (Munk and Wunsch, 1998).*

For years after the *Munk* (1966) paper, oceanographers have tried to measure κ_e in the ocean to see how well it agrees with the hypothesized $10^{-4}\, m^2/s$ value. Unfortunately, observations of *eddy diffusivity* are indirect and rely heavily on a series of assumptions relating kinetic energy dissipation (ϵ), a somewhat easier quality to measure, and *eddy diffusivity* via the *Osborn* (1980) relation

$$\kappa_e = \Gamma \frac{\epsilon}{N^2}, \tag{1.2}$$

where Γ is the mixing efficiency typically taken to be ~ 0.2. Recent observations (*Whalen et al.*, 2012) show that κ_e varies over several orders of magnitudes spatially and seasonally with values ranging between $5 \times 10^{-7} - 5 \times 10^{-4}\, m^2/s$, making it difficult to validate Munk's hypothesis conclusively.

In the last two decades oceanographers have begun to realize that the Southern Ocean, particularly the Antarctic Circumpolar Current (ACC), plays a crucial role in the dynamics of the MOC. Ignoring bathymetric detail, the lack of zonal barriers and the wind forcing configuration in the ACC create an Ekman driven Eulerian-mean circulation which tends to steepen isopycnals and drive a baroclinic zonal jet. Mesoscale baroclinic eddies, which are generated via baroclinic instability of the zonal current, tend to restratify the isopycnals and oppose the Eulerian mean circulation. The resulting *residual circulation* upwells water adiabatically along isopycnals (*Marshall and Radko*, 2003). In this view, baroclinic eddies formed in the ACC have a leading order effect on the buoyancy transport of the MOC and the *residual circulation* is the relevant quantity for the ocean's effect on the climate. More importantly, these zonally-symmertric theories of the ACC suggest a completely different mechanism for the dynamics of the MOC, particularly in the Atlantic Ocean, which doesn't rely on diapycnal mixing for closure, except for a very thin surface mixed layer, (see *Marshall and Speer* 2012 and references therein).

During the last few years it has become commonpractice to divide the Atlantic MOC into an upper 'adiabatic' cell and a lower 'diabatic' one combining the two views discussed above (*Nikurashin and Vallis*, 2012). Furthermore, zonally-symmetric theories of the ACC are considered to be quite unrealistic because they ignore topographic effects as well as the Antarctic margin, both of which are now considered to be key players in the dynamics (*Thompson and Garabato*, 2014; *Thompson et al.*, 2014).

1.1.2 Energetics and the ϵ-*theorem* for horizontal convection

In order to asses the validity of the dynamical hypotheses discussed in section 1.1.1 multiple studies have attempted to use an energetic framework to gain insight into the processes governing the MOC.

The evolution equations for the volume averaged kinetic and potential energies in an ocean which is externally forced by buoyancy forcing and wind stress τ_s and under the Boussinesq approximation are (*Winters et al.*, 1995)

$$\frac{d\langle E_k\rangle}{dt} \equiv \frac{1}{V}\frac{d}{dt}\left(\frac{1}{2}\int |\boldsymbol{u}|^2\,\mathrm{d}V\right) = \langle wb\rangle - \epsilon + \frac{1}{H}\widehat{\boldsymbol{u}_s\cdot\tau_s}, \tag{1.3a}$$

$$\frac{d\langle E_p\rangle}{dt} \equiv \frac{1}{V}\frac{d}{dt}\left(\int -zb\,\mathrm{d}V\right) = -\langle wb\rangle + \frac{\kappa}{H}\Delta\widehat{b}, \tag{1.3b}$$

where $\widehat{\ }$ denotes a horizontal average, $\langle\ \rangle$ denotes a volume average, $\epsilon = \nu\langle|\boldsymbol{\nabla u}|^2\rangle$, $\Delta\widehat{b} = \widehat{b}(top) - \widehat{b}(bot)$, $\boldsymbol{u}$ is the three dimensional velocity vector (u, v, w), $\boldsymbol{u}_s$ is the horizontal velocity vector (u, v) evaluated at the surface and b is the buoyancy.

The claim that the ocean is mechanically driven relies, in part, on comparing the energy source term associated with buoyancy forcing $\kappa H^{-1}\Delta\widehat{b}$ and that associated with wind forcing $H^{-1}\widehat{\boldsymbol{u}_s\cdot\tau_s}$ and noting that in the ocean

$$O\left(\rho_0 V\frac{\kappa}{H}\Delta\widehat{b}\right) \ll O\left(\rho_0 V\frac{1}{H}\widehat{\boldsymbol{u}_s\cdot\tau_s}\right) \approx 1\,TW, \tag{1.4}$$

where V is a representative volume and ρ_0 the background density.

Paparella and Young (2002) claimed that an ocean forced solely by surface buoyancy forcing (following the HC model) cannot be turbulent. Their argument is based on combining (1.3a) and (1.3b) above and noting that, at steady state,

$$\epsilon = \frac{\kappa}{H}\Delta\widehat{b}. \tag{1.5}$$

If the buoyancy forcing is cast in terms of any surface buoyancy distribution $b_{\max}\mathcal{F}(x, y)$, then from (1.5)

$$\epsilon \leq \frac{\kappa}{H}b_{\max} = \nu\frac{b_{\max}}{\mathrm{Pr}\,H}. \tag{1.6}$$

For a fixed Prandtl number Pr, in the limit that the viscosity goes to zero so does the dissipation. This contrasts with typical turbulent flows for which the dissipation rate is set by the forcing at scales larger than those in the inertial subrange and is independent of the fluid viscosity.

In the years that followed *Paparella and Young* (2002), multiple authors (see *Hughes and Griffiths* 2008 and references therein) have shown in laboratory and numerical experiments of HC that the resulting flow may be highly unsteady, particularly in the convective plume region. Furthermore, *Scotti and White* (2011) argued, based on certain statistical properties of the velocity gradient tensor which are common to all known turbulent flows, that HC is in fact turbulent. Such studies imply that buoyancy forcing alone can drive quite an active flow

Additional arguments in favor of the importance of buoyancy forcing, discussed for example in *Hughes et al.* (2009), rely on the idea that the available potential energy E_a and not E_p is the relevant framework to evaluate the role of buoyancy forcing in the ocean. The evolution equation for the volume averaged available potential energy is (*Winters et al.*, 1995)

$$\frac{d\langle E_a\rangle}{dt} \equiv \frac{1}{V}\frac{d}{dt}\left(\int (z_* - z)b\,\mathrm{d}V\right) = -\langle wb\rangle - \kappa\left\langle \frac{dz_*}{db}|\nabla b|^2\right\rangle + \frac{\kappa}{H}\Delta\widehat{b} + \frac{\kappa}{H} z_*\widehat{(b_{top})b_z}|_{top}, \tag{1.7}$$

where $z_*(b,t)$ is the reference height in the minimum potential energy state of a fluid with buoyancy $b(\boldsymbol{x},t)$. The source term of E_a, $\kappa H^{-1} z_*\widehat{(b_{top})b_z}|_{top}$, depends on the reference profile $z_*(b,t)$ which is directly linked to the dynamics, and can be as large as $H^{-1}\widehat{\boldsymbol{u}_s\cdot\tau_s}$ in some cases. Furthermore, in a statistical steady state, combining (1.3b) and (1.7) above leads to

$$\frac{\kappa}{H} z_*\widehat{(b_{top})b_z}|_{top} = \kappa\left\langle \frac{dz_*}{db}|\nabla b|^2\right\rangle, \tag{1.8}$$

where $\kappa\langle\frac{dz_*}{db}|\nabla b|^2\rangle$ is the term associated with diabatic processes or mixing. Thus, if the closure of the MOC relies on diapycnal mixing, as suggested by *Munk* (1966), then from the balance (1.8) buoyancy forcing should play a very active role in the process.

1.1.3 What breaks the inverse kinetic energy cascade in the *geostrophically turbulent* ocean?

Understanding the driving forces and energy sources of the MOC is only one aspect of the ocean circulation's role in affecting the climate system. Being able to follow the energy pathways from the large forcing scales to the small dissipative scales is yet another. A large fraction of the kinetic energy in the ocean is stored in the mesoscale eddy field. These *geostrophic* eddies are formed primarily via baroclinc instability of large-scale ocean currents that are in approximate thermal wind balance (*Gill et al.*, 1974). These eddies are considered 'balanced' in the sense that they are in geostrophic and hydrostatic balance and the associated velocity and buoyancy fields are entirely determined by their potential vorticity (*Ford*, 1993).

Between the 1960s and 1980s scientists began to think of the dynamics of geostrophic eddies in the ocean and atmosphere using two-dimensional turbulence theories. In contrast with three-dimensional turbulence in which energy is the sole quadratic invariant, in two-dimensional turbulence the second moment of vorticity, *enstrophy*, is also conserved.[1] The conservation of enstrophy requires the kinetic energy to be transferred to larger scales and consequently, two-dimensional turbulence exhibits an *inverse energy cascade* (*Kraichnan*, 1967). *Charney* (1971) was the first to suggest the analogy between two-dimensional turbulence and the turbulent ocean and atmosphere, and suggested the term *geostrophic turbulence.* If the *geostrophicially turbulent* ocean is expected to transfer energy to larger scales yet kinetic energy dissipation is observed to take place at small scales (*Wunsch and Ferrari* 2004 and references therein) an immediate question arises:

What is the mechanism by which the inverse energy cascade of the geostrophic eddies is discontinued and a forward cascade is allowed ?

Certain processes must lead to a loss of geostrophic and/or hydrostatic balance and other fields aside from the potential vorticity are going to be required to

---

[1] In fact all vorticity moments are conserved in 2D turbulence. However only enstrophy is a quadratic invariant that is conserved triad-wise (*Salmon*, 1998).

fully understand the mechanism by which the inverse cascade is halted. This phenomenon is often referred to as '*loss of balance*' (*McWilliams and Yavneh*, 1998).

Studying '*loss of balance*' (LOB) has become feasible in recent years because computers are now able to resolve the wide range of scales required to capture both the inverse and forward energy cascades. The two main hypotheses for LOB in the ocean are (*Müller et al.*, 2005):

- *The boundary route*: Geostrophic eddies can interact with bottom topography and lose balance via a variety of turbulent boundary layer processes or by generating IGWs which will propagate to the ocean interior and break, dissipating kinetic energy in the process.

- *The instability route*: Geostrophic eddies can spontaneously develop smaller, submesoscales in the form of surface intensified fronts. These fronts are susceptible to a variety of instabilities which can lead to LOB. Secondary instabilities are then hypothesized to take place and induce kinetic energy dissipation.

The extreme challenges associated with properly observing submesoscales in the ocean leaves the LOB dilemma largely unanswered at this point in time. It is the hope that in the next few decades, high resolution satellite altimetry and the development of Lagrangian measuring devices will help shed some light into the dominant LOB mechanisms in the ocean.

1.2 Outline of the Dissertation

1.2.1 Available potential energy density

Kinetic Energy has a natural link to the dynamics of a fluid flow largely because it has a local, positive definite energy density $\mathcal{E}_k \equiv 1/2|\boldsymbol{u}|^2$ which allows for meaningful point-wise evolution equation, interpretable in a similar manner to the volume averaged evolution equation (1.3a). As discussed in section 1.1.2 it has recently been suggested that in order to investigate the role of buoyancy forcing in the MOC, E_a should be examined because it corresponds more closely to the fluid flow than E_p. However, in order for the analogy with E_k to be fully established, a positive definite available potential energy density has to be derived.

In chapter 2, we derive an exact expression for available potential energy density $\mathcal{E}_a$ in Boussinesq fluid flows that is shown explicitly to integrate to E_a in eq. (1.7). The derivation follows closely the original interpretation of available potential energy discussed by *Lorenz* (1955), which is based on energy minimization formalized in terms of an adiabatic sorting of fluid parcels. $\mathcal{E}_a$ can be used to construct spatial maps of local contributions to E_a for numerical simulations in a similar manner to the easily computable spatial maps of $\mathcal{E}_k$. Because $\mathcal{E}_a$ integrates to E_a, these maps are explicitly connected to the exact, temporal evolution equations for kinetic, and available potential energies (1.3a, 1.7).

1.2.2 The effects of rotation on horizontal convection

Although the horizontal convection model described in the works of *Sandström* (1908, 1916); *Rossby* (1965); *Hughes and Griffiths* (2008) has helped provide insight into the role of buoyancy forcing in driving the MOC it lacks the effects of rotation, a key aspect of all large scale oceanic flows. In HC buoyancy is transported in pole-to-equator cells via advection, an impossible mechanism in a rotating frame. In addition, HC doesn't include one of the most important buoyancy transport mechanisms found in the ocean, the buoyancy flux due to baroclinic eddies. We suggest that in order to study HC in an oceanic context, rapid rotation has to be included and its effects on the circulation and thermocline depth understood. The energy equations (1.3a, 1.3b, 1.7) are invariant for rotating and non-rotating HC because they don't contain f explicitly. However, in the presence of rotation the reference profile $z_*(b,t)$, discussed in section 1.1.2, is expected to change, and consequently so will the magnitude of the available potential energy source term $\kappa H^{-1} z_*(\widehat{b_{top}) b_z}|_{top}$.

In chapter 3, we study numerically the effects of rotation on three-dimensional HC and quantify the way in which rapid rotation alters the steady state solution of HC. We show how in rotating horizontal convection (RHC) baroclinic eddies dominate the vertical and horizontal buoyancy fluxes as well as the energy reservoirs and exchange terms, leading to enhanced stratification and a deeper thermal boundary layer compared with non-rotating HC. Furthermore, the statistically steady solutions exhibit characteristics of *geostrophic turbulence*, a much better representation of large-scale oceanic flows.

1.2.3 Kinetic energy pathways in a reentrant channel

In chapter 4, we focus on the kinetic energy pathways and cascades in the RHC model as well as in a model externally forced by wind stress. We choose a flat-bottomed re-entrant channel geometry and a forcing configuration that resembles that of the ACC. The simulated flow is allowed to reach a statistical steady state at which point it exhibits both a forward and an inverse energy cascade. Flow interactions with irregular bathymetry are intentionally excluded, so that bottom drag represents the sole eddy kinetic energy (EKE) sink of the *boundary route* discussed in section 1.1.3. We show that EKE is dissipated preferentially at small scales near the surface via frontal instabilities associated with LOB and a forward energy cascade rather than by bottom drag after an inverse energy cascade. This is true both with and without forcing by the wind. These results suggest that LOB caused by frontal instabilities near the ocean surface could provide an efficient mechanism by which EKE is dissipated, independent of boundary effects.

Chapter 2

Available potential energy density for Boussinesq fluid flow

An exact expression $\mathcal{E}_a$ for available potential energy density in Boussinesq fluid flows (*Roullet and Klein*, 2009; *Holliday and McIntyre*, 1981), is shown explicitly to integrate to the available potential energy E_a of *Winters et al.* (1995). $\mathcal{E}_a$ is a positive definite function of position and time consisting of two terms. The first, which is simply the indefinitely signed integrand in the *Winters et al.* (1995) definition of E_a, quantifies the expenditure or release of potential energy in the relocation of individual fluid parcels to their equilibrium height. When integrated over all parcels, this term yields the total available potential energy E_a. The second term describes the energetic consequences of the compensatory displacements necessary under the Boussinesq approximation to conserve vertical volume flux with each parcel relocation. On a point-wise basis, this term adds to the first in such a way that a positive definite contribution to E_a is guaranteed. Globally however, the second term vanishes when integrated over all fluid parcels and therefore contributes nothing to E_a. In effect, it filters the components of the first term that cancel upon integration, isolating the positive definite residuals. $\mathcal{E}_a$ can be used to construct spatial maps of local contributions to E_a for direct numerical simulations of density stratified flows. Because $\mathcal{E}_a$ integrates to E_a, these maps are explicitly connected to known, exact, temporal evolution equations for kinetic, available and background potential energies.

2.1 Introduction

Recently, *Roullet and Klein* (2009) examined a positive definite expression for available potential energy density for Boussinesq fluid flows originally proposed by *Holliday and McIntyre* (1981), combining it with the specific reference state based on energy minimization *Lorenz* (1955) formalized in terms of an adiabatic sorting of fluid parcels discussed in *Winters et al.* (1995).

Roullet and Klein (2009) note that the volume integral of the positive definite expression for energy density yields the same available potential energy E_a of *Winters et al.* (1995) for which an exact evolution equation is known. This is intriguing as the formal definition of E_a in *Winters et al.* (1995) is the volume integral of a quantity that is not sign definite but rather explicitly accumulates the expenditure or release of energy in moving individual fluid parcels from their actual positions to their equilibrium heights with respect to a globally defined reference density profile. Because the integrand is not signed definite, it cannot be understood as a local available potential energy density (see e.g. *Molemaker and McWilliams*, 2010).

The objective of this chapter is to show the relationship between the exact, positive definite available potential energy density of *Roullet and Klein* (2009) and the integrand of the available potential energy E_a defined in *Winters et al.* (1995). The positive definite energy density is reinterpreted strictly in terms of the energy released during an adiabatic repositioning of individual fluid parcels, compensated by an opposing, nonlocal transport of fluid such that the net vertical volume flux vanishes on a parcel by parcel basis. Both the volume and the density of the fluid displaced in compensation are uniquely determined by the actual height z and reference height z_* (*Winters et al* 1995; and section 2.2 below) of each fluid parcel. This interpretation allows one to discuss background potential energy, available potential energy and its local positive definite density strictly in terms of work done in displacing fluid parcels vertically in a gravitational field, a view that seems natural given the usual physical interpretation of potential energy. Though our discussion here is confined to available potential energy under the Boussinesq approximation, similar ideas apply to the mixing of potential vorticity (*Wood and McIntyre*, 2010).

In section 2.2 we consider a Boussinesq fluid with a linear equation of state and revisit briefly the definition of available potential energy E_a in a finite volume V and its interpretation in terms of an adiabatic re-sorting of infinitesimal fluid parcels. In section 2.3 we show that the expression for available potential energy density of *Roullet and Klein* (2009) can be written as the sum of two terms: the integral definition of E_a of *Winters et al.* (1995), in which the integrand is not sign-definite, and a second integral, also with a sign-indefinite integrand, that integrates identically to zero over V. This second term is described in terms of work against the background pressure force in *Holliday and McIntyre* (1981) and obtained as a difference of integrands of Casimirs in *Roullet and Klein* (2009). That it integrates to zero results from the specific property that the reference density profile is an adiabatic redistribution of fluid parcels. Here we reinterpret the work against pressure as additional gravitational work incurred in displacing fluid a small distance to make room for the repositioning of 'flattened' fluid parcels in constructing the one-dimensional reference profile. The integrands describe the two adiabatic resorting operations that, when combined, reveal the positive definite contribution to E_a on a point-wise basis. In section 2.4 we introduce the fundamental three-dimensional to one-dimensional mapping at the heart of the adiabatic resorting idea and in sections 2.5 and 2.6 we describe the closed-loop parcel exchanges and compensatory displacement operations underlying the interpretation of the positive definite integrand in terms of resorting. In section 2.7, we briefly illustrate by example the mechanics of the calculations and their utility using simulations of rotating and non-rotating horizontal convection (see e.g. *Hughes and Griffiths*, 2008). Concluding comments are given in 2.8 and a recipe for computing the reference state of minimum potential energy is given in appendix 2.9.

2.2 Available potential energy E_a

The available potential energy E_a is defined in terms of the reference profile $\rho(z_*)$ where z_* is the equilibrium height of a fluid parcel with potential density ρ:

$$E_a \equiv g \int (z - z_*)\rho \, \mathrm{d}V \,. \tag{2.1}$$

The corresponding definition for total potential energy is

$$E_p(t) \equiv g \int z\rho \, \mathrm{d}V \tag{2.2}$$

where in both expressions we take z positive upward.

As discussed in *Winters et al.* (1995), the strictly one-dimensional reference profile is defined by

$$z_*(\boldsymbol{x}, t) = \frac{1}{A} \int H[\rho(\boldsymbol{x}', t) - \rho(\boldsymbol{x}, t)] \, \mathrm{d}V' \,, \tag{2.3}$$

where H is the Heaviside step function. For a given point $(\boldsymbol{x}, t)$, the corresponding value z_* is the total volume of fluid in V with density greater than $\rho(\boldsymbol{x}, t)$, normalized by the cross section A. While it is often convenient to write z_* as an explicit function of space and time, we also note that at fixed t the function z_* has the same unique value at all points on an isopycnal surface. We can therefore regard z_* as a unique function of ρ and consider the corresponding, strictly one-dimensional function $\rho(z_*)$ (at fixed time t). This reference profile is monotonic with $\frac{\mathrm{d}\rho}{\mathrm{d}z_*} \leq 0$. The potential energy associated with the reference profile is the global minimum potential energy attainable via adiabatic leveling or sorting of the fluid parcels in V at time t. The definition of background potential energy is therefore

$$E_b \equiv g \int z_* \rho \, \mathrm{d}V \,, \tag{2.4}$$

which leads immediately to the definition (2.1) since $E_p = E_a + E_b$. Because E_b is the positive definite potential energy after adiabatic leveling it is intuitively obvious that $E_a > 0$.

That E_a is a positive definite quantity, however, is not at all obvious from the integral expression (2.1) alone. For stratified flows in general, a snapshot of the density field will capture some fluid parcels above their adiabatic equilibrium positions and others below. In particular, $(z-z_*)$ can be of either sign and the total integral represents significant cancellation of positive and negative contributions.

The sign indefiniteness of the integrand leads to some awkwardness in defining an available potential energy density directly from (2.1). What, for example, is the contribution to E_a from a particle with $(z - z_*) < 0$? The situation here is quite different than that for kinetic energy where the corresponding integrand is positive definite. Each parcel in the domain contributes an identifiable portion of the volume integrated kinetic energy and a spatial map of these contributions is intrinsically meaningful.

2.3 Available potential energy density $\mathcal{E}_a$

It would be useful to define an available potential energy density $\mathcal{E}_a$ with the following properties:

$$g \int \mathcal{E}_a(\boldsymbol{x}, t)\, \mathrm{d}V = E_a(t) \tag{2.5}$$

$$\mathcal{E}_a(\boldsymbol{x}, t) \geq 0 \;\forall\; \boldsymbol{x}, t\,. \tag{2.6}$$

Requirement (2.5) permits a precise physical interpretation of $\mathcal{E}_a$ in the context of the previously known exact evolution equations for E_a and E_b (*Winters et al.*, 1995) and their application to diagnosing the energetics of diabatic mixing. Though we will define $\mathcal{E}_a$ formally as a function of $\boldsymbol{x}$ and t, the value for a given parcel can never be a *truly* local quantity in the sense that the value for each parcel depends on the positions and densities of all other parcels via a dependence on $z_*(\rho)$. Nevertheless, with requirement (2.6), the spatial distribution of the local contributions can be examined. Such an expression would also allow, for example, for a spectral decomposition and an assessment of the scale dependence of available potential energy as in *Molemaker and McWilliams.* (2010).

We define the available potential energy density as follows:

$$\mathcal{E}_a(\boldsymbol{x}, t) \equiv (z - z_*)(\rho(\boldsymbol{x}, t) - \overline{\rho}(z, z_*)) \tag{2.7}$$

where

$$\overline{\rho}(z, z_*) = \frac{1}{(z - z_*)} \int_{z_*}^{z} \rho(z'_*)\,\mathrm{dz}'_* \,. \tag{2.8}$$

Eq. (2.7) is equivalent to Eq. (2.1) of *Roullet and Klein* (2009) when z_r in that paper is taken as z_* and ρ_r as the reference profile $\rho(z_*)$. *Roullet and Klein* (2009) also show by way of a Taylor series that, in the limit of small displacements from the reference state, (2.7) reduces to their quadratic quasi-geostrophic expression (2.5).

The first thing to note is that $\mathcal{E}_a \geq 0$, vanishing only for fluid parcels located at their equilibrium heights. Figure 2.1 shows schematically a monotonic reference profile $\rho(z_*)$ for a given flow at time t. We now consider two possibilities for the fluid parcel located at height $z = z_i$ with a density value ρ_i. In constructing the reference profile from discrete volume elements, each parcel with volume $\mathrm{dV} = \mathrm{dx\,dy\,dz}$ is first "flattened" to size $A\,dz_*$. The flattened parcels, each with thickness $dz_* = dV/A << dz$, are then stacked in order of descending density. The left panel in Figure 2.1 illustrates the case where the position of the parcel at time t is higher than it's equilibrium location $z_*(\rho_i)$. The horizontal position of the parcel is not relevant to the argument. In this case, $(z_i - z_*) > 0$ and the density $\overline{\rho}(z_i, z_*)$ is the average of the reference profile over a range of heights greater than $z_*(\rho_i)$ and so must be less than ρ_i. Thus, the product in Eq. (2.7) is positive for all such parcels. Similarly, the right panel illustrates the case for a parcel located below its equilibrium position. The average density $\overline{\rho}$ is greater than $\rho(z_i)$ but now represents an average over a portion of the reference profile below $z_*(\rho_i)$. Thus, the two terms in (2.7) are both negative and the product is once again positive. The definition (2.7) therefore satisfies requirement (2.6).

To show that (2.7) also satisfies (2.5), we first rewrite the integral for E_a as

$$E_a = g \int \mathcal{E}_a(\boldsymbol{x}, t)\,\mathrm{d}V = g \int (z - z_*)\rho(\boldsymbol{x}, t)\,\mathrm{d}V - g \int \int_{z_*}^{z} \rho(z'_*)\,\mathrm{dz}'_*\,\mathrm{dV}\,. \tag{2.9}$$

Denoting the last two integrals in (2.9) as $\mathcal{I}_1$ and $\mathcal{I}_2$ respectively, establishing (2.5) is equivalent to showing that $\mathcal{I}_2 = 0$.

Consider the contribution to $\mathcal{I}_1$ and $\mathcal{I}_2$ associated with the i^{th} parcel with volume element $\mathrm{d}V$ located at height z_i with density ρ_i. The contribution to $\mathcal{I}_1$

from this parcel is the energy expended or released in moving the i^{th} parcel from it's actual height z_i to it's equilibrium position $z_*(\rho_i) \equiv z_*^i$:

$$\mathcal{I}_1^i = g\,\mathrm{d}V\,\rho_i(z_i - z_*^i). \tag{2.10}$$

Relocation of this parcel represents a "volume displacement" of $(z_i - z_*^i) \times \mathrm{d}V\,\mathrm{m}^4$, either up- or downward depending on the sign of $(z_i - z_*^i)$.

Similarly,

$$\mathcal{I}_2^i = -g\,\mathrm{d}V \int_{z_*^i}^{z_i} \rho(z_*')\,\mathrm{d}z_*' \approx -\mathrm{g}\,\mathrm{dV} \sum_{\mathrm{j}=1}^{\mathrm{n}} \rho_{\mathrm{j}}\,\Delta \mathrm{z}_* = -\mathrm{g}\Delta\mathrm{z}_* \sum_{\mathrm{j}=1}^{\mathrm{n}} \rho_{\mathrm{j}}\,\mathrm{dV} \tag{2.11}$$

where n is the number of $\mathrm{d}V$ parcels with height in the reference density profile between z_*^i and z_i. The increment Δz_* is a signed quantity with magnitude $\mathrm{d}z_* = \mathrm{d}V/A$. $\mathcal{I}_2^i$ is thus the energy expended or released in moving the particular volume of fluid, with density either somewhat greater than or somewhat less than ρ_i, a small distance Δz_* to make room for parcel i. Schematically, this corresponds to the energy associated with shifting the parcels comprising the thick portions of the reference profiles in Figure 2.1 a small distance Δz_*. The sign of the shift again depends on the sign of $(z - z_*)$, but it is always opposite the direction implied by the relocation of parcel i from z to z_*. As the volume displacement of these parcels is equal to $-(z - z_*) \times \mathrm{d}V$, $\mathcal{I}_2^i$ gives the energetic consequences of the particular compensatory displacement required in moving parcel i to its equilibrium position. We have already seen that, taken together, $\mathcal{I}_1^i + \mathcal{I}_2^i \geq 0$ for any parcel i.

2.4 Equivalent energy 3D to 1D map

It remains to be shown that $\mathcal{I}_2$, is equal to zero. Extending the interpretation of the previous section, we continue with a discrete approach and consider the integrations over the volume V as a sequence of reordering operations involving the discrete parcels with volume elements $\mathrm{d}V$ and passing to the limit $\mathrm{d}V \to 0$. To simplify the presentation however, it is first necessary to introduce a nearly energy conserving mapping of the mass distribution $\rho(\boldsymbol{x})$ at time t to a strictly one-dimensional distribution $\rho_{\mathrm{1D}}(z)$.

The potential energy associated with the parcel located at (x, y, z) depends on the height z but is independent of the horizontal position. Furthermore, for small $\mathrm{d}V$ elements, we have seen that $\mathrm{d}z_* << \mathrm{d}z$. The profile $\rho_{1\mathrm{D}}(z)$ is constructed by taking all the $\mathrm{d}V$ elements located at a given height z, "flattening" them to occupy a volume $A \times \mathrm{d}z_*$ and placing them arbitrarily within the height range $[z, z + \mathrm{d}z]$. For each parcel i, the magnitude of the difference in potential energy between the 3D and 1D configurations is bounded by $g\,\mathrm{d}V \rho_i \mathrm{d}z$ which vanishes like $\mathrm{d}z^2$ as $\mathrm{d}V \to 0$. The potential energy associated with $\rho_{1D}(z)$ is therefore arbitrarily close to E_p in (2.2) for small but finite $\mathrm{d}V$ and equal to E_p in the limit. The important point here is that the flattened elements are geometrically conformable with those in the reference state $\rho(z_*)$ which can now be formally constructed from $\rho_{1\mathrm{D}}(z)$ via a sequence of discrete parcel interchanges. In principle, we can track the energetic consequences of both the direct equilibration of individual parcels $(\mathcal{I}_1^i)$ as well as that of the "compensatory displacement" operations $(\mathcal{I}_2^i)$ associated with each such repositioning. We show however, that the accumulated distance in compensatory displacement of each parcel, *i.e.* displacements "induced" by the direct relocation to equilibrium of all other parcels, sums to zero. This implies that the net energy released in compensatory displacements vanishes for each parcel individually and therefore, in the limit $\mathrm{d}V \to 0$, that $\mathcal{I}_2 = 0$.

2.5 Closed loop exchanges

The monotonic reference profile $\rho(z_*)$ can be obtained from $\rho_{1\mathrm{D}}(z)$ via a finite sequence of *closed loop parcel exchanges* that produces a reordering of the given sequence of density values such that the heaviest parcel is placed at the bottom of the volume, the next heaviest just above etc. The general algorithm for computing $\rho(z_*)$ is given in appendix 2.9. The idea of closed loop exchanges is illustrated by means of a sequence of parcel exchanges that closes after 4 steps as shown in Figure 2.2. Absent additional restrictions on the underlying flow, we regard the profile $\rho_{1\mathrm{D}}(z)$ as a random sequence of the density values ρ observed in V at time t. Suppose we select a random parcel located at position z_i with density

ρ_i and calculate the equilibrium position $z_*(\rho_i)$ for this parcel.

Following the schematic in Figure 2.2, we introduce the following interchange operations:

1 Move parcel ρ_i from z_i to $z = z_*(\rho_i)$.

Label the parcel previously located at $z = z_*(\rho_i)$ with index $i+1$.

2 Move parcel ρ_{i+1} from z_{i+1} to $z = z_*(\rho_{i+1})$.

Label the parcel previously located at $z = z_*(\rho_{i+1})$ with index $i+2$.

3 Move parcel ρ_{i+2} from z_{i+2} to $z = z_*(\rho_{i+2})$.

Label the parcel previously located at $z = z_*(\rho_{i+2})$ with index $i+3$.

4 Move parcel ρ_{i+3} from z_{i+3} to $z = z_*(\rho_{i+3})$.

This particular sequence of exchanges closes after 4 steps because the unique parcel with equilibrium position matching the randomly chosen initial parcel was encountered, *i.e.* $z_*(\rho_{i+3}) = z_i$. We call such a sequence a closed loop exchange. The number of steps in a closed loop exchange is greater than or equal to 1. A complete reordering, *i.e.* the construction of $\rho(z_*)$ from $\rho_{\mathrm{1D}}(z)$ can always be accomplished through a finite sequence of closed loop exchanges of varying lengths, initiated with a randomly chosen parcel.

2.6 Compensatory displacements

Recall that for each parcel relocation from z_i to z_*^i implied by (2.1) and explicitly represented by $\mathcal{I}_1^i$, a compensating displacement over a small distance $\mathrm{d}z_*$ has been introduced via $\mathcal{I}_2^i$ involving all fluid parcels with equilibrium heights between z_i and z_*^i. For a given parcel i, the two relocation operations together always result in a release of energy, *i.e.* $\mathcal{E}_a > 0$ unless parcel i happens to be located at its equilibrium height, in which case $\mathcal{E}_a = 0$.

While an individual parcel has only one primary relocation, from it's initial height z_i to it's height in the reference profile z_*^i, it is generally subject to multiple additional translations as a member of different density classes undergoing compensatory displacement as discussed above. Figure 2.3 illustrates these motions for the 4 step closed loop exchange sequence introduced in Section 2.5. The arrows indicate translation of specific sets of parcels, either up- or downward, by a distance $\mathrm{d}z_*$ in association with the primary parcel relocation at each step shown in Figure 2.2. In this example, each parcel is involved in exactly 2 compensatory translations, one up and one down, so that the total distance traveled by each parcel as a result of these translations is zero.

The cancellation of translations is a direct consequence of the fact that the 4 primary translations i through $i+3$ form a closed loop exchange sequence. The net translation during compensatory displacement for all parcels is always zero for closed loop exchange sequences regardless of their length. Because a complete reordering can always be obtained via a finite sequence of closed loop exchanges, it follows that the net compensatory translation of all parcels during the reordering is identically zero and therefore $\mathcal{I}_2$ is identically zero.

By introducing $\mathcal{I}_2$ into the definition of $\mathcal{E}_a$ we have added the particular function of $\boldsymbol{x}$ that, when added to $\mathcal{I}_1^i$, yields a positive definite contribution to the available potential energy for each parcel i, while, once integrated over all parcels, doesn't contribute to the total integral E_a. In essence, $\mathcal{I}_2$ filters out the cancellation inherent in the integrand (2.1) and isolates the unique positive definite contribution from each spatial location.

2.7 Application to rotating horizontal convection

Horizontal convection is the term used to describe the buoyancy driven flow that results when a fluid is subjected to horizontally variable buoyancy forcing at either its top or bottom surface (see *Hughes and Griffiths*, 2008). The flows that result are generated entirely by the conversion of available potential energy to kinetic energy through the buoyancy flux (e.g. *Winters and Young*, 2009) and so knowledge of the spatial distribution of $\mathcal{E}_a$ in these flows is of fundamental interest.

Figure 2.4 (left panel) shows the density field from a two-dimensional simulation of horizontal convection with temperature prescribed at the upper boundary such that the fluid is heated at the left and right portions of the upper surface and cooled in the middle. This snapshot will be used to illustrate the analytical formulae introduced in the previous discussion.

The black circle in the left panel indicates the vertical position $z_i = 0.0501\,m$ of fluid parcel i with density $\rho_i = 0.0119\,kg/m^3$. The black circle in the right panel shows that the corresponding equilibrium height for this parcel in the reference profile is $z_*(\rho_i) = 0.0995\,m$, which is above z_i (red circle). Parcel i must therefore be moved a distance $(z_*(\rho_i) - z_i)$ upward during an adiabatic sorting to the minimum energy state. This corresponds to a 'volume displacement' of $dV \times (z_*(\rho_i) - z_i) = 2.228 \times 10^{-8}\ m^4$ for the particular discrete interior parcel size for this simulation. The average $\bar{\rho}$, defined in (2.8), is the average density of the fluid between the red and black circles in the right panel. The total volume of fluid within the density range is equal to $(z_*(\rho_i) - z_i) \times A$ and the corresponding volume flux when lowering this fluid the small distance $dz_* = dz/A$ exactly cancels that associated with equilibrating parcel i.

These two relocation operations, equilibration of a single parcel and the corresponding compensatory displacement, are the two operations implied by the integrands of $\mathcal{I}_1$ and $\mathcal{I}_2$ respectively. Carrying out these operations point-wise throughout the domain yields the spatial maps shown in Figure 2.5. The top panel shows $10^3 \times \mathcal{E}_a$ as defined in (3.3), which characterizes the essential contribution from each parcel to the volume integrated available potential energy E_a. The available potential energy density is concentrated in the middle of the domain in the cool fluid that is ejected from the upper surface as a negatively buoyant plume. The middle panel shows $(z - z_*)\rho$, the integrand of $\mathcal{I}_1$ in Eq. (2.9), which integrates to the same value as the function shown in the top panel but exhibits both positive and negative values with much larger magnitudes. Integrating this function over the domain produces significant cancellation which prevents identification of the essential contribution on a point-wise basis. The bottom panel shows $-(z-z_*)\bar{\rho}$, the integrand for $\mathcal{I}_2$. This function accounts for the compensatory displacements associated with each direct parcel relocation. Point-wise it is always opposite in sign to the function in the middle panel. In the absence of discretization errors, the volume integral of this function would be identically zero. In this example, the integral $\mathcal{I}_2$ is a small fraction of E_a:

$$\frac{\left|\int -(z-z_*)\,\bar{\rho}\,\mathrm{d}V\right|}{\int (z-z_*)\,\rho\,\mathrm{d}V} \approx 1\times 10^{-3}. \tag{2.12}$$

Figure 2.6 shows results from a three dimensional simulation of rotating horizontal convection. In this example, positive heat flux is applied at the upper left, negative heat flux at the upper right and the entire domain rotates about the vertical axis. The non-dimensional parameters defining this simulation (see *Hughes and Griffiths*, 2008) are the flux Rayleigh number $Ra_f \equiv B_{max}L_x^4/\nu\kappa^2 = 3.8\times 10^9$, the Prandtl number $Pr \equiv \nu/\kappa = 7$, the aspect ratio $H/L_x = 0.25$ and the rotation rate $Q \equiv f\,L_x^2/\nu Ra_f^{1/3} = 9.5$ (see Barkan, Winters and Llewellyn Smith, 2012). Here B_{max} is the maximal buoyancy flux applied at the top surface, f is the Coriolis frequency, L_x is the domain length in the $\boldsymbol{x}$ direction, and ν and κ are molecular diffusivities for momentum and temperature respectively. The initial conditions for this three dimensional simulation were the steady state solutions from a two dimensional simulation with identical parameters. In two-dimensions, the addition of sufficiently rapid rotation inhibits lateral spreading of dense fluid at depth, producing a geostrophically balanced flow characterized by relatively high available potential energy density beneath the cooled portion of the upper surface. Once perturbations are introduced and three-dimensional flow is allowed to develop, baroclinic instability ensues, releasing the stored available potential energy. Because of the high available potential energy content of these initial conditions, the ensuing flow undergoes a quasi-periodic oscillation between two distinct states. Figure 2.6 shows the y averaged density (left) and the corresponding y averaged $\mathcal{E}_a$ (right) for each of these states. State 1 has high values of available potential energy owing to the sloping isopycnals while in state 2 the available potential energy has been almost completely released via baroclinic instability. Figure 2.7 shows the volume integrated available potential energy E_a as the flow oscillates between the two states. Initially E_a is $5-6$ times larger than in the rest of the simulation due to the excess available potential energy stored in the two dimensional flow when baroclinic instability cannot occur. Once the initial excess available potential energy is released, the flow develops quasi-steady oscillations which decay slowly in time. This slow decay shows that most of the energy is being exchanged between kinetic and available potential energies and only a small fraction is being dissipated or expended in irreversible mixing.

2.8 Discussion

An exact, positive definite available potential energy density $\mathcal{E}_a$ (*Holliday and McIntyre*, 1981; *Roullet and Klein*, 2009; *Molemaker and McWilliams.*, 2010) for stratified flows under the Boussinesq approximation has been shown to integrate to the expression for E_a in *Winters et al.* (1995) and to have a physical interpretation in terms of adiabatic redistribution of fluid parcels and the corresponding positive definite release of potential energy. The expression is exact in the sense that it does not rely on a small perturbation approximation for the displacements nor a near linearity approximation for the reference profile. Independence from a small perturbation approximation has advantages both for small scale turbulent flows, where parcel excursions can be large compared to eddy scales, and for larger scale ocean flows where the curvature of the reference profile is often significant (*Roullet and Klein*, 2009). The explicit connection to E_a allows a rigorous interpretation of $\mathcal{E}_a$ in terms of the volume integrated energy transfers between kinetic energy and available and background components of potential energy described in the evolution equations of *Winters et al.* (1995).

The concepts of available potential energy are quite useful in understanding the dynamics of horizontal convection. In horizontal convection, the fluid is energized by a diffusive flux of available potential energy through the upper surface (*Winters and Young*, 2009; *Hughes et al.*, 2009). The interpretation of E_a in terms of the energy released under the action of two resorting operations, i.e. the repositioning of a given parcel and the corresponding compensatory displacements required, and the spatial distribution of $\mathcal{E}_a$ allows one to see at a glance that state 2 in Figure 2.6 represents a nearly complete release of available potential energy while also illustrating where in the flow the baroclinic instability is ineffective in releasing available potential energy. The energy transfers are similar to those discussed by *Molemaker and McWilliams.* (2010) for an Eady-like (*Eady*, 1947) shear flow.

Finally, we note that while the development presented here is formally valid for simple container shapes with uniform cross section A, it is straightforward to compute the corresponding quantities for irregular numerical discretizations and/or in more complicated single-basin geometries by taking dV to be a function of position and A to be a function of height z. For irregularly shaped containers, *i.e.* those with tall sills or obstructions, *Stewart* (2012) suggests defining the reference state in terms of a local minimum of potential energy rather than the global minimum discussed here. Local minima reflect re-sortings in which dense fluid parcels are sorted and stacked within their local basin, even if additional potential energy would be released by allowing the parcel to be positioned in a different, perhaps deeper basin. Such local minima may be useful, for example, when the energy required to move deep dense parcels from one basin to another is large compared to the typical kinetic energy of the flow.

2.9 Acknowledgements

Discussions with Myrl Hendershott were much appreciated and gratefully acknowledged. We also appreciate the helpful suggestions of Jonas Nycander. This work was supported by the National Science Foundation (grant numbers OCE-0726320 and OCE-0926481). The chapter has been published in: Winters, K. B. and **Barkan, R.** (2013). Available potential energy density for Boussinesq fluid flow. *J. Fluid Mech.*, 714, 476-488.

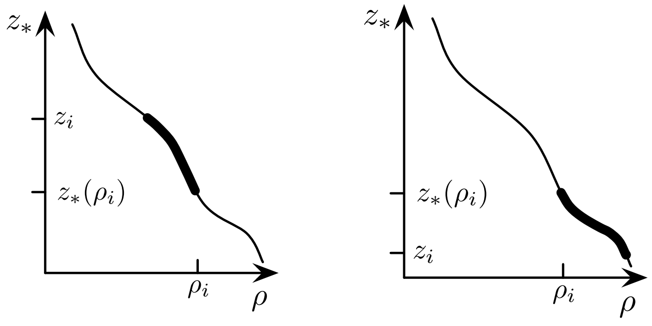

$(z_i - z_*) > 0$ $\quad$ $(z_i - z_*) < 0$

$\rho(z_i) - \overline{\rho}(z_i, z_*) > 0$ $\quad$ $\rho(z_i) - \overline{\rho}(z_i, z_*) < 0$

Figure 2.1: $\mathcal{E}_a$ (Eq. 2.7) is positive definite.

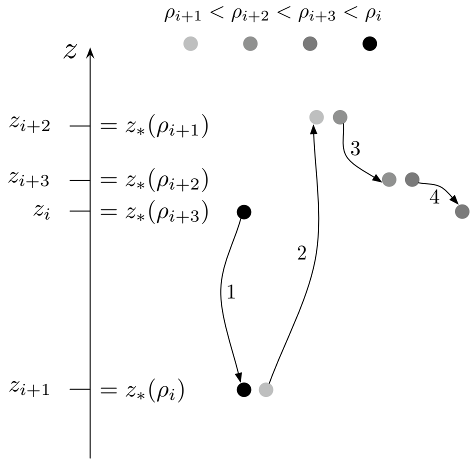

Figure 2.2: Schematic representation of the 4 step closed loop exchange described in the text. Starting with the parcel located at z_i, parcels are moved to their equilibrium heights z_*, replacing the parcels previously located at those locations. The replaced particles are then moved to their equilibrium positions. The parcel exchanges continue until the parcel with equilibrium position z_i replaces the original parcel and the loop is closed.

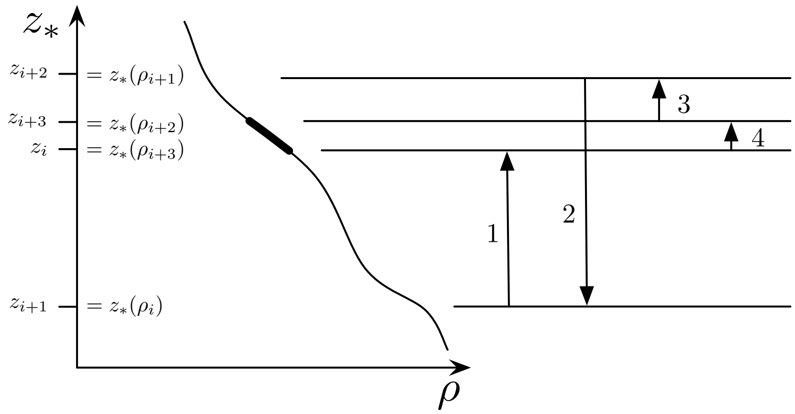

Figure 2.3: Compensatory displacements for the 4 step closed loop exchange sequence shown in Figure 2.2 and described in the text. The upward arrow labeled 1 indicates the upward transport of all fluid with density between ρ_{i+3} and ρ_i over a distance dz_* which comprises the compensatory displacements in $\mathcal{I}_2^i$ for parcel i. The same parcels are moved an equivalent distance downward as part of the compensatory displacements for parcel $i+1$. Similarly, the parcels within the density range indicated by the heavy line portion of the curve are moved down and up a distance dz_* during the compensatory displacements for steps 2 and 4 respectively. All fluid parcels experience a zero net compensatory displacement for a closed loop exchange sequence.

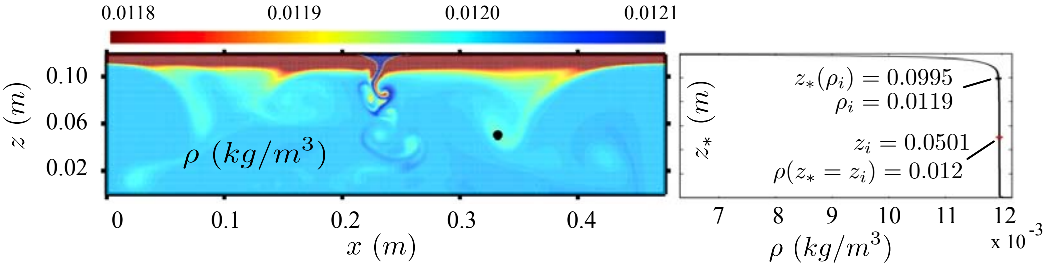

Figure 2.4: Left: snapshot of density field from a numerical simulation of horizontal convection illustrating the calculations associated with a single fluid parcel (filled black circle) with density $\rho = \rho_i$ located at $z = z_i$, at time t. Right: the corresponding reference profile $\rho(z_*)$ associated with the minimum potential energy state attainable via adiabatic sorting. Filled red circle shows the density of the fluid parcel located at z_i in the sorted profile, $\rho(z_* = z_i)$.

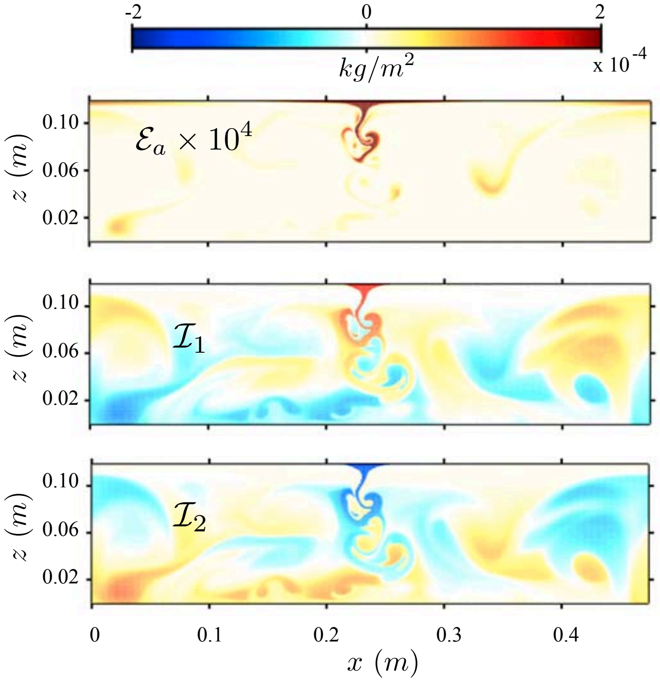

Figure 2.5: Integrands for $\mathcal{E}_a$, $\mathcal{I}_1$ and $\mathcal{I}_2$ as a function of x and z are shown respectively in the top, middle and bottom panels. $\mathcal{E}_a$ is multiplied by 10^4.

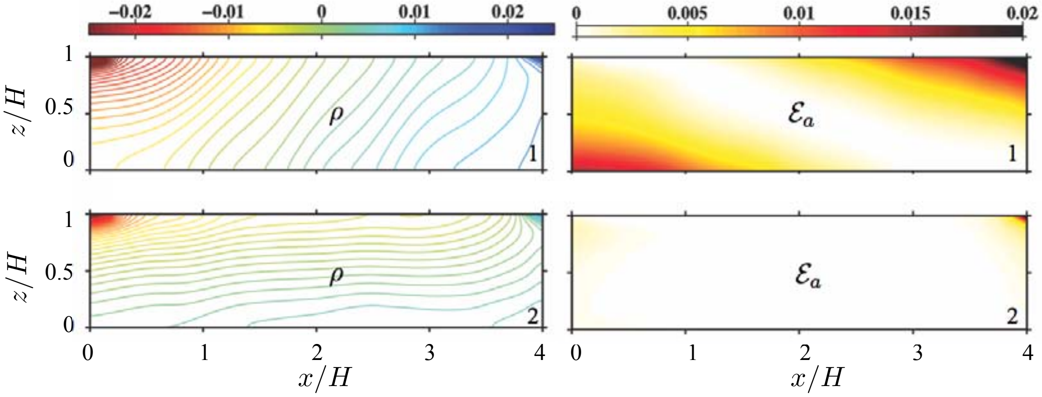

Figure 2.6: Left: y averaged snapshots of density ρ, normalized by $\rho_0 B_{max} H/g\kappa$. Right: the corresponding y averaged available potential energy density normalized by $\rho_0 B_{max} H^2/g\kappa$. States 1 and 2 shown in upper and lower panels respectively.

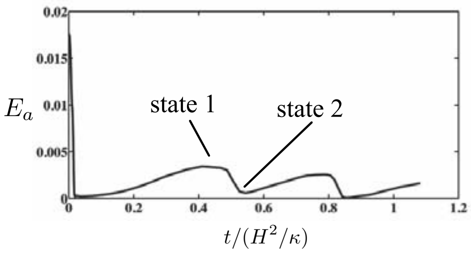

Figure 2.7: E_a, normalized by $\rho_0 V B_{max}\, H^2/\kappa$, as a function of time. E_a decreases rapidly owing to baroclinic instability. This rapid transient is followed by a slowly decaying oscillation between states 1 and 2.

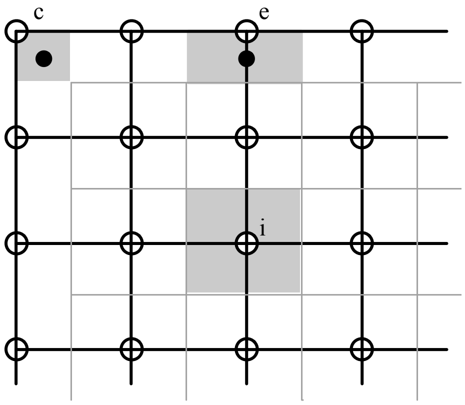

Figure 2.8: Schematic of a discrete grid (collapsed to two dimensions) with density values given at the grid points shown as open circles. Interior grid points (labeled i) give the density values at the center of discrete volume elements of size dV (shaded). Density values near edges (e), seams and corners (c) are interpolated to their respective volume centers (filled circles). These volume elements have sizes equal to one half, one quarter and one eighth dV respectively. (Here corner volume elements are bounded by three edge faces, seams by two and edges by one.)

2.10 Appendix: Calculation of the reference profile

We describe here our implementation of the construction of the one-dimensional reference state $\rho(z_*)$ from a snapshot of the three-dimensional Boussinesq density field obtained from a numerical model. For specificity, we assume that the numerical model generates density values at regularly spaced discrete grid points in a simple domain of size $L_x \times L_y \times L_z$. Let $A = L_x L_y$ be the cross sectional area of the domain and $\mathrm{d}V = \mathrm{d}x\,\mathrm{d}y\,\mathrm{d}z$ the nominal discrete differential unit of volume. The reference state is simply the mapping between height z_* and density ρ corresponding to a global minimum in potential energy defined by Eq. 2.3. We construct this state using a simple sorting and stacking procedure.

Let the density value at each interior grid point i represent the differential volume element centered at the gridpoint as shown in Figure 2.8. All such elements have a volume $\mathrm{d}V$. Edge elements adjacent to the boundaries are similar except they occupy only half the volume $\mathrm{d}V$ and the density values at the volume centers are not directly available from the model output but rather are found by interpolation. Similarly, the seam and corner elements occupy one quarter and one eighth the volume of the interior elements.

Mapping to a discrete one dimensional profile can be thought of as 'squashing' each volume element $\mathrm{d}V_i$ into a thin sheet of thickness $\mathrm{d}z_{*i} = \mathrm{d}V_i/A$ and assigning its central density value ρ_i to a particular height z_{*i}. The first step is to determine the central density values ρ_i for all the edge, seam and corner elements, keeping track of the corresponding value $\mathrm{d}z_{*i}$. The set of discrete density values is then sorted in order of decreasing density. The densest parcel is placed at the bottom of the domain and assigned a height value of $\mathrm{d}z_{*i}/2$. The rest of the parcels are then stacked in order with each parcel j assigned a z_* value of $z_{*j-1} + \mathrm{d}z_{*j-1}/2 + \mathrm{d}z_{*j}/2$. The result is a monotonic mapping of ρ to z_* expressed on a discrete z_* 'grid' that is unequally spaced owing to the different sized volume elements at the edges, seams and corners of the domain. This approach is easily adapted to different gridding schemes and irregular domains. It obviates the unnecessary step of first distributing the sorted parcels onto horizontal planes and then approximately removing the remaining available potential energy by averaging.

Chapter 3

Rotating Horizontal Convection

'Horizontal Convection' (HC) is the generic name for the flow resulting from a buoyancy variation imposed along a horizontal boundary of a fluid. We study the effects of rotation on three-dimensional HC numerically in two stages: first when baroclinic instability is suppressed, and second, when it ensues and baroclinic eddies are formed. We concentrate on changes to the thickness of the near-surface boundary layer, the stratification at depth, the overturning circulation and the flow energetics during each of these stages. Our results show that, for moderate Rayleigh numbers ($O(10^{11})$), rapid rotation greatly alters the steady state solution of HC. When the flow is constrained to be uniform in the transverse direction, rapidly-rotating solutions do not support a boundary layer, exhibit weaker overturning circulation and greater stratification at all depths. In this case, diffusion is the dominant mechanism for lateral buoyancy flux and the consequent buildup of available potential energy leads to baroclinically unstable solutions. When these rapidly-rotating flows are perturbed, baroclinic instability develops and baroclinic eddies dominate both the lateral and vertical buoyancy fluxes. The resulting statistically steady solution supports a boundary layer, larger values of deep stratification and multiple overturning cells compared with non-rotating HC. A transformed Eulerian-mean approach shows that the residual circulation is dominated by the quasi geostrophic eddy streamfunction and that the eddy buoyancy flux has a non-negligible interior diabatic component. The kinetic and available potential energies are greater than in the non-rotating case and the mixing efficiency drops from ~ 0.7 to ~ 0.17. The eddies play an important role in the formation of the thermal boundary layer and, together with the negatively buoyant plume, help establish deep stratification. These baroclinically active solutions have characteristics of geostrophic turbulence.

3.1 Introduction

Horizontal Convection (HC) is the term used to describe the flow resulting from a buoyancy variation imposed along a horizontal boundary of a fluid (*Stern*, 1975). In the ocean, the equator to pole gradient of solar irradiance produces differential surface buoyancy forcing, which is believed to play an important role in the large scale dynamics. HC is thus often used as simple model to study the large scale overturning circulation, stratification and thermocline of the world oceans.

Based on a series of laboratory experiments and thermodynamic reasoning, *Sandström* (1908, 1916) speculated that a closed steady circulation can only be maintained if the stabilizing buoyancy source is located at a lower level than the destabilizing buoyancy source. This hypothesis, often referred to as *Sandström's theorem*, suggests that buoyancy forcing alone is an insufficient mechanism of supplying energy to the ocean circulation (*Munk and Wunsch*, 1998). *Jeffreys* (1925) showed however, that Sandström's argument was flawed because it ignored the effects of diffusion. Furthermore, *Coman et al.* (2006) revisited Sandström's experiment and found persistent circulation, even in cases where the stabilizing buoyancy source was located at the same level as, or above, the destabilizing source. *Paparella and Young* (2002) argued that HC is non-turbulent because in the limit that the kinematic viscosity ν and diffusivity κ go to zero, for a fixed Prandtl number $Pr \equiv \nu/\kappa$, the volume-averaged kinetic energy dissipation goes to zero. This contrasts with typical turbulent flows for which the dissipation rate is set by the forcing at scales larger than those in the inertial subrange and is independent of the fluid viscosity. This argument, often referred to as the *anti-turbulence theorem*, supports Sandström's hypothesis, suggesting that a hypothetical ocean circulation, driven by surface buoyancy forcing alone, could not exhibit the observed small-scale marine turbulence without other forms of energy sources. Recently, however, *Scotti and White* (2011) argued that the criterion leading to the *anti-turbulence theorem* is too restrictive and that, based on certain statistical properties of the velocity gradient tensor which are common to all known turbulent flows, HC is in fact turbulent. In addition, using flow visualization techniques, *Mullarney and Hughes* (2004) and *Stewart* (2012) demonstrated in laboratory experiments of both heat- and salt-driven HC that the plume beneath the destabilizing buoyancy forcing is turbulent and suggested that it plays an important role in mixing the fluid.

Rossby (1965) performed a set of laboratory experiments of HC by differentially heating a fluid from below. Motivated by his observations at steady state, he derived scaling laws for the thermal boundary layer depth and the strength of the circulation (see §3.3 for details). These scaling laws suggest that in the oceanic regime HC supports a thinner thermal boundary layer and weaker circulation and abyssal stratification than those observed (*Munk and Wunsch*, 1998). These scaling laws have subsequently been verified by numerical simulations and laboratory experiments (*Rossby*, 1998; *Mullarney and Hughes*, 2004; *Chiu-Webster et al.*, 2008; *Ilicak and Vallis*, 2012). It thus seems that, although HC exhibits similar features to those observed in the overturning circulation of the oceans, additional physical processes and energy sources are important to obtain a better match with the oceanic regime. Previous numerical and laboratory studies have examined the effects of surface stress on HC (*Beardsley and Festa*, 1972; *Whitehead and Wang*, 2008; *Tailleux and Rouleau*, 2010; *Hazewinkel et al.*, 2012; *Paparella and Young*, 2002; *Ilicak and Vallis*, 2012). It was generally found that the addition of mechanical surface stress makes a substantial difference to the structure of the flow and to the stratification. *Stewart* (2012) examined the effects of mechanical stirring on HC in the laboratory. By parametrizing the effective turbulent diffusivity (κ_{eff}) induced by the stirring rod in their experiments they found that stirring levels corresponding to $\kappa_{eff} = 100\kappa$ (κ being the molecular diffusivity) are necessary for the stirring rod to dynamically dominate the effective turbulent diffusivity of the negatively buoyant plume.

In the present chapter, however, we are concerned primarily with the basic HC model and it's applicability to oceanic processes. We suggest that in order to study HC in an oceanic context, rapid rotation has to be included and its effects understood. In non-rotating HC, the interior lateral buoyancy flux is accomplished via advection. When rapid rotation is added, one expects this lateral interior advective flux to be inhibited and for baroclinic instability to be generated, resulting in very different pattern of circulation and buoyancy transport mechanism. We therefore focus our attention on the effects rotation has on HC and examine the nature of the resulting flow which we term *'Rotating Horizontal Convection'* (RHC). The importance of rotational effects on the ocean thermocline (corresponding to the thermal boundary layer in HC studies) is not a new concept and dates back to classical thermocline theory studies by *Robinson and Stommel* (1959); *Bryan and Cox* (1967); *Welander* (1971) and many others. *Stern* (1975) discusses specifically the thermal boundary layer scaling of HC in a rapidly rotating annulus. *Hignett et al.* (1981) performed a set of laboratory experiments of RHC and describe the dynamics as being controlled by the parameter Q defined as the square of the ratio of the non-rotating thermal-layer scale (Rossby boundary layer) to the viscous Ekman scale. Their experiments focussed on the moderately rotating regime with $Q \sim O(1)$ and they proposed a similarity solution in the specific case of a quadratically varying surface temperature. They also discuss a critical value $Q_c \approx 3.4$, above which baroclinic instability sets in and waves are seen. *Park and Whitehead* (1999) performed a set of laboratory experiments of RHC in the moderately rotating regime and proposed scaling laws for the lateral heat flux and thermal boundary layer. They further showed that when typical North Atlantic values are introduced, their scaling law predicts heat flux values that are comparable to those observed if the diffusivity is taken as an 'eddy' diffusivity of 10^{-4} m^{2}s^{-1}. We extend these studies by exploring the rapidly rotating regime, $Q \gg 1$, which is more relevant to the oceanic regime. We also allow for three dimensional effects and the consequent generation of baroclinic eddies. Baroclinic eddies are thought to play an important role in the dynamics of the oceanic overturning circulation (*Wolfe and Cessi*, 2010), the establishment of the ocean stratification (*Marshall et al.*, 2002), and the transport of buoyancy and tracers in the ocean and the atmosphere (*Pérez-Pérez Read & Moroz* 2010 and references therein). The effects of eddies on large scale flows are often illustrated using residual-mean theories based on the works of *Andrews and McIntyre* (1976, 1978). For flows in channels the transformed Eulerian-mean (TEM) approach (see e.g. *Plumb & Ferrari* 2004) provides a good approximation to the residual circulation (*Wolfe*, 2014) and we adopt this approach here.

The current work consists of Direct Numerical Simulations (DNS) of RHC using the model defined in § 3.2. We seek to answer the following main questions:

i. How are the strength of the overturning circulation, the thermal boundary layer depth and the deep stratification affected by adding rotation to HC? Are previously proposed scaling laws consistent with the numerical simulations for different rotation rates?

ii. What are the effects of baroclinic instability and of the resulting baroclinic eddies in the rapidly rotating numerical simulations? How do the results compare with non-rotating HC simulations?

iii. How are the available potential energy (E_a) and kinetic energy (E_k) cycles modified by rotational effects? What part do the eddies play in these energy transfers?

In § 3.3 we review scaling arguments, show numerical solutions of non-rotating HC and discuss the criteria used to assess the accuracy of the simulations. In § 3.4 we discuss non-dimensional parameters and previously suggested scaling laws associated with RHC. In § 3.5, simulations of RHC in which baroclinic instability was suppressed ($\boldsymbol{x}$-uniform RHC) are discussed and an analytical model capturing the essence of these solutions is described. In § 3.6, baroclinically-active RHC solutions are presented and compared with solutions of non-rotating HC and $\boldsymbol{x}$-uniform RHC. In § 3.7 we examine changes to the energy balances in the presence of rotation. Finally, in § 3.8 we summarize and discuss our results.

3.2 Formulation

We consider a three dimensional rotating fluid in a rectangular box of volume V, uniform depth H, lateral and transverse dimensions L_y and L_x respectively. The vertical coordinate is $-H \leq z \leq 0$, and density is expressed as $\rho = \rho_0(1 - g^{-1}b)$, where b is the 'buoyancy'. The Cartesian Boussinesq equations of motion are:

$$\frac{D\boldsymbol{u}}{Dt} + f\hat{\boldsymbol{k}} \times \boldsymbol{u} = -\nabla p + b\hat{\boldsymbol{k}} + \nu\boldsymbol{\nabla}^2\boldsymbol{u} - rf_b(z)(u\boldsymbol{x} + v\boldsymbol{y}), \tag{3.1a}$$

$$\frac{Db}{Dt} = \kappa\nabla^2 b, \tag{3.1b}$$

$$\boldsymbol{\nabla} \cdot \boldsymbol{u} = 0. \tag{3.1c}$$

The pressure is $\rho_0 p$, f is the Coriolis frequency, r [s^{-1}] is the coefficient of bottom drag, $f_b(z)$ is a near-bottom localization function defined later in (4.19) and $\hat{\boldsymbol{k}}$ is the unit vector in the vertical direction. No-penetration conditions $\boldsymbol{u} \cdot \hat{\boldsymbol{n}} = 0$ are imposed on the top, bottom and lateral ($\boldsymbol{y}$) sides, where $u = (u, v, w)$ and $\hat{\boldsymbol{n}}$ is the outward normal to the surface V. Periodic boundary conditions are prescribed in the transverse ($\boldsymbol{x}$) direction to resemble the rotating tank experiments with infinite radius of curvature. The top and bottom boundary conditions are free-slip. The buoyancy flux specified at the top surface ($z = 0$) is:

$$\kappa\frac{\partial b}{\partial z} = B_{max} f(x, y) \quad \text{with} \quad \int f(x, y)\ \mathrm{d}x\,\mathrm{d}y = 0, \tag{3.2}$$

where B_{max} [m^{2}s^{-3}] is the magnitude of the maximal buoyancy flux applied at the surface. The imposed surface flux will depend primarily on y, with variability in x introduced only as a means of perturbing the forcing. On the other five faces of V, $\nabla b \cdot \hat{\boldsymbol{n}} = 0$. Throughout the paper $\langle\cdot\rangle$ denotes a volume average, $\hat{\cdot}$ denotes a spatial average over the horizontal area $A = L_x \times L_y$, $\bar{\cdot}$ denotes an average over the transverse length L_x, and eddies (denoted by $'$) are defined as perturbations from the transverse average.

The non-dimensional parameters that govern non-rotating HC are the fixed-buoyancy Rayleigh number Ra, the fixed-flux Rayleigh number Ra_B, the Prandtl number Pr and the aspect ratio α (*Hughes and Griffiths*, 2008) defined as:

$$Ra \equiv \frac{b_{\max} L_y^3}{\nu\kappa}, \qquad Ra_B \equiv \frac{B_{max} L_y^4}{\nu\kappa^2}, \qquad Pr \equiv \frac{\nu}{\kappa}, \qquad \alpha \equiv \frac{H}{L_y}. \tag{3.3}$$

Here b_{max} [ms^{-2}] is the maximal specific buoyancy at the top and B_{max} is described in (3.2). Typically in HC, the nature of the buoyancy boundary condition determines which of the Rayleigh numbers is known *ab intio* and which is part of the solution. The two numbers are related via the Nusselt number $Nu \equiv Ra_B/Ra$ (*Hughes and Griffiths*, 2008), which measures the ratio between convective to conductive buoyancy transport along the lateral length of the box L_y.

The volume averaged, kinetic (E_k), potential (E_p), background potential (E_b), and available potential ($E_a \equiv E_p - E_b$) energy equations for this model take the form (*Winters and Young*, 2009):

$$\frac{d\langle E_k\rangle}{dt} \equiv \frac{1}{V}\frac{d}{dt}\left(\frac{1}{2}\int |\boldsymbol{u}|^2\,\mathrm{d}V\right) = \langle wb\rangle - \nu\langle||\boldsymbol{\nabla}\boldsymbol{u}||^2\rangle - r\langle f_b(z)|\boldsymbol{u}_H|^2\rangle, \tag{3.4a}$$

$$\frac{d\langle E_p\rangle}{dt} \equiv \frac{1}{V}\frac{d}{dt}\left(\int -zb\,\mathrm{d}V\right) = -\langle wb\rangle + \frac{\kappa}{H}\Delta\widehat{b}, \tag{3.4b}$$

$$\frac{d\langle E_b\rangle}{dt} \equiv \frac{1}{V}\frac{d}{dt}\left(\int -z_* b\,\mathrm{d}V\right) = \kappa\langle\frac{dz_*}{db}|\nabla b|^2\rangle - \frac{\kappa}{H}z_*(\widehat{b_{top})b_z}(0), \tag{3.4c}$$

$$\frac{d\langle E_a\rangle}{dt} \equiv \frac{1}{V}\frac{d}{dt}\left(\int (z_* - z)b\,\mathrm{d}V\right) = -\langle wb\rangle - \kappa\langle\frac{dz_*}{db}|\nabla b|^2\rangle + \frac{\kappa}{H}\Delta\widehat{b} + \frac{\kappa}{H}z_*(\widehat{b_{top})b_z}(0), \tag{3.4d}$$

where $z_*(b,t)$ is the reference height in the minimum potential energy state of a fluid with buoyancy $b(\boldsymbol{x},t)$ (*Winters et al.*, 1995), $\boldsymbol{u}_H = (u,v)$ and $\Delta\widehat{b} = \widehat{b}(0) - \widehat{b}(-H)$.

The model equations (3.1) are solved using the three dimensional spectral model **flow_solve** (*Winters and de la Fuente*, 2012). The fixed-flux boundary condition (3.2) is implemented using a forcing term $\mathcal{F}(y,z)$ in (4.1b) of the form:

$$\frac{Db}{Dt} - \kappa\nabla^2 b = \mathcal{F}(y,z) \equiv S\mathrm{e}^{-(z/\sigma_z)^2}(\mathrm{e}^{-(y/\sigma_y)^2} - \mathrm{e}^{-([y-L_y]/\sigma_y)^2}), \tag{3.5}$$

where $\sigma_z = O(\Delta z)$ and Δz is the grid spacing in the $\hat{\boldsymbol{k}}$-direction. In the limit of infinite resolution ($\Delta z \to 0$) the inhomogeneity in the boundary condition is exactly exchanged for inhomogeneity in the governing equation (*Winters and de la Fuente*, 2012) so that (3.5) and (3.2) are identical. The length σ_y is chosen to confine the negative/positive buoyancy source/sink to the upper corners of the domain. The corresponding maximal surface buoyancy flux $B_{max} = (g/\rho_0)\sqrt{\pi}S\sigma_z$. Note that $\int \mathcal{F}(y,z)\,dy = 0$ to ensure mass conservation.

The form of the bottom drag $f_b(z)$ in (4.1a) is

$$f_b(z) = e^{-([z+H]/\sigma_d)^2}, \tag{3.6}$$

where $\sigma_d = 6\,\Delta z$, which smoothly confines the action of the drag term to a thin but well resolved near-bottom layer. Bottom drag was only used for the baroclinically-active RHC simulations (see § 3.6).

For the baroclinically-active RHC simulations, the forcing term $\mathcal{F}$ in (3.5) was perturbed as follows:

$$\frac{Db}{Dt} - \kappa\nabla^2 b = \mathcal{F}(y,z)\left(1 + dS\left(e^{-\left(\frac{x-[L_x/2+\sigma_x]}{\sigma_x}\right)^2} - e^{-\left(\frac{x-[L_x/2-\sigma_x]}{\sigma_x}\right)^2}\right)\right), \tag{3.7}$$

in order to trigger baroclinic instability. Here $dS = 0.005 \times S$ and σ_x was set to six times the grid spacing in the $\hat{\boldsymbol{i}}$-direction ($\hat{\boldsymbol{i}}$, being the unit normal in the transverse direction). This introduces a total perturbation of 1%, sufficient to initiate baroclinic instability while exactly maintaining the mass flux of the unperturbed runs. The relatively small value of σ_x perturbs a wide range of transverse wavenumbers and thus allows the evolving flow to select the most unstable wavenumber. The perturbation to the forcing (3.7) was only applied during an initiation stage of the simulations spanning the first 0.01 diffusive times (H^2/κ), which was at most $\sim 1\%$ of an entire simulation time.

The numerical simulations presented in this paper model thermally driven HC ($Pr = 7$). Table 3.1 summarizes the simulations presented in this paper.

3.3 Non-rotating Horizontal Convection

Rossby (1965) suggested scaling laws that provide a satisfactory condensation of numerical simulations and laboratory experiments of non-rotating HC. Performing laboratory experiments with fixed-temperature boundary conditions, he first assumed that the typical vertical variation of buoyancy within the thermal boundary layer of thickness δ_R is $b_{\max}$. He further assumed that the dominant balance in the vertical momentum equation is hydrostatic, and that, in the horizontal momentum equations, the pressure force is balanced by vertical viscosity.

Finally, he assumed that the balance in the buoyancy equation (4.1b) is between the advective terms $\boldsymbol{u}\cdot\nabla b$ and vertical diffusion κb_{zz}. The resulting scaling law is

$$\delta_R \sim \frac{L_y}{Ra^{1/5}} \sim \frac{L_y}{Ra_B^{1/6}}, \tag{3.8}$$

where the scaling law in terms of Ra_B is derived using $\kappa b_{\max}\delta_R^{-1} \sim B_{max}$. The corresponding lateral velocity scale v_R and $\boldsymbol{x}$-averaged streamfunction scale ψ_R can be found using $v_R \sim \kappa L_y \delta_R^{-2}$, $\psi_R \sim \kappa L_y \delta_R^{-1}$. Two things should be kept in mind regarding Rossby's scaling law (3.8). First, it is thought to hold in the interior of the flow away from the lateral side boundaries. Second, δ_R is independent of the domain depth H, implying that $\delta_R/H \ll 1$. *Chiu-Webster et al.* (2008) discuss the nature of the flow when $\delta_R/H \sim O(1)$. In this regime the analytical solution proposed by *Smith* (1976) to describe estuarine dynamics, can be modified to describe HC dynamics quite accurately.

Estimating Rossby's scaling laws using molecular oceanographic values corresponding to a temperature difference of $25K$, a thermal expansion coefficient of 2×10^{-4} K^{-1}, $L_y = 10\times L_x = 2000\times H = 10^7$ m and $\nu = 10\times\kappa = 10^{-7}$ m^{2}s^{-1} yields $\delta_R = 2.9$ m, $v_R = 0.12$ ms^{-1} and $\psi_R = 0.35$ Sv. If turbulent values are used ($\nu = \kappa = 10^{-5}$ m^{2}s^{-1}) then $\delta_R = 11.5$ m, $v_R = 0.75$ ms^{-1} and $\psi_R = 8$ Sv.

Figure 3.1(a) shows a typical, steady state, $\boldsymbol{x}$-averaged, density field of non-rotating HC. Qualitatively, the flow develops a box-scale lateral density gradient within a boundary layer that forms near the top ($z = 0$). This lateral density gradient drives a flow towards the destabilizing (cold) end, where a plume is formed that penetrates to full depth. The volume transport in the plume is returned laterally along the bottom boundary ($z = -H$). The circulation is closed via slow vertical flow in the interior of the domain. Away from the lateral boundaries the vertical density structure is everywhere very similar to the horizontally averaged stratification shown in figure 3.1(c), with a clear maximum at $z \sim -\delta_R$ (dashed line) and an unstratified abyss. In oceanography, such a clear maximum is often used to define the thermocline. The $\boldsymbol{x}$-averaged streamfunction shows a single, clockwise overturning cell extending almost throughout the entire lateral domain as can be seen in figure 3.1(b). Figure 3.2 shows that advection is the dominant mechanism for the lateral buoyancy flux in this flow.

All of the non-rotating and the $\boldsymbol{x}$-uniform rotating simulations (§ 3.5) presented in this chapter reached a complete, pointwise steady state, and there was no difference between three-dimensional and two-dimensional simulations of these kinds. The perturbation to the forcing term $\mathcal{F}$ of the form (3.7) made no difference when applied to the non-rotating HC simulations and triggered baroclinic instability when applied to RHC simulations (§ 3.6). In order to verify that all simulated fields were resolved down to the viscous scale, the spectra of the second derivative (highest derivative in these simulations) of density in each direction were analyzed. The value of Pr was 7 for all simulations, so density fields exhibit the smallest scale in these simulations and the second derivative of density is the hardest computed field to resolve. The decay in the spectra of the second derivative down to the highest wavenumber was the first criterion used to ensure sufficient resolution. Second, because the laterally integrated forcing at the top boundary (3.5) is zero by construction, the change in total mass should remain zero at all times. Therefore the change in mass, normalized by $(\rho_0/g)S\sigma_z\sqrt{\pi}L_y^2L_xL_z\kappa^{-1}$, was computed as a function of time to measure solution quality. The normalized change in mass was less than 1×10^{-14} in all simulations. Finally, conservation of equations (4.8a), (4.8b) normalized by $|\langle wb\rangle|$ to within $\sim 1\times10^{-4}$, was the last criterion used to ensure sufficient resolution and agreement with the simulated equations of motion. Figure 3.3 shows a plot of the different terms in equations (4.8a) and (4.8b) for a typical simulation of non-rotating HC (simulation 2). The fact that $d\langle E_k\rangle/dt = d\langle E_p\rangle/dt = 0$ along with $\nu\langle||\boldsymbol{\nabla u}||^2\rangle = \kappa\Delta\widehat{b}/H = \langle wb\rangle$ indicates that the flow has reached a completely steady state.

3.4 Adding Rotation

The scaling law (3.8) has been verified by multiple authors (see § 1 for references), which motivates non-dimensionalizing (3.1) with $f \neq 0$ using δ_R, v_R, as previously proposed by *Hignett et al.* (1981). This leads to the non-dimensional momentum equations:

$$\frac{1}{Pr}\frac{D\boldsymbol{u}}{Dt} + Q\,\hat{\boldsymbol{k}} \times \boldsymbol{u} = -\frac{1}{\alpha}\nabla_H p + Ra^{2/5}\left(-\frac{\partial p}{\partial z} + b\right)\hat{\boldsymbol{k}} + \nabla^2\boldsymbol{u}, \tag{3.9}$$

where, for simplicity, $L_y = L_x = L$, $\nabla^2 = \alpha^2(\partial^2/\partial y^2 + \partial^2/\partial x^2) + \partial^2/\partial z^2$, and $\nabla_H = \alpha(\partial/\partial x, \partial/\partial y)$. The non-dimensional number

$$Q = 2(\delta_R/d)^2 \tag{3.10}$$

describes the rotation rate in rotating convection systems (*King et al.*, 2009),, δ_R is defined in (3.8), and $d = \sqrt{2\nu/f}$ is the Ekman depth. *Killworth and Manins* (1980) show that $Pr \geq 5$ is sufficiently large for the material derivative in (3.9) to be ignored. For $Q = 0$ (no-rotation) we thus recover the momentum balance leading to (3.8).

We now provide a short review of scaling laws previously suggested for the thermal boundary layer depth in RHC. These are linear scaling laws, in the sense that they ignore the effects of baroclinic eddies. In all cases the velocity and streamfunction scales can be determined using $v \sim \kappa L_y \delta^{-2}$, $\psi \sim \kappa L_y \delta^{-1}$. We find it illuminating to present these results as modifications to the non-rotating scales (Rossby scales).

Robinson and Stommel (1959) proposed the same dominant balance in the vertical momentum equation and buoyancy equation as Rossby. However, in the horizontal momentum equation the rotation term is assumed to balance the pressure term (geostrophic balance). These assumptions lead to the following thermal boundary layer scale (subscript RS):

$$\delta_{RS} \sim Q^{1/3}\delta_R \sim Q^{1/4}\delta_{R_B}, \tag{3.11}$$

where the subscript B denotes fixed flux scales for δ_R in (3.8). *Stern* (1975) assumed the same momentum balance as RS. However, instead of incorporating the buoyancy equation, he proposed a balance in the E_k equation (4.8a) between the buoyancy flux term $\langle wb \rangle$ and the E_k dissipation $\nu\langle ||\boldsymbol{\nabla u}||^2 \rangle$. His main assumption was that $\langle wb \rangle$ is dominant throughout the entire thermal boundary layer whereas dissipation occurs mainly in the Ekman layer. This new balance leads to the following thermal boundary layer scale (subscript St):

$$\delta_{St} \sim Q^{3/4}\delta_R \sim Q^{1/2}\delta_{R_B}. \tag{3.12}$$

Note that for $Q \sim O(1)$ there is a three-term balance between the rotation, pressure and viscous terms in the horizontal components of (3.9), and based on (3.11), (3.12) the thermal boundary layer should still scale like δ_R.

Using oceanic, basin scale values on an f-plane ($L_y = 10^6$ m, $f = 10^{-4}$ s^{-1}) yields $Q = 130$ and 210 for molecular and turbulent values respectively (using parameters defined in § 3.3). The ocean is therefore rapidly rotating and it is of interest to examine solutions in the regime $Q \gg 1$. In all of the above scaling laws the f-plane approximation leads to constant Q. In the ocean the latitudinal variation in Coriolis force is clearly important. The correction to the above scaling can be incorporated simply by considering $Q = Q(y)$.

3.5 $\boldsymbol{x}$-Uniform RHC

In order to illustrate the effects of rotation, while suppressing baroclinic instability, we first examine unperturbed RHC solutions which are uniform in $\hat{\boldsymbol{i}}$. In these solutions, rapid rotation is expected to halt the lateral, return volume transport from the plume region at a distance of a Rossby radius of deformation (R_d) from the cold end ($y = L_y$). If the rotation rate is not too high, i.e. $Q \sim O(1)$, then $R_d \gg L_y$, and we expect little change from the non-rotating solution.

Figure 3.4(a) shows typical, steady state, $\boldsymbol{x}$-uniform density fields of RHC. For $Q = 1$ the solution is similar to the non-rotating one, in agreement with the laboratory results of *Hignett et al.* (1981); *Park and Whitehead* (1999). For $Q = 15$ however, the solution is substantially different with no apparent thermal boundary layer (or thermocline). In the interior, away from the lateral sides ($y = 0$, L_y) there is an extensive region in which the isopycnals touch both top and bottom boundaries. The corresponding, horizontally-averaged stratification (figure 3.4c) shows that for $Q = 15$ there is an increase in stratification throughout the domain with two local maxima, presumably near the top and bottom Ekman layers. The streamfunction (figure 3.4b) shows a substantial decrease in magnitude from the $Q = 1$ to the $Q = 15$ case, with an anti-clockwise circulation pattern next to the plume region. This structure develops because the heavy fluid in the cold end, which flows in the positive $\hat{\boldsymbol{i}}$ direction as it falls, is deflected away from the sidewall by the Coriolis force. Continuity then produces a compensating updraft adjacent to the sidewall producing the two-cell circulation pattern. This feature is enhanced with increasing rotation. Figure 3.5 shows that, unlike the non-rotating case (figure 3.2), diffusion is the dominant mechanism for lateral buoyancy flux in the rapidly rotating simulations outside the thin top and bottom Ekman layers.

In non-rotating HC the Nusselt number and Péclet number $Pe = \psi_{max}/\kappa$ should scale like $Ra^{1/5}$ (*Chiu-Webster et al.*, 2008). Figure 3.6 shows Nu and Pe versus $Ra^{1/5}$ for a set of $\boldsymbol{x}$-uniform RHC simulations in which Q varies between 0 at $y = 0$ to 2 at $y = L_y$. The good agreement between the numerical simulations and Rossby's scaling law confirm its applicability for $Q \sim O(1)$ simulations, even for varying Q (corresponding to laterally varying f) . Note that both RS (3.11) and St (3.12) scaling laws reduce to Rossby's scaling law in this regime. Similar analyses for a set of $Q > 1$ simulations (not shown) demonstrated no such agreement between any of the previously suggested scaling laws (3.11), (3.12) and the $\boldsymbol{x}$-uniform RHC simulations.

3.5.1 Analytical Model

The $\boldsymbol{x}$-uniform solutions shown in figure 3.4 motivate us to suggest the following analytical model in the interior region, away from the lateral boundaries where the buoyancy forcing is applied. This model is partly based on *Whitehead* (1981) model for shelf circulation and is essentially an extension of *Smith* (1976) solution for buoyancy-driven estuarine circulation.

Scaling the horizontal velocities using u ,$v \sim b_{\max}\alpha/f$ (assuming $L_x \sim L_y$), the pressure hydrostatically ($p \sim b_{\max}H$), and assuming $Pr \gg 1$, $\alpha^2 \ll 1$, $Q \sim O(1)$ and $Ra\alpha^5 \sim O(1)$, the dominant balance in (3.1) is

$$-f\,\tilde{v} = \nu\tilde{u}_{zz}, \tag{3.13a}$$

$$f\,\tilde{u} = -\frac{\partial p}{\partial y} + \nu\tilde{v}_{zz}, \tag{3.13b}$$

$$0 = -\frac{\partial p}{\partial z} + b, \tag{3.13c}$$

$$-\Gamma\tilde{v} = \kappa\tilde{b}_{zz}, \tag{3.13d}$$

$$\int_{-H}^{0} \tilde{v}dz = 0 \tag{3.13e}$$

where we have also assumed the ansatz

$$b = -\Gamma y + \tilde{b}(z), \qquad p = y\left(-\Gamma z + p_y^0\right) + \tilde{p}(z), \qquad \boldsymbol{u} = (\tilde{u}(z), \tilde{v}(z), 0). \tag{3.14}$$

Equation (3.13e) comes from the incompressibility condition. In (3.14), Γ is the (assumed) constant, lateral buoyancy gradient and p_y^0 is a constant representing the lateral pressure gradient at $z = 0$. We assume the buoyancy flux is confined to the corner regions away form the interior (where the solution is thought to apply), and we therefore suppose $\nabla b \cdot \hat{\boldsymbol{n}} = 0$ at the top and bottom. Free-slip is always assumed at the top boundary, and at the bottom boundary we apply either free-slip (in accordance with the numerical simulations) or no-slip. In either case inserting (3.13a) into (3.13d) leads to

$$\frac{\Gamma\nu}{f}\tilde{u}_{zz} = \kappa\tilde{b}_{zz}. \tag{3.15}$$

The boundary condition at the top is free slip, and both the bottom and top walls are taken to be insulating, so $\partial u/\partial z = 0$ at the bottom, irrespective of the bottom velocity boundary condition. Because $\tilde{u}_x = 0$ it is useful to define a streamfunction such that:

$$\tilde{v} = -\tilde{\psi}_z \qquad \text{and} \qquad \tilde{w} = \tilde{\psi}_y. \tag{3.16}$$

Inserting (3.16) into (3.13a), integrating once making use of (3.15), and substituting into $\partial/\partial z$ of (3.13b) we get

$$\tilde{\psi}_{4z} + \frac{4}{d^4}\tilde{\psi} = \frac{2\Gamma}{fd^2} \tag{3.17}$$

where the d is the Ekman depth defined in § 3.4. For free-slip top and bottom boundary conditions, the symmetry in both $\tilde{u}, \tilde{v}$ motivates the introduction of a new coordinate $z' = z + H/2$, since then $p_y^0 = 0$, simplifying the algebra. The solution to (3.17) in the new coordinate z' is

$$\tilde{u}(z') = \Gamma\left(\frac{z'}{f} + F_2(z')\,G_1 - F_1(z')\,G_2\right), \tag{3.18a}$$

$$\tilde{v}(z') = \Gamma(F_1(z')\, G_1 + F_2(z')\, G_2), \tag{3.18b}$$

$$\tilde{b}(z') = \frac{\Gamma\nu}{\kappa f}\tilde{u}(z'), \tag{3.18c}$$

where $F_{1,2}(z')$ and $G_{1,2}$ are given explicitly in (3.50).

The solution (3.18c) is correct up to a constant which vanishes in the limit $\alpha \to 0$. The solution for no-slip boundary condition at the bottom is described in (3.45)–(3.49).

In order to determine Γ for either of the bottom velocity boundary conditions one must apply conservation of flux in the form

$$|\mathcal{F}_{1/2}| = \int (\tilde{v}\tilde{b} + \kappa\Gamma)\,\mathrm{d}z, \tag{3.19}$$

where $|\mathcal{F}_{1/2}| = (\pi g/4\rho_0)S\sigma_z\sigma_y = (\sqrt{\pi}/4)\sigma_y B_{max}$ is the magnitude of the buoyancy source/sink determined from the numerical boundary condition defined in (3.5). Calculating the integral in (3.19) leads to

$$\Gamma^3\mathcal{H}_{fs} + \Gamma\kappa H = |\mathcal{F}_{1/2}| \tag{3.20}$$

where $\mathcal{H}_{fs}$ is a positive constant written explicitly in (3.51). Finding Γ therefore reduces to finding the single real root of the cubic (3.20).

The analytical model described above is valid when the ratio between the lateral extent of a typical sloping isopycnal Δ_y and the lateral extent of the domain L_y is small, so we write

$$\beta \equiv \frac{\Delta_y}{L_y} = \frac{\tilde{b}_{top} - \tilde{b}_{bot}}{\Gamma\, L_y} \ll 1 \tag{3.21}$$

as the condition of validity.

3.5.1.1 Rapidly Rotating analytical solution

It is illuminating to examine the analytical solution in the rapidly rotating limit $Q \gg 1$ which is most relevant to the oceanic regime. This limit corresponds to the regime $Ra\alpha^5 \gg 1$ using the scales leading to (3.13) with the lateral velocity $v \sim \nu/(fH^2)\, u$ (in this regime $v \ll u$), which makes the viscous term in (3.13b) negligible. This can be done by taking the limit $d \to 0$ of (3.18) in the free-slip case and of (3.45–3.49) in the no-slip case, leading to:

$$\tilde{u}_I = \frac{\Gamma z - p_y^0}{f}, \tag{3.22}$$

where the subscript I indicates that the rapidly rotating solution is in the interior, between the thin, top and bottom Ekman layers. For free-slip bottom boundary condition, using the same transformation as before ($z' = z + H/2$) leads to $p_y^0 = 0$ and z should be replaced by z' in what follows. For no-slip bottom boundary condition, $p_y^0 = -\Gamma H$ (assuming the bottom Ekman layer is thin so that the boundary condition is applied at $z = -H$). The remaining fields are

$$\tilde{\psi}_I = \nu \frac{\Gamma}{f^2}, \qquad \tilde{v}_I = 0, \qquad b_I \approx -\Gamma\, y + z\, Pr \left(\frac{\Gamma}{f}\right)^2. \tag{3.23}$$

Then (3.20) becomes

$$\Gamma \left(\frac{Pr^2}{f^4} \Gamma^2 + 1 \right) = \frac{|\mathcal{F}_{1/2}|}{\kappa H}, \tag{3.24}$$

and the validity condition (3.21) is now

$$\beta = Pr \alpha \frac{\Gamma}{f^2} \ll 1. \tag{3.25}$$

This condition is satisfied in both the ocean (using parameters defined in § 3) and in the numerical simulations.

If we scale Γ using $b_{\max}/L_y$ (3.24) can be written as

$$\left(Pr^2 Ro_T^2 + 1 \right) = \frac{|\mathcal{F}_{1/2}|}{\kappa \alpha b_{\max}}, \tag{3.26}$$

suggesting that the size of the lateral buoyancy gradient depends on $Pr^2 Ro_T^2$, where

$$Ro_T \equiv \frac{b_{\max}}{f^2 L_y}, \tag{3.27}$$

is the thermal Rossby number measuring the ratio between the length scale on which rotation is affecting buoyancy ($b_{\max}/f^2$) to the domain length (L_y). In the oceanic regime $Ro_T \sim O(1)$ and $Pr^2 Ro_T^2 \gg 1$. The corresponding lateral buoyancy gradient Γ in this regime is

$$\Gamma = \left(\frac{f^4 |\mathcal{F}_{1/2}|}{\kappa Pr^2 H} \right)^{1/3}. \tag{3.28}$$

Figure 3.7 shows a comparison between a steady-state, $\boldsymbol{x}$-uniform, interior buoyancy field, computed from a numerical simulation (a) and from the rapidly rotating analytical solution (3.23) (b). Good qualitative agreement is seen in the isopycnal slopes, although there is a difference in absolute values. This difference is expected to vanish in the limit $\alpha \to 0$. The horizontally averaged, interior stratification (c) and streamfunction (d) are shown along with the predicted analytical values in dashed lines. The maximal difference between theory and simulation in both cases is $\sim 10\%$ in the bottom of the top Ekman layer. The numerically computed lateral buoyancy gradient normalized by B_{max}/κ at $z/H = -1/2$ is $\Delta b/\Delta y = 0.054$. The normalized analytical prediction (3.20) gives $\Gamma = 0.055$. Similar accuracies were obtained for all other $\boldsymbol{x}$-uniform RHC simulations.

3.5.1.2 Stability Analysis

The sloping isopycnals of the rapidly-rotating $\boldsymbol{x}$-uniform solutions produce greatly enhanced available potential energy and, consequently, one expects the flow to be baroclinically unstable. Figure 3.8 shows a comparison of the available potential energy density, $\mathcal{E}_a$, for non-rotating HC (top) and for $\boldsymbol{x}$-uniform RHC (bot). $\mathcal{E}_a$ is the positive definite spatial contribution of available potential energy, which integrates to E_a (3.4d) (*Holliday and McIntyre*, 1981; *Andrews*, 1981; *Scotti et al.*, 2006; *Roullet and Klein*, 2009; *Molemaker and McWilliams.*, 2010; *Winters and Barkan*, 2013).

The tendency of the $\boldsymbol{x}$-uniform flow to become unstable can be analyzed by performing linear-stability-analysis on the rapidly rotating analytical solution (3.22)–(3.23). The non-dimensional parameter that indicates the type of instability with the largest growth rate is the Richardson number (*Stone*, 1966). In the rapidly rotating solution $Ri \equiv \tilde{b}_{I_z}/\tilde{u}_{I_z} = Pr > 1$. This suggests that the Quasigeostrophic (QG) modes have the largest growth rate (*Stone*, 1966), although other modes of instability are also present. Nevertheless, if the Ekman layers are ignored the rapidly rotating solution (§5.1) is the basic state of the Eady problem (*Eady*, 1947) and the QG approximation does a good job in predicting the largest wavelength of instability (*Cessi and Fantini*, 2004). The resulting QG predictions for the critical and maximal wavelengths of instability are $\lambda_c = 2.62R_d$ and $\lambda_m = 3.9R_d$ respectively, where $R_d \equiv NH/f = \sqrt{Pr}\Gamma H/f^2$ is the Rossby radius of deformation. These predictions were used to guide us in choosing sufficiently large transverse domains (L_x) for the baroclinically-active RHC simulations (§ 6). Given resource constraints, baroclinically-active RHC simulations were carried out using $L_x \sim L_y \geq 10R_d$.

Note that the critical rotation rate value (Q_c) above which baroclinic instability is expected to develop depends on the other non-dimensional parameters that govern RHC (4.4). *Hignett et al.* (1981) have performed a linear stability analysis which accounted for the top Ekman layer as well. They found the following relation for the critical rotation rate

$$Q_c > \left(Pr(\frac{R_d}{L_x})^2\right)^{-4/11}. \tag{3.29}$$

Given the Pr of our simulation and the requirement $L_x \sim L_y \geq 10R_d$, we expect instability to occur for $Q_c > 2.63$.

3.6 Baroclinically-Active RHC

We now turn our attention to simulations of RHC with transverse variations, which allow for baroclinic instability and the generation of baroclinic eddies that release the available potential energy stored in the sloping isopycnals. The differences between these simulations and the $\boldsymbol{x}$-uniform ones are the small perturbation to the forcing term (3.7).

3.6.1 Transformed Eulerian-mean (TEM) analysis

The TEM formalism, introduced by *Andrews and McIntyre* (1976, 1978) provides a useful framework for discussing eddy effects under a wide range of conditions. For channel flows the TEM equations rely on the transformation from the Eulerian $\boldsymbol{x}$-mean velocity $\overline{\boldsymbol{u}}$ to the residual mean velocity $\overline{\boldsymbol{u}}_{res}$, following

$$\overline{\boldsymbol{u}}_{res} = \overline{\boldsymbol{u}} + \overline{\boldsymbol{u}}^* = \overline{\boldsymbol{u}} + \nabla \times \hat{\boldsymbol{i}}\psi^*, \tag{3.30}$$

where $\overline{\boldsymbol{u}}^*, \psi^*$ are the velocity, streamfunction associated with the eddies and $\hat{\boldsymbol{i}}$ is the unit vector in the transverse direction. Consider the $\boldsymbol{x}$-average of (4.1b),

$$\frac{\partial \overline{b}}{\partial t} + \overline{\boldsymbol{u}} \cdot \nabla \overline{b} = \kappa \nabla^2 \overline{b} - \nabla \cdot \boldsymbol{F}\{b\}, \tag{3.31}$$

where $\boldsymbol{F}\{b\} = \overline{\boldsymbol{u}' \, b'}$ is the eddy flux of buoyancy. Under the transformation (3.30), (3.31) becomes

$$\frac{\partial \overline{b}}{\partial t} + \overline{\boldsymbol{u}}_{res} \cdot \nabla \overline{b} = \kappa \nabla^2 \overline{b} - \nabla \cdot \boldsymbol{F}_{res}\{b\}, \tag{3.32}$$

where $\boldsymbol{F}_{res}\{b\}$ is the "residual eddy flux" defined as

$$\boldsymbol{F}_{res}\{b\} = \boldsymbol{F}\{b\} - \psi^* \hat{\boldsymbol{i}} \times \nabla \overline{b}. \tag{3.33}$$

Andrews and McIntyre (1976) introduced the coordinate-independent form of the eddy streamfunction

$$\psi^* = \frac{\overline{v'b'}\,\overline{b}_z - \overline{w'b'}\,\overline{b}_y}{\overline{b}_y^2 + \overline{b}_z^2}, \tag{3.34}$$

which eliminates entirely the eddy flux component that is directed along $\overline{b}$ contours (skew flux). Consequently, if the flow is completely adiabatic then the choice (3.34) identically sets $\boldsymbol{F}_{res}\{b\} = 0$. In the limit of small isopycnal slope ($-\overline{b}_y/\overline{b}_z \ll 0$) (3.34) reduces to the QG form

$$\psi^*_{QG} = \frac{\overline{v'b'}}{\overline{b}_z}. \tag{3.35}$$

Figure 3.9 shows the statistically steady, $\boldsymbol{x}$-averaged, density (a), streamfunction (b), residual streamfunction (c) and horizontally averaged stratification (d) for a typical baroclinically-active RHC simulation. Time averages over the last quarter of a diffusive time ($H^2\kappa^{-1}$) were carried out prior to computing the fields. The $\boldsymbol{x}$-averaged density plot shows that a thermal boundary layer is again apparent. Most of the surface outcropping isopycnals no longer intersect the bottom boundary, in contrast to the $\boldsymbol{x}$-uniform RHC simulations (figure 3.4). The horizontally-averaged stratification in the baroclinically-active RHC solution shows a maximum at a depth similar to that of non-rotating HC, and larger values of N^2 at depth. Rossby's scaling law (3.8) better matches that maximum than RS scaling law (3.11) and St scaling law (3.12) (dashed, vertically dashed, and dot-dashed lines in 3.9c). The $\boldsymbol{x}$-averaged streamfunction shows multiple overturning cells, in contrast with the single large overturning cell of the non-rotating HC simulation (figure 3.1). The residual streamfunction $\psi_{res} = \overline{\psi} + \psi^*$ is an order of magnitude larger than the $\boldsymbol{x}$-averaged streamfunction, implying that the contribution of the mean flow to the buoyancy transport is negligible in these solutions. Figure 3.10 further supports this point, showing that it is the eddy buoyancy flux $\overline{v'b'}$ that dominates the lateral buoyancy flux in this flow.

Figure (3.11 top) shows the residual streamfunction $\psi_{res} = \overline{\psi} + \psi^*$, the eddy streamfunction ψ^* (middle) and the QG eddy streamfunction ψ^*_{QG} (bottom) for a baroclinically-active RHC simulation with a higher Ra_B and smaller aspect ratio than in figure 3.9 (simulation 15 in table 3.1). The overall solution is generally similar to the lower Ra_B, higher aspect ratio simulation (see § 6.2 for further discussion). As before, the residual streamfunction is dominated by the eddy component ψ^*, which, aside for thin top and bottom boundary layers, agrees well with the QG form (3.35). Note that the sense of the eddy induced circulation is counter clockwise. This is in contrast to the $\boldsymbol{x}$-uniform solutions where the sense of the circulation was clockwise (figure 3.4b, bottom). Because ψ_{res} contours do not align with density contours the eddy flux of buoyancy has a non-negligible diabatic component. Given the dominance of ψ^*_{QG} in the interior and that of $\overline{v'b'}$ shown in figure 3.10, (3.19) becomes:

$$|\mathcal{F}_{1/2}| \approx \int (\overline{v'b'}) dz \approx \int (v^* \overline{b})\, dz \tag{3.36}$$

(after an integration by parts and because ψ^* vanishes at the top). (3.36) states that the lateral buoyancy flux in this flow is predominantly due to 'advection' by the eddy velocity v^*.

3.6.2 The effects of Ro_T on the stratification

Figure (3.12) shows a comparison between horizontally averaged stratification of two baroclinically-active RHC simulations with different values of Ro_T (3.27) and the corresponding non-rotating HC one. In all cases the maximum stratification (thermocline depth) is at about $z/H \sim -0.1$ which fits the scaling laws proposed by Rossby (3.8) better than the other suggested scaling laws (3.11), (3.12) (the corresponding boundary layer scale would be $1.5 - 4$ times deeper depending on the value of Q). Clearly, deep stratification is increased for both of the RHC simulations. Note however, that the maximum in stratification is larger in magnitude for the baroclinically-active RHC simulation with higher Ro_T. This difference is best demonstrated when comparing the ratio N/f in these two simulations. For the simulation with $Ro_T = 0.04$, $N/f \sim O(1)$ in the thermal boundary layer whereas in the simulation with $Ro_T = 0.25$, $N/f \sim O(10)$. In the ocean typical values range between $N/f = 20 - 50$ in the thermocline and decreasing to $N/f = 5$ at depth (*Marshall and Schott*, 1999). The above comparison demonstrates that the value of Ro_T affects the nature of the solution, particularly with respect to the stratification.

3.6.3 Steady State and Bottom Drag

Figure 3.13 shows a comparison between two baroclinically-active RHC simulations, with the only difference being the inclusion of the bottom drag term of the form (4.19) in (4.1a). In contrast to the statistical steady state that is achieved in the simulation with bottom drag, there is a gradual increase in E_k for the simulation without bottom drag. In these baroclinically active simulations, energy can cascade to larger scales (*Salmon*, 1980), and bottom drag is necessary to halt that inverse energy cascade (*Vallis*, 2006). Traditionally the bottom drag r is a parametrization of the bottom Ekman layer and has a magnitude $r \sim H^{-1}\sqrt{\nu f/2}$ (*Vallis*, 2006). The wavenumber k_r at which the inverse energy cascade is halted scales like $k_r \sim (r^3\mathcal{E}^{-1})^{1/2}$, where $\mathcal{E}$ is the energy supply rate to the system. The Rossby deformation wavenumber k_d associated with a typical eddy length scale (*Vallis*, 2006), can be estimated based on the rapidly rotating solution (3.23). Ideally the bottom drag magnitude should be chosen such that $2\pi L_y^{-1} < k_r < k_d$, in order to ensure that the baroclinic eddies do not grow and occupy the entire domain. For 2D turbulence simulations $k_r \approx (3\mathcal{B})^{3/2}(r^3\mathcal{E}^{-1})^{1/2}$ with the constant $\mathcal{B} = 5.8$ (*Smith et al.*, 2002), so that $(3\mathcal{B})^{3/2} \gg 1$. In RHC the energy generation term at steady state $\mathcal{E} = \kappa H^{-1}\Delta\widehat{b} \leq B_{max}$, so one can try to estimate

k_r for these simulations. However, it is hard to accurately approximate $\mathcal{B}$ in our three dimensional, non-hydrostatic, Boussinesq simulations. We thus compared simulations of $\boldsymbol{x}$-uniform RHC with a no-slip bottom boundary condition to ones with bottom drag (not shown), and determined that the bottom drag magnitude that best parameterizes no-slip boundary conditions is $r = 1.57H^{-1}\sqrt{\nu f/2}$.

3.7 Energetics of RHC

Paparella and Young (2002) established a bound on the volume averaged dissipation rate $\epsilon \equiv \nu\langle||\boldsymbol{\nabla u}||^2\rangle$ by combining the steady-state balance in (4.8a) and (4.8b) with no bottom drag ($r = 0$) to yield

$$\epsilon = \frac{\kappa}{H}\Delta\widehat{b} \leq \frac{\kappa}{H}b_{max}. \tag{3.37}$$

With bottom drag, the left hand side of (3.37) becomes $\epsilon+\epsilon_d$, where the dissipation due to bottom drag $\epsilon_d \equiv \langle f_b(z)|\boldsymbol{u}_H|^2\rangle$. In all the figures and discussion that follow in the next sections, although we computed $\epsilon + \epsilon_d$ explicitly, we refer to it simply as ϵ because in all of our baroclinically-active RHC simulations $\epsilon \gg \epsilon_d$.

Using oceanic parameters defined in § 3.3, $\kappa H^{-1}b_{\mathrm{max}} = 1 \times 10^{-12}$ W kg^{-1} for molecular diffusivity and 1×10^{-10} W kg^{-1} for turbulent diffusivity. These values are 1–3 orders of magnitudes less than the observed values in the interior of the ocean, 1×10^{-9} W kg^{-1}.

Winters and Young (2009) established a non-rigorous bound on the positive definite term $\Phi_d \equiv \kappa\langle(\mathrm{d}z_*/\mathrm{d}b)|\nabla b|^2\rangle$, defined by *Winters et al.* (1995) as the rate of change of the background potential energy E_b due to diabatic processes. At steady state, the balance in (3.4c) is

$$\Phi_d = \frac{\kappa}{H}\widehat{z_*(b_{top})b_z}(0) \leq \kappa\frac{b_{max}}{\delta}. \tag{3.38}$$

Winters and Young (2009) estimated the thinnest possible scale upon which diabatic processes take place as $\delta \sim Pr\kappa^{2/3}b_{max}^{-1/3}$, leading to

$$\Phi_d \leq \frac{\kappa^{1/3}b_{max}^{4/3}}{Pr}. \tag{3.39}$$

The mixing efficiency in a Boussinesq flow is often defined as the ratio between the dissipation of E_a to that of the sum $E_a + E_k$, and is given by (*Peltier and Caulfield*, 2003)

$$\gamma = \frac{\Phi_d - \frac{\kappa}{H}\Delta\widehat{b}}{\Phi_d - \frac{\kappa}{H}\Delta\widehat{b} + \epsilon}. \tag{3.40}$$

At steady state, using (3.37) and (3.39),

$$\gamma \leq 1 - \frac{\delta}{H} = 1 - \frac{Pr^{2/3}}{Ra^{1/3}\alpha}. \tag{3.41}$$

The bounds on γ and Φ_d, may in fact be less restrictive, as pointed out by *Scotti and White* (2011). If, instead, $\delta \sim \delta_R$, the power in (3.39), and (3.41) should be reduced to 1/5. Note that for the boundary condition described in (3.2), the above bounds are only known *a posteriori*. Similar bounds can be established using the prescribed maximal buoyancy flux B_{max}. Finally, the above bounds assume nothing about the velocity boundary conditions and only require that the flow reaches a statistical steady state.

3.7.1 The mechanical energy cycles of RHC

Figure 3.14 shows a comparison between E_a (a), ϵ (b), $\Phi_d - \kappa H^{-1}\Delta\widehat{b}$ (c) and γ (d), for non-rotating HC, $\boldsymbol{x}$-uniform RHC, and baroclinically-active RHC. The amount of volume-averaged available potential energy increases five fold when rotation is introduced, but the increase is reduced when baroclinic instability is active. Nevertheless, $\langle E_a \rangle$ values are still almost twice as large for baroclinically-active RHC compared with non-rotating HC. The same is true for the volume averaged dissipation, where the baroclinic eddies (dashed gray line in b) contribute much more to the dissipation than the $\boldsymbol{x}$-mean. Under the Boussinesq approximation with a linear equation of state (see *Tailleux* 2009 for a more general discussion) the difference $\Phi_d - \kappa H^{-1}\Delta\widehat{b}$ indicates the rate of conversion from E_a to E_b in these flows (*Winters & Young* 2009 and figure 3.15). For fully developed stably stratified turbulent flows $\Phi_d \gg \kappa H^{-1}\Delta\widehat{b} > 0$ so that most of the conversion is accomplished by mixing. In the present simulations $\Phi_d - \kappa H^{-1}\Delta\widehat{b}$ is positive for non-rotating HC, negative for $\boldsymbol{x}$-uniform RHC, and positive again for baroclinically-active RHC.

The corresponding γ values are ~ 0.7, ~ -1 and ~ 0.17 respectively. The reason for the negative γ values in $\boldsymbol{x}$-uniform RHC can be understood qualitatively by examining (3.41), and noting that $\gamma < 0$ requires $\delta > H$, or no thermal boundary layer. Alternatively, note that δ in (3.38), represents the scale at which diabatic processes take place. Because diffusion is the mechanism which fluxes heat laterally in this flow (figure 3.5), this suggests that $\delta \sim L_y$ and, consequently, that small aspect ratios ($\alpha < 1$) can support negative γ values. In this case, viewing γ as the 'mixing efficiency' is misleading, because diabatic processes act on large scales, as opposed to the small scales which are often associated with mixing processes. Quantitatively we can use the rapidly-rotating, analytical model described in § 3.5.1.1 to compute the different terms in (3.40) explicitly:

$$\frac{\kappa}{H}\Delta\widehat{b} = \frac{\kappa}{H}\left(\frac{1}{L_y L_x}\int_0^{L_y}\int_0^{L_x}\left(b_I(top) - b_I(bot)\right)\mathrm{d}y\,\mathrm{d}x\right) = \nu\left(\frac{\Gamma}{f}\right)^2, \tag{3.42a}$$

$$\epsilon = \nu\left(\frac{1}{HL_yL_x}\int_0^{L_x}\int_0^{L_y}\int_{-H}^{0}\left(\frac{\partial u_I}{\partial z}\right)^2\mathrm{d}x\,\mathrm{d}y\,\mathrm{d}z\right) = \nu\left(\frac{\Gamma}{f}\right)^2, \tag{3.42b}$$

$$\Phi_d \approx \frac{1}{HL_yL_x}\int_0^{L_x}\int_0^{L_y}\int_{-H}^{0}\frac{\kappa[(\partial b_I/\partial y)^2 + (\partial b_I/\partial z)^2]}{\mathrm{d}b/\mathrm{d}z_*}\mathrm{d}x\,\mathrm{d}y\,\mathrm{d}z = \kappa\alpha\left(\Gamma + Pr^2\frac{\Gamma^3}{f^4}\right), \tag{3.42c}$$

where $\mathrm{d}b/\mathrm{d}z_*$ was approximated using a linear profile

$$\frac{\mathrm{d}b}{\mathrm{d}z_*} \approx \frac{b_{I_{max}} - b_{I_{min}}}{H} = \Gamma\left(\frac{1}{\alpha} + Pr\frac{\Gamma}{f^2}\right) \approx \frac{\Gamma}{\alpha}. \tag{3.43}$$

The final simplification in (3.43) results from (3.25). As expected from a steady state solution $\kappa H^{-1}\Delta\widehat{b} = \epsilon$, and thus $\gamma = 1 - \kappa H^{-1}\Delta\widehat{b}\Phi_d^{-1}$. This ratio has to be greater than 1 for γ to be negative. Using (3.42) leads to

$$\frac{\frac{\kappa}{H}\Delta\widehat{b}}{\Phi_d} = \frac{\beta}{\alpha^2} + \frac{1}{\beta} \tag{3.44}$$

From (3.25) $\beta^{-1} \gg 1$. In order for $\beta\alpha^{-2} \gg 1, \alpha \ll Pr\Gamma/f^2$ which is satisfied in all of the numerical simulations as well as for typical oceanic parameters defined in § 3.3. If one scales $\Gamma \sim b_{\max}/L_y$ and from $(\partial/\partial z)$ of (3.23), $\partial b_I/\partial z = Pr\,(\Gamma/f)^2 \sim H^{-1}b_{\max}$ then demanding that $\alpha \ll Pr\Gamma/f^2$ is equivalent to requiring $\alpha^2 \ll 1$. This means that $\boldsymbol{x}$-uniform RHC, with small aspect ratios is expected to yield negative γ

values. Figure 3.15 shows the energy cycle of HC (*Winters and Young*, 2009) along with the various energy transfer rates. The dashed black arrow shows the change to the lower cycle in the rapidly rotating regime when eddies are suppressed.

In baroclinically-active RHC positive values of $\Phi_d - \kappa H^{-1}\Delta\widehat{b}$ indicate that the length scale at which diabatic processes take place is, as in non-rotating HC, much smaller than H so that a thermal boundary layer is again part of the solution and γ can again be viewed as the mixing efficiency. As a result the direction of the lower cycle in figure 3.15 is as was originally proposed by *Winters and Young* (2009). This demonstrates the importance of the eddies in the formation of the thermal boundary layer from an energetic point of view.

Figure 3.16 shows a comparison between $\langle E_k \rangle$ (a), and $\langle wb \rangle$ (b), for non-rotating HC, $\boldsymbol{x}$-uniform RHC, and baroclinically-active RHC. The volume averaged kinetic energy increases ten fold when rotation is introduced but the increase is somewhat reduced when baroclinic eddies are active. The same is true for $\langle wb \rangle$ although the increase in the $\boldsymbol{x}$-uniform case is not as large. In $\boldsymbol{x}$-uniform RHC, the flow is primarily in the $\boldsymbol{x}$ direction, in fact 99% of $\langle E_k \rangle$ is due to $u^2/2$ (not shown). Figure 3.16(c) shows that baroclinically-active RHC still has $\langle E_k \rangle$ and $\langle wb \rangle$ values two-three times larger than non-rotating HC. Furthermore it is evident that the contribution to both the vertical buoyancy flux and the kinetic energy is dominated by the eddies ($\overline{w'b'}$, E_k'), as is the case for kinetic energy dissipation ϵ' (figure 3.14c). This suggests that each individual term in the kinetic energy equation (4.8a) and the kinetic energy reservoir (gray shadow in figure 3.15) are dominated by the eddy field.

Figure 3.17 shows snapshots of horizontal slices taken at the base of the thermal boundary layer ($z/H \sim -0.1$) from a typical baronclinally-active RHC simulation. The left panel shows the density field exhibiting eddying structures of different scales. The right panel shows the corresponding diabatic processes term Φ_d (3.38, 3.39) which is associated with diapycnal mixing. Note that areas of elevated mixing correspond well with the edges of the eddies and eddy filaments suggesting that eddies dominate the diabatic processes (mixing) in these flows. In a statistical steady state Φ_d is balanced by the external energy term $H^{-1}\kappa\,\widehat{z_* b_z}$

(3.4c) which supplies energy to the available potential energy (E_a) reservoir (figure 3.15). The eddy dominance of Φ_d and wb along with the statistical steady state balance in (3.4c) and the fact that $\Phi_d > H^{-1}\kappa\Delta\widehat{b}$ (figure 3.14c) suggest that each individual term in the E_a equation and the E_a reservoir are dominated by the eddy field as well.

3.8 Summary and Discussion

Our main focus in this paper was to examine the effects of rotation on HC. In order to understand these effects with and without baroclinic instability, we have designed the RHC simulations in two steps. First, we analyzed $\boldsymbol{x}$-uniform RHC simulations, in which baroclinicity was suppressed (§ 3.5). Second, we examined simulations in which we allowed for baroclinic instability to ensue (§ 3.6). Our results show that rapid rotation and baroclinic instability greatly alter the steady state of non-rotating HC and thus are essential components of process-based models of the overturning circulation and thermal structure of the ocean.

In the moderately rotating regime ($Q \sim O(1)$), the steady solution is very similar to the non-rotating one, as was shown by the laboratory experiments of *Hignett et al.* (1981) and *Park and Whitehead* (1999). This solution supports a thin thermal boundary layer, a single overturning circulation cell, and weak abyssal stratification that are all well described by Rossby's scaling law (3.8).

In the rapidly rotating regime ($Q \gg 1$), however, the $\boldsymbol{x}$-uniform solutions support no thermal boundary layer, weaker overturning circulation, and greater values of stratification (N^2), that extend throughout the entire domain depth. The full-depth penetrating plume that transports cold fluid laterally along the bottom boundary in the non-rotating case is arrested by about a distance R_d away from the wall in the rapidly rotating case, resulting in sloping isopycnals that occupy an extensive portion of the lateral domain. None of the previously suggested scaling laws (3.11), (3.12) accurately describe these solutions. An analytical model (§ 3.5.1) can very well predict the interior stratification, circulation, and lateral buoyancy gradient as long as the lateral extent of a typical sloping isopycnal is smaller than the domain length (3.21). Two main insights are gained from the analytical model. First, the interior, ‘eddy-less’, lateral buoyancy gradient $\partial b/\partial y$ is, to a good approximation, constant. Second, the non-dimensional number Ro_T (3.27) is important to the nature of the solution. Note that the analytical model can easily be expanded to account for stress at the top and for different distributions of surface buoyancy flux.

The lateral buoyancy flux in the rapidly-rotating, $\boldsymbol{x}$-uniform solutions is dominated by diffusion and not advection, as was the case in the non-rotating and moderately rotating solutions. From an energetic point of view, this means that diffusion acts to build up available potential energy, resulting in negative values of $\Phi_d - H^{-1}\kappa\Delta\widehat{b}$ and γ (3.40). Increased values of E_a and ϵ compared with non-rotating solutions indicate that rapid rotation enables the extraction of more available potential energy compared with non-rotating HC with the same buoyancy forcing. These $\boldsymbol{x}$-uniform simulations, however, are unstable and are used here primarily to provide insight into the key features of the mean flow. Detailed linear stability analysis was carried out analytically for $Pr = Ri > 1$ (§ 3.5.2), in order to predict the horizontal scale of the most unstable mode. The transverse scale $L_x \geq 10R_d$ was used in the baroclinically-active simulations to allow the formation of enough eddies within the domain.

In the baroclinically-active RHC solution a thermal boundary layer is again supported (compared with the $\boldsymbol{x}$-uniform simulations), abyssal stratification is increased and multiple overturning cells are formed (compared with non-rotating simulations). Analyzing these solutions using a TEM framework shows the dominance of the eddy streamfunction in transporting buoyancy in these flows. The relative contribution of the mean flow is completely negligible. The interior eddy streamfunction is very well represented by the quasi geostrophic (QG) form ψ^*_{QG} (3.35), suggesting the isopycnal slope is small. Because the residual streamfunction contours intersect buoyancy contours throughout the interior of the flow the eddy buoyancy fluxes have a non-negligible diabatic component. This is in contrast to channel flows that are forced by surface stress (wind) as well as buoyancy fluxes (see for example *Marshall & Radko*, 2003). A good measure of stratification in these flows is the ratio N/f. This ratio increases for increasing Ro_T. Note, that Ro_T can be expressed in terms of the other non-dimensional numbers that govern this problem (specifically $Ro_T \sim Ra^{1/5}Q^{-2}Pr^{-1}$). The solution dependence on Ro_T thus suggests that the ratio between the non-dimensional parameters that govern RHC is important in addition to their absolute magnitudes. Qualitatively, it appears that previously suggested scaling laws (3.11), (3.12) overestimate the thermal boundary layer depth in these flows.

The lateral buoyancy flux is dominated by eddy flux ($\overline{v'b'}$), where perturbations are from an $\boldsymbol{x}$ average. In terms of a TEM framework this means that buoyancy is predominantly 'advected' by the eddy velocity v^* (3.36). The kinetic and available potential energy reservoirs and the terms in the evolution equations (4.8a, 3.4d) are dominated by the eddy field as well. The difference $\Phi_d - H^{-1}\kappa\Delta\widehat{b}$ is positive for baroclinically-active RHC, demonstrating the importance of the eddies in mixing the fluid. The value of γ, which can now be interpreted as a mixing efficiency, is reduced from ~ 0.7 in non-rotating HC to ~ 0.17, a value similar to that commonly assumed in small scale stratified turbulence and in the ocean. Although the energy bounds (3.37), (3.39), (3.41) hold, reaching a steady state is no longer independent of boundary conditions. Bottom drag (used to parametrize the bottom Ekman layer resulting from no-slip boundary conditions) is needed to allow the flow to equilibrate, at least over diffusive time scales (H^2/κ).

The re-establishment of the thermal boundary layer in the baroclinically-active simulation compared with the $\boldsymbol{x}$-uniform ones suggests that the eddies play an important role in the thermal boundary layer formation. Eddies are responsible for most of the vertical and lateral buoyancy fluxes in the flow, overcoming the diffusive dominance of the $\boldsymbol{x}$-uniform simulations that do not support a thermal boundary layer. Furthermore, we hypothesize that it is the combined effect of the lateral transport of the eddies and the depth-dependent buoyancy of the negatively buoyant plume that set the deep stratification in this flow.

Because the kinetic and available potential energy are dominated by eddies ($E_k \sim E'_k$, $E_a \sim E'_a$), the mixing efficiency is close to values typically reported for actively turbulent flows, and bottom drag appears to be necessary to halt the inverse energy cascade and achieve a statistically steady state, the flow has the main characteristics of geostrophic turbulence. This observation does not contradict *Paparella and Young* (2002) 'anti-turbulence' theorem, which is based on a definition of three-dimensional turbulence consistent with a Kolmogorov inertial subrange. The geostrophically turbulent nature of baroclinically-active RHC is a critical feature that distinguishes it from non-rotating HC and emphasizes the importance of rapid rotation in relating these process based models to the real ocean.

The importance of baroclinic eddies to the ocean's thermocline, stratification and overturning circulation is a concept well studied by multiple authors in both laboratory experiments (*Marshall et al.*, 2002) and numerical simulations using general circulation models (GCMs) of different resolutions and configurations (see for example *Henning & Vallis* 2004; *Wolfe & Cessi* 2010). The hydrostatic approximation and parameterization of convection via 'convective-adjustment', which are typical of GCMs, reduce the detail by which processes such as entrainment and mixing in the negatively buoyant plume can be represented. These processes are thought to be of great importance *Hughes et al.* (2009); *Stewart* (2012).

The applicability of DNS that resolve such processes (like the ones described in this paper) to large scale ocean dynamics is, however, open to question. The *Ra* number, aspect ratio, and rotation rates (Q) presented here are nowhere near those observed in the ocean. Nevertheless, we argue that understanding physical mechanisms such as the combined effects of baroclinic eddies, the negatively buoyant plume and, in future work, mechanical forcing can lead to insights into oceanic processes.

3.9 Acknowledgements

Discussions with William Young were much appreciated and gratefully acknowledged. We would like to thank Caroline Papadopoulos for continuous technical support which made this work possible. This work was supported by the National Science Foundation (grant number OCE-0926481). This chapter has been published in: **Barkan, R.**, Winters, K. B., and Llewellyn Smith, S. G. (2013). Rotating Horizontal Convection. *J. Fluid Mech.*, 723, 556-586.

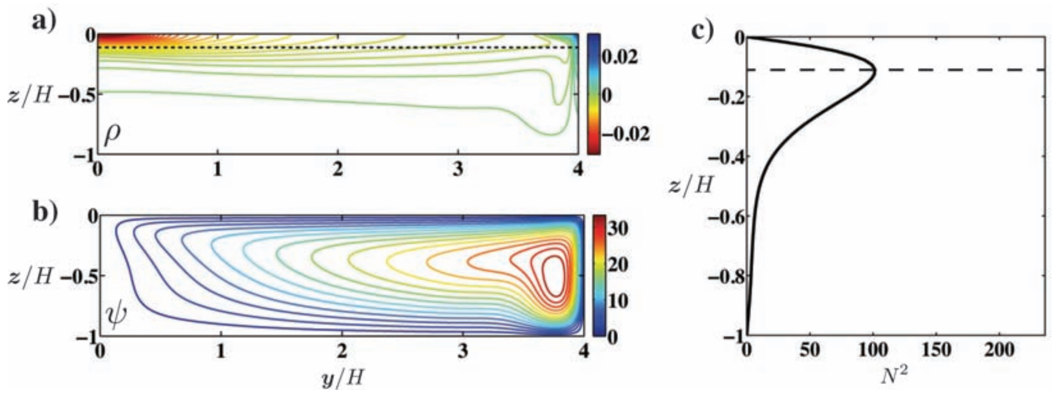

Figure 3.1: Steady state, $\boldsymbol{x}$-averaged density normalized by $HB_{max}\rho_0/g\kappa$ (a), streamfunction normalized by κ (b), and horizontally averaged interior stratification normalized by $(B_{max}/L_y^2)^{2/3}$ (c) for simulation 1. Dashed lines represent the thermal boundary layer depth according to Rossby's scaling law (3.8).

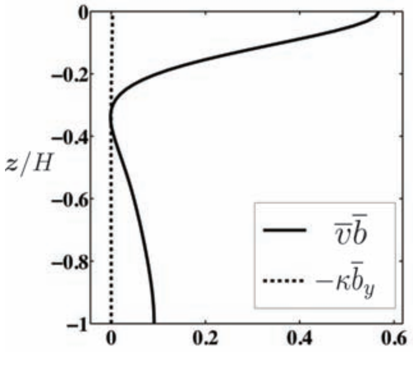

Figure 3.2: Lateral, $\boldsymbol{x}$-averaged, advective (solid) and diffusive (dash) buoyancy flux at $y = L_y/2$, for the simulation in figure 3.1. Fluxes are normalized by B_{max}.

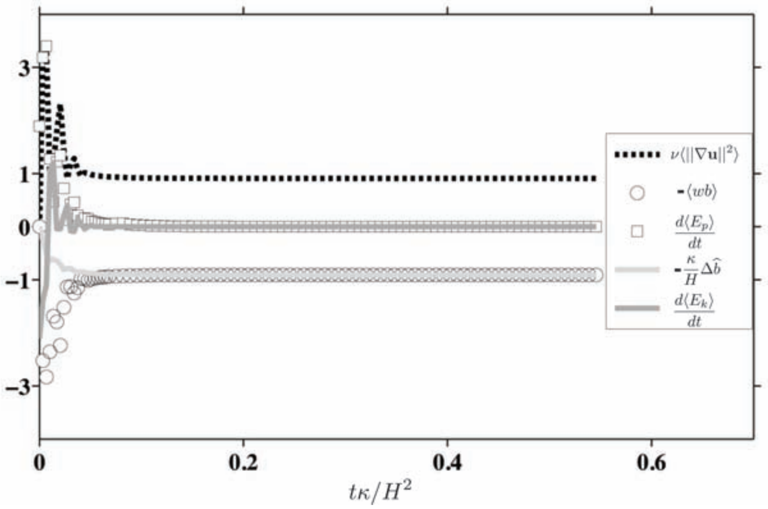

Figure 3.3: Time series of the different terms in (4.8a), (4.8b) normalized by $|\langle wb\rangle|$, for simulation 2.

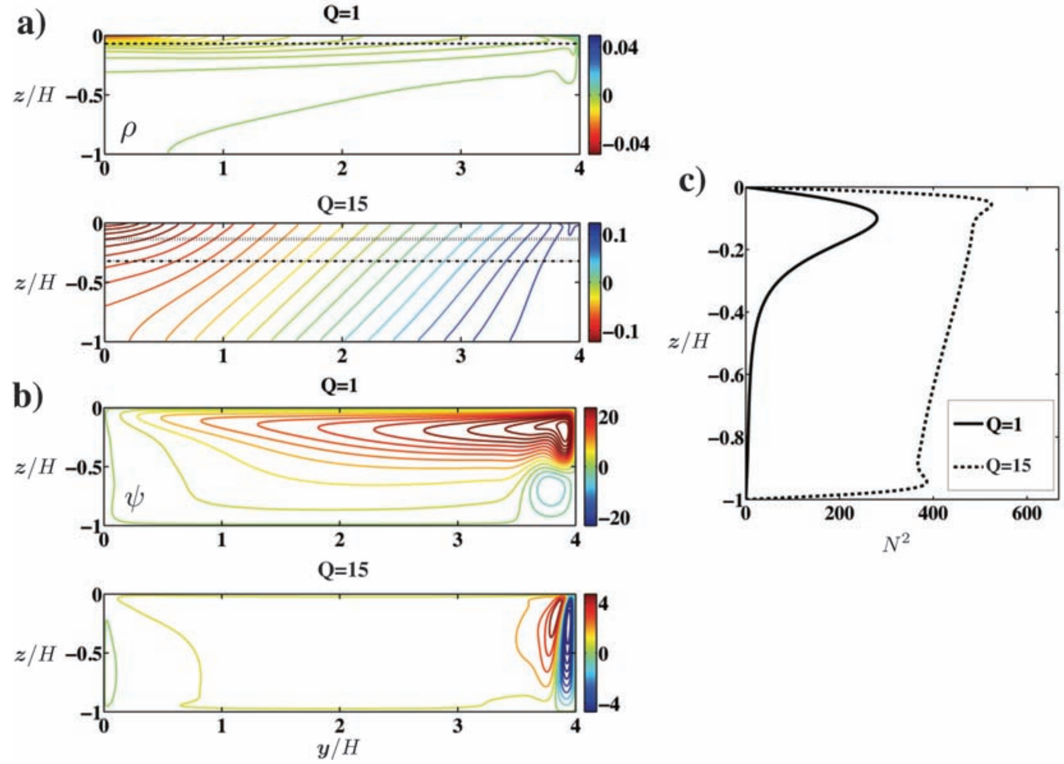

Figure 3.4: Steady-state $\boldsymbol{x}$-averaged density normalized by $HB_{max}\rho_0/g\kappa$ (a), streamfunction normalized by κ (b), and horizontally averaged, interior stratification normalized by $(B_{max}/L_y^2)^{2/3}$ (c) for $\boldsymbol{x}$-uniform RHC. Dashed line (a, top) represents Rossby's scaling law (3.8) for the $Q = 1$ solution (simulation 8). Vertically-dashed and dot-dashed lines (a, bottom) represent Robinson & Stommel's scaling law (3.11) and Stern's scaling law (3.12), respectively, for the $Q = 15$ solution (simulation 10).

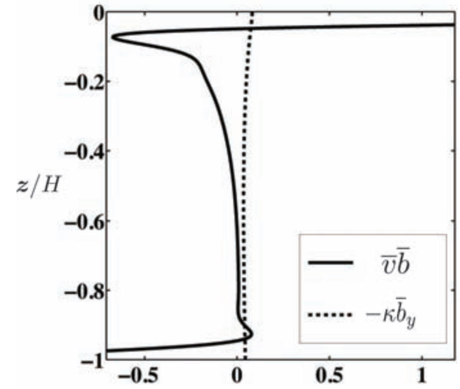

Figure 3.5: Lateral, $\boldsymbol{x}$-averaged, advective (solid) and diffusive (dashed) buoyancy flux at $y = L_y/2$, for simulation 10 ($Q = 15$). Fluxes are normalized by B_{max}.

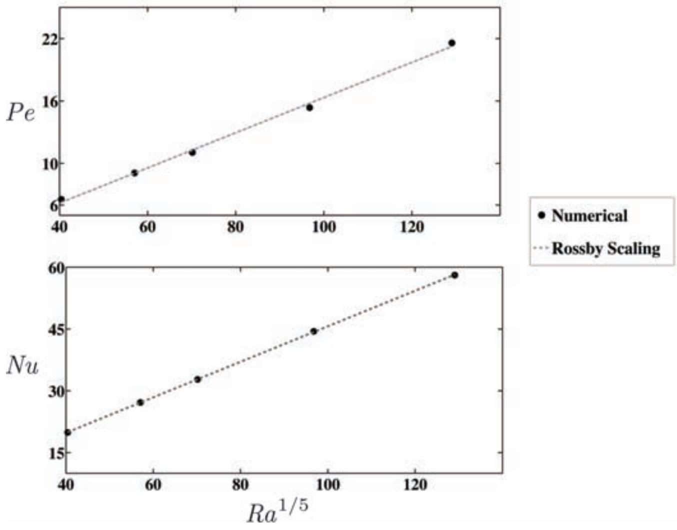

Figure 3.6: Péclet number (top) and Nusselt number (bot) versus $Ra^{1/5}$. Q varies between 0 in the buoyancy stabilizing (hot) end to 2 in the buoyancy destabilizing (cold) end (simulations 3–7).

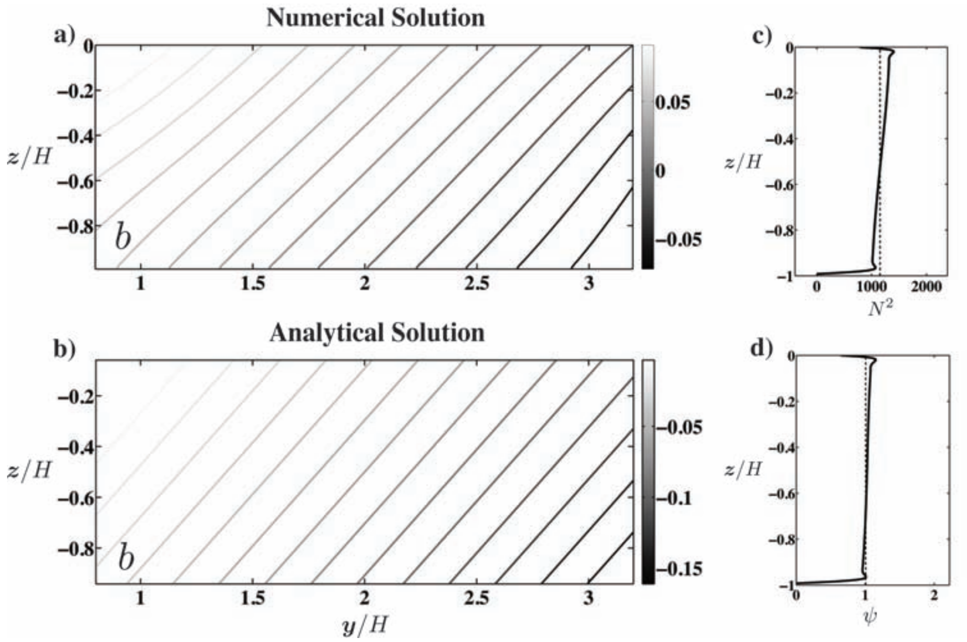

Figure 3.7: Interior, $\boldsymbol{x}$-averaged, steady-state buoyancy normalized by HB_{max}/κ for $\boldsymbol{x}$-uniform RHC simulation (a) and the corresponding analytical field (3.23) (b). Horizontally-averaged interior stratification normalized by $(B_{max}/L_y^2)^{2/3}$ (c) and streamfunction normalized by κ (d) for the numerical solution in (a). Dashed lines in (c) and (d) represent the predicted analytical values $\partial\tilde{b}_I/\partial z$ and $\tilde{\psi}_I$ in (3.23), respectively. Numerical fields are computed from simulation 11 ($Q = 24$).

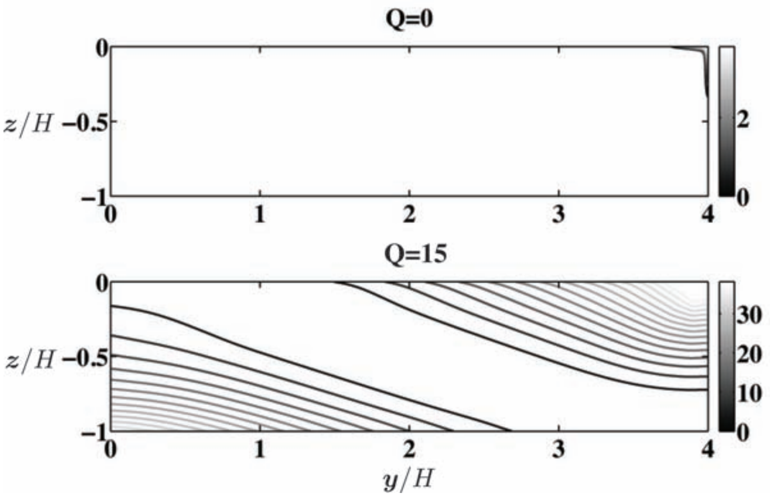

Figure 3.8: Available potential energy density $\mathcal{E}_a$ normalized by $(B_{max}L_y)^{2/3}$, for non-rotating HC (top), and $\boldsymbol{x}$-uniform RHC (bot) from simulations 2 and 10.

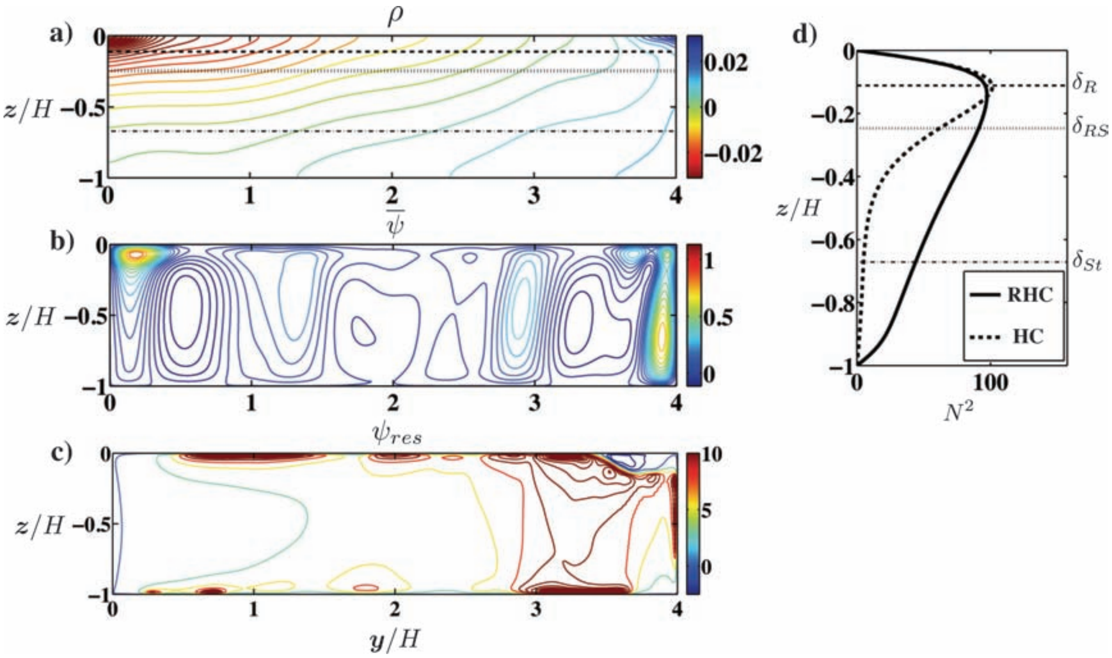

Figure 3.9: Statistically-steady, $\boldsymbol{x}$-averaged density normalized by $HB_{max}\rho_0/g\kappa$ (a), $\boldsymbol{x}$-averaged streamfunction normalized by κ (b), the residual streamfunction $\overline{\psi} + \psi^*$ normalized by κ (c), and horizontally averaged, interior stratification normalized by $(B_{max}/L_y^2)^{2/3}$ (d) for baroclinically-active RHC (simulation 13, $Q = 10$). The dashed line in (d) shows the horizontally averaged stratification for non-rotating HC. Horizontally-dashed, vertically-dashed, and dot-dashed lines in (a) and (d) represent the boundary layer scaling laws proposed by Rossby, (3.8), Robinson & Stommel (3.11) and Stern (3.12), respectively.

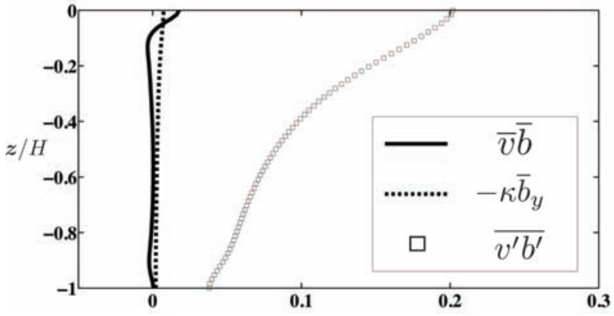

Figure 3.10: Lateral, $\boldsymbol{x}$-averaged, advective (solid), diffusive (dash) and eddy (square) buoyancy flux at $y = L_y/2$, for simulation 13 ($Q = 10$). Fluxes are normalized by B_{max}.

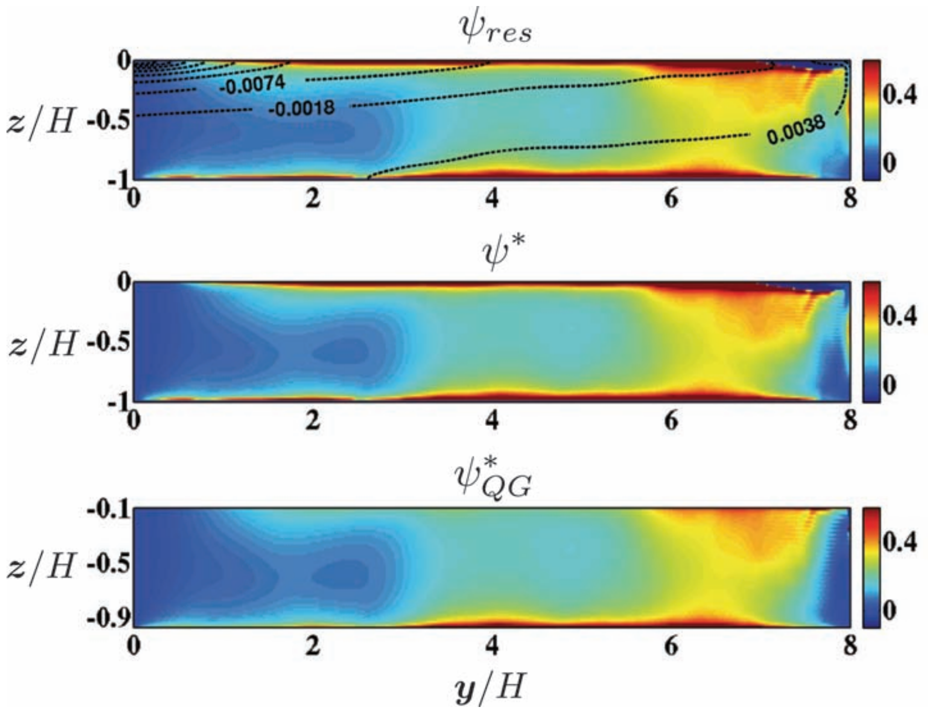

Figure 3.11: The residual streamfunction $\overline{\psi} + \psi^*$ (top), the eddy streamfunction ψ^* (3.34) (middle) and the quasi geostrophic (QG) streamfunction ψ^*_{QG} (3.35) (bottom). Density contours in the top panel are normalized by $HB_{max}\rho_0/g\kappa$. Streamfunctions are normalized by κ. Simulation 15 ($Q = 6$).

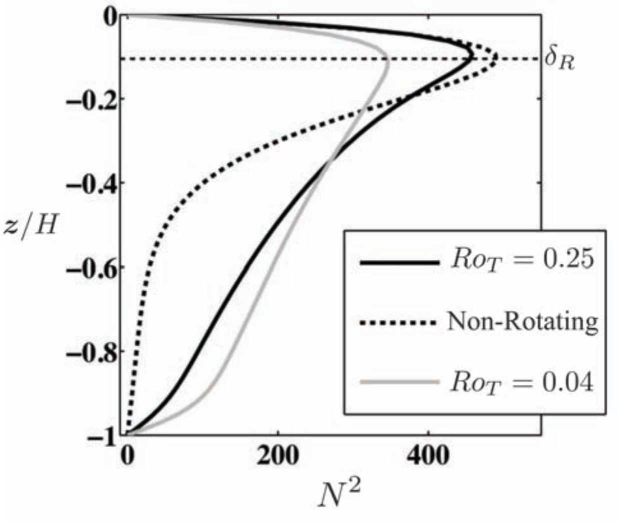

Figure 3.12: The horizontally averaged stratification normalized by $(B_{max}/L_y^2)^{2/3}$ for simulations 14, 15, 16 ($Q = 15, 6, 0$ respectively). The horizontally dashed line represents Rossby's boundary layer scale (3.8) based on simulation 15 ($Ra_B = 2 \times 10^{11}$).

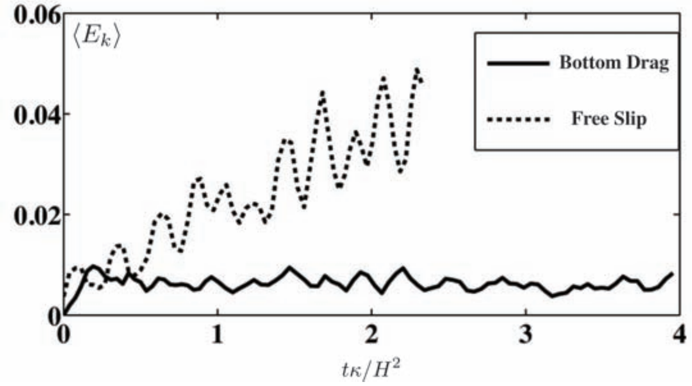

Figure 3.13: Volume-averaged Kinetic Energy (4.8a) normalized by $(B_{max}L_y)^{2/3}$ for baroclinically-active RHC simulations with (solid) and without (dash) bottom drag from simulations 12 and 13 ($Q = 10$).

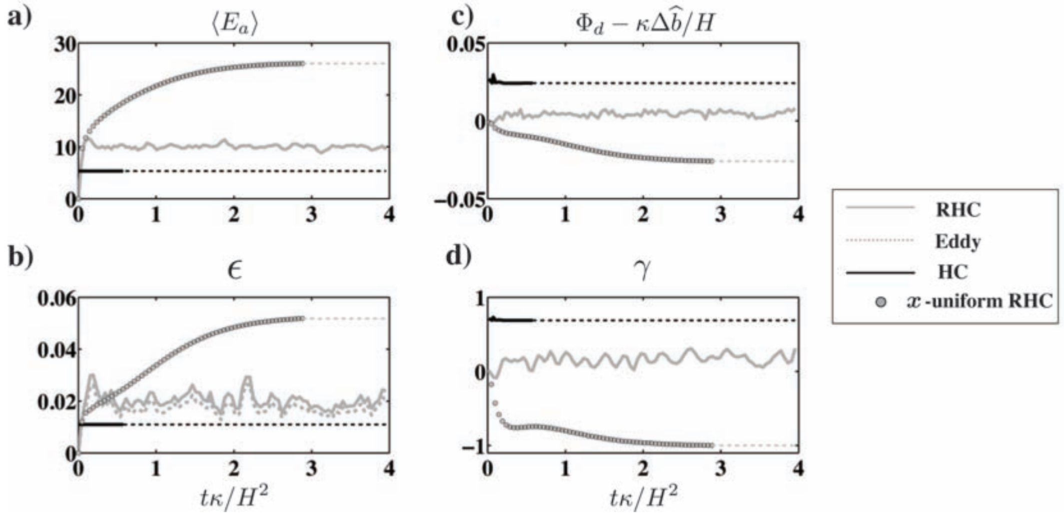

Figure 3.14: Volume-averaged available potential energy (3.4d) normalized by $(B_{max}L_y)^{2/3}$ (a), volume averaged kinetic energy dissipation ϵ normalized by B_{max} (b), $\Phi_d - \frac{\kappa}{H}\Delta\widehat{b}$ normalized by B_{max} (c), and the rate of dissipation of E_a to that of $E_a + E_b$, γ (3.41) (d), for non-rotating HC (black), $\boldsymbol{x}$-uniform RHC (gray circles) and baroclinically-active RHC (gray). Horizontal dashed light gray and black lines are hypothesized extrapolations after equilibrium. Dashed gray line in (c) represents perturbations from $\boldsymbol{x}$ average (eddies). a) Simulations $1, 9$ and 13.

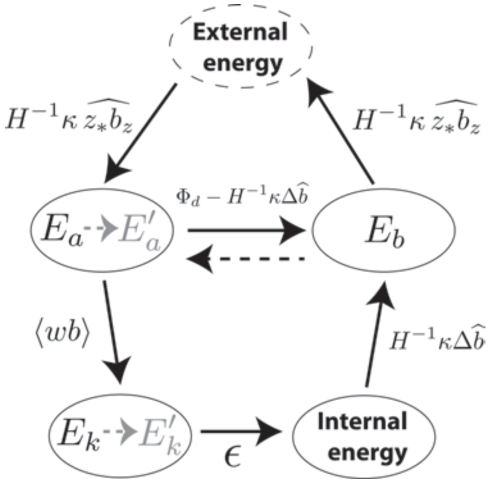

Figure 3.15: Energy cycle between mechanical, external and internal energies for statistically steady horizontal convection (adopted from *Winters & Young* 2009). The dashed black arrow indicates the sign reversal in $\Phi_d - H^{-1}\kappa\Delta\widehat{b}$ for $\boldsymbol{x}$-uniform RHC. The dashed gray arrows indicate that the kinetic and available potential energy reservoirs for baroclinically-active RHC comprise mainly of eddy kinetic and available potential energies.

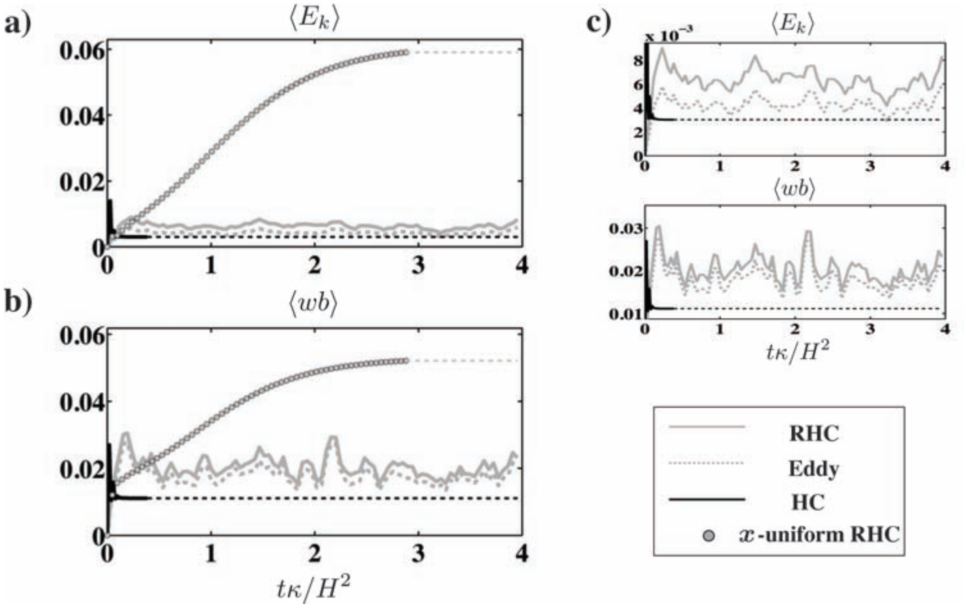

Figure 3.16: Volume averaged kinetic energy (4.8a) normalized by $(B_{max}L_y)^{2/3}$ (a) and vertical buoyancy flux $\langle wb \rangle$ normalized by B_{max} (b), for non-rotating HC (black), $\boldsymbol{x}$-uniform RHC (gray circles) and baroclinically-active RHC (gray). Horizontal dashed light gray and black lines are hypothesized extrapolations after equilibrium. Dashed gray lines represent perturbations from $\boldsymbol{x}$ average (eddies). (*c*) compares between non-rotating HC and baroclinically-active RHC only. Simulations $1\,(Q=0), 9\,(Q=10)$ and $13\,(Q=10)$.

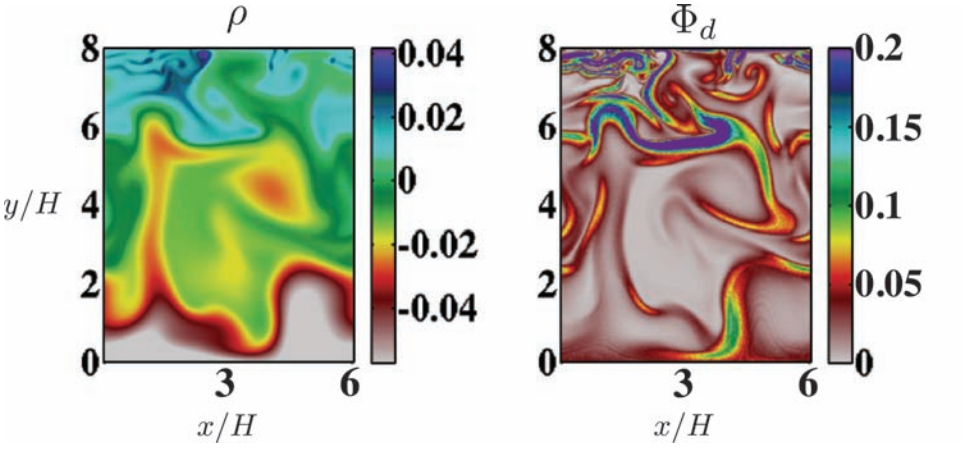

Figure 3.17: Snapshots of horizontal slices of density normalized by $HB_{max}\rho_0/g\kappa$ (left) and diapycnal mixing (Φ_d) normalized by B_{max} (right) at $z/H \sim -0.1$. Simulation 14 $(Q=15)$.

Table 3.1: $L_y = 1.25 \times L_x$, $\alpha = 1/4$ (except for simulations $14 - 16$), $Pr = 7$, Q is defined in (3.10). All simulations were integrated for at least half of a diffusive time (H^2/κ).

Simulation #	Ra_B	Q	$nz \times ny \times nx$	Comments
1	3.8×10^9	0	$65 \times 257 \times 50$	non-rotating HC
2	6.3×10^{10}	0	$257 \times 801 \times 1$	non-rotating HC
3	1.1×10^8	0–2	$129 \times 257 \times 1$	x-uniform RHC, varying Q
4	6.0×10^8	0–2	$193 \times 401 \times 1$	x-uniform RHC, varying Q
5	1.7×10^9	0–2	$257 \times 513 \times 1$	x-uniform RHC, varying Q
6	1.0×10^{10}	0–2	$289 \times 801 \times 1$	x-uniform RHC, varying Q
7	5.4×10^{10}	0–2	$385 \times 1201 \times 1$	x-uniform RHC, varying Q
8	6.3×10^{10}	1	$257 \times 801 \times 1$	x-uniform RHC
9	3.8×10^9	10	$65 \times 257 \times 1$	x-uniform RHC
10	6.3×10^{10}	15	$257 \times 801 \times 1$	x-uniform RHC
11	1.3×10^{12}	24	$257 \times 1025 \times 1$	x-uniform RHC
12	3.8×10^9	10	$65 \times 257 \times 150$	baroclinically-active RHC, free slip
13	3.8×10^9	10	$65 \times 257 \times 150$	baroclinically-active RHC, bot-drag
14	6.0×10^{10}	15	$65 \times 513 \times 300$	$\alpha = 1/8$, $Ro_T = 0.04$, bot-drag
15	2.0×10^{11}	6	$65 \times 513 \times 300$	$\alpha = 1/8$, $Ro_T = 0.24$, bot-drag
16	2.0×10^{11}	0	$65 \times 801 \times 1$	$\alpha = 1/8$, $Ro_T \to \infty$

3.10 Appendix: Details of analytical solution described in § 3.5.1

The solution to (3.17) subject to no-slip boundary condition is:

$$\tilde{\psi} = \frac{d^2\Gamma}{2f} + d\Gamma\left[P1(z) + P2(z) + P3(z) + P4(z)\right], \tag{3.45}$$

where:

$$\begin{aligned}
P1(z) &= \frac{d\cosh\left(\frac{H}{d}\right)\cosh\left(\frac{z}{d}\right)\left(\sec\left(\frac{H}{d}\right)\cos\left(\frac{z}{d}\right) - \coth\left(\frac{H}{d}\right)\sin\left(\frac{H+z}{d}\right)\right)}{2f\left(\sec\left(\frac{H}{d}\right)\cosh\left(\frac{H}{d}\right) - \sin\left(\frac{H}{d}\right)\operatorname{csch}\left(\frac{H}{d}\right)\right)},\\
P2(z) &= \frac{d\sec\left(\frac{H}{d}\right)\cosh\left(\frac{H}{d}\right)\coth\left(\frac{H}{d}\right)\cos\left(\frac{z}{d}\right)\sinh\left(\frac{z}{d}\right)}{2f\left(\sec\left(\frac{H}{d}\right)\cosh\left(\frac{H}{d}\right) - \sin\left(\frac{H}{d}\right)\operatorname{csch}\left(\frac{H}{d}\right)\right)},\\
P3(z) &= -\frac{d\cos\left(\frac{z}{d}\right)\sinh\left(\frac{z}{d}\right)\left(\tan\left(\frac{H}{d}\right) + \coth\left(\frac{H}{d}\right)\right)}{2f\left(\sec\left(\frac{H}{d}\right)\cosh\left(\frac{H}{d}\right) - \sin\left(\frac{H}{d}\right)\operatorname{csch}\left(\frac{H}{d}\right)\right)},\\
P4(z) &= \frac{d\cosh\left(\frac{z}{d}\right)\left(-\tan\left(\frac{H}{d}\right)\sin\left(\frac{z}{d}\right) + \sinh\left(\frac{H}{d}\right)\sin\left(\frac{H+z}{d}\right) + \coth\left(\frac{H}{d}\right)\sin\left(\frac{z}{d}\right)\right)}{2f\left(\sec\left(\frac{H}{d}\right)\cosh\left(\frac{H}{d}\right) - \sin\left(\frac{H}{d}\right)\operatorname{csch}\left(\frac{H}{d}\right)\right)}.
\end{aligned}$$

The corresponding lateral velocity $\tilde{v}$ is:

$$\tilde{v} = \Gamma\left[V1(z) + V2(z) + V3(z) + V4(z)\right], \tag{3.46}$$

where:

$$\begin{aligned}
V1(z) &= \frac{d\sinh\left(\frac{z}{d}\right)\left(\sinh\left(\frac{H}{d}\right)\sin\left(\frac{H+z}{d}\right) + 2\coth\left(\frac{H}{d}\right)\sin\left(\frac{z}{d}\right)\right)}{2f\left(\sec\left(\frac{H}{d}\right)\cosh\left(\frac{H}{d}\right) - \sin\left(\frac{H}{d}\right)\operatorname{csch}\left(\frac{H}{d}\right)\right)},\\
V2(z) &= \frac{d\cosh\left(\frac{z}{d}\right)\left(\sinh\left(\frac{H}{d}\right)\cos\left(\frac{H+z}{d}\right) - 2\tan\left(\frac{H}{d}\right)\cos\left(\frac{z}{d}\right)\right)}{2f\left(\sec\left(\frac{H}{d}\right)\cosh\left(\frac{H}{d}\right) - \sin\left(\frac{H}{d}\right)\operatorname{csch}\left(\frac{H}{d}\right)\right)},\\
V3(z) &= -\frac{d\cosh\left(\frac{H}{d}\right)\sinh\left(\frac{z}{d}\right)\left(\coth\left(\frac{H}{d}\right)\left(\sin\left(\frac{H+z}{d}\right) + \sec\left(\frac{H}{d}\right)\sin\left(\frac{z}{d}\right)\right) - \sec\left(\frac{H}{d}\right)\cos\left(\frac{z}{d}\right)\right)}{2f\left(\sec\left(\frac{H}{d}\right)\cosh\left(\frac{H}{d}\right) - \sin\left(\frac{H}{d}\right)\operatorname{csch}\left(\frac{H}{d}\right)\right)},\\
V4(z) &= -\frac{d\cosh\left(\frac{H}{d}\right)\cosh\left(\frac{z}{d}\right)\left(\sec\left(\frac{H}{d}\right)\sin\left(\frac{z}{d}\right) - \tan\left(\frac{H}{d}\right)\coth\left(\frac{H}{d}\right)\sin\left(\frac{H+z}{d}\right)\right)}{2f\left(\sec\left(\frac{H}{d}\right)\cosh\left(\frac{H}{d}\right) - \sin\left(\frac{H}{d}\right)\operatorname{csch}\left(\frac{H}{d}\right)\right)}.
\end{aligned}$$

The corresponding transverse velocity $\tilde{u}$ is:

$$\tilde{u}(z) = \frac{\Gamma}{f}(z + p_y^0) + \Gamma\left[U1(z) + U2(z) + U3(z) + U4(z)\right], \tag{3.47}$$

where

$$\begin{aligned}
U1(z) &= -\frac{d\cosh\left(\frac{z}{d}\right)\left(\operatorname{csch}\left(\frac{H}{d}\right)\cos\left(\frac{H+z}{d}\right)+\coth\left(\frac{H}{d}\right)\cos\left(\frac{z}{d}\right)\left(\sec\left(\frac{H}{d}\right)\cosh\left(\frac{H}{d}\right)-2\right)\right)}{2f\left(\sec\left(\frac{H}{d}\right)\cosh\left(\frac{H}{d}\right)-\sin\left(\frac{H}{d}\right)\operatorname{csch}\left(\frac{H}{d}\right)\right)},\\
U2(z) &= -\frac{d\sec\left(\frac{H}{d}\right)\cosh\left(\frac{H}{d}\right)\sin\left(\frac{z}{d}\right)\cosh\left(\frac{z}{d}\right)}{2f\left(\sec\left(\frac{H}{d}\right)\cosh\left(\frac{H}{d}\right)-\sin\left(\frac{H}{d}\right)\operatorname{csch}\left(\frac{H}{d}\right)\right)},\\
U3(z) &= \frac{d\sinh\left(\frac{z}{d}\right)\left(2\tan\left(\frac{H}{d}\right)\sin\left(\frac{z}{d}\right)-\sinh\left(\frac{H}{d}\right)\sin\left(\frac{H+z}{d}\right)\right)}{2f\left(\sec\left(\frac{H}{d}\right)\cosh\left(\frac{H}{d}\right)-\sin\left(\frac{H}{d}\right)\operatorname{csch}\left(\frac{H}{d}\right)\right)},\\
U4(z) &= \frac{d\cosh\left(\frac{H}{d}\right)\sinh\left(\frac{z}{d}\right)\left(\tan\left(\frac{H}{d}\right)\coth\left(\frac{H}{d}\right)\cos\left(\frac{H+z}{d}\right)-\sec\left(\frac{H}{d}\right)\cos\left(\frac{z}{d}\right)\right)}{2f\left(\sec\left(\frac{H}{d}\right)\cosh\left(\frac{H}{d}\right)-\sin\left(\frac{H}{d}\right)\operatorname{csch}\left(\frac{H}{d}\right)\right)},\\
p_y^0 &= \left(\frac{d\left(\cos\left(\frac{2H}{d}\right)+\cosh\left(\frac{2H}{d}\right)-2\cos\left(\frac{H}{d}\right)\cosh\left(\frac{H}{d}\right)\right)}{\sin\left(\frac{2H}{d}\right)-\sinh\left(\frac{2H}{d}\right)}+H\right).
\end{aligned}$$

and finally the corresponding buoyancy field $\tilde{b}$ is:

$$\tilde{b}(z)=\frac{\Gamma\nu}{\kappa f}\left(\tilde{u}(z)-\frac{\Gamma}{f}p_y^0\right). \tag{3.48}$$

Note that z has not been transformed as in the free-slip case, and is in the interval $[-H,0]$. (3.19) still holds, leading to:

$$\Gamma^3\mathcal{H}_{ns_1}+\Gamma\kappa H=|\mathcal{F}_{1/2}|, \tag{3.49}$$

where $\mathcal{H}_{ns}=H_{ns_1}+H_{ns_2}+H_{ns_3}+H_{ns_4}>0$ and

$$\begin{aligned}
H_{ns_1} &= \frac{d^4\left(15d\sin\left(\frac{4H}{d}\right)-8H\cos\left(\frac{4H}{d}\right)+8H\sin\left(\frac{3H}{d}\right)\sinh\left(\frac{H}{d}\right)+2\cos\left(\frac{2H}{d}\right)\left(4H-15d\sinh\left(\frac{2H}{d}\right)\right)\right)}{64f^2\kappa\left(\sin\left(\frac{2H}{d}\right)-\sinh\left(\frac{2H}{d}\right)\right)^2},\\
H_{ns_2} &= \frac{d^4\left(16H\cos\left(\frac{H}{d}\right)\cosh\left(\frac{H}{d}\right)\cosh\left(\frac{2H}{d}\right)+2\sin\left(\frac{2H}{d}\right)\left(5d\left(3\cosh\left(\frac{2H}{d}\right)+2\right)-28H\sinh\left(\frac{2H}{d}\right)\right)\right)}{64f^2\kappa\left(\sin\left(\frac{2H}{d}\right)-\sinh\left(\frac{2H}{d}\right)\right)^2},\\
H_{ns_3} &= \frac{d^4\cosh\left(\frac{H}{d}\right)\left(-35d\sinh\left(\frac{H}{d}\right)-8\cos\left(\frac{H}{d}\right)\left(5d\sin\left(\frac{2H}{d}\right)+H\cos\left(\frac{2H}{d}\right)-5d\sinh\left(\frac{2H}{d}\right)\right)\right)}{32f^2\kappa\left(\sin\left(\frac{2H}{d}\right)-\sinh\left(\frac{2H}{d}\right)\right)^2},\\
H_{ns_4} &= \frac{d^4\left(8H\sin\left(\frac{H}{d}\right)\left(2\sinh\left(\frac{H}{d}\right)+\sinh\left(\frac{3H}{d}\right)\right)+2\sinh\left(\frac{H}{d}\right)\left(8H\sinh\left(\frac{3H}{d}\right)-15d\cosh\left(\frac{3H}{d}\right)\right)\right)}{64f^2\kappa\left(\sin\left(\frac{2H}{d}\right)-\sinh\left(\frac{2H}{d}\right)\right)^2}.
\end{aligned}$$

For for free-slip bottom boundary condition the solution is (3.18), where,

$$\begin{aligned}
F_1(z') &= \sin\left(\frac{z'}{d}\right)\cosh\left(\frac{z'}{d}\right), \\
F_2(z') &= \cos\left(\frac{z'}{d}\right)\sinh\left(\frac{z'}{d}\right), \\
G_1 &= \frac{d\left(\sin\left(\frac{H}{2d}\right)\sinh\left(\frac{H}{2d}\right)-\cos\left(\frac{H}{2d}\right)\cosh\left(\frac{H}{2d}\right)\right)}{f\left(\cos\left(\frac{H}{d}\right)+\cosh\left(\frac{H}{d}\right)\right)}, \\
G_2 &= \frac{d\left(\sin\left(\frac{H}{2d}\right)\sinh\left(\frac{H}{2d}\right)+\cos\left(\frac{H}{2d}\right)\cosh\left(\frac{H}{2d}\right)\right)}{f\left(\cos\left(\frac{H}{d}\right)+\cosh\left(\frac{H}{d}\right)\right)}.
\end{aligned} \tag{3.50}$$

In (3.20), $\mathcal{H}_{fs} = H_{fs_1} + H_{fs_2} + H_{fs_3} > 0$, where

$$\begin{aligned}
H_{fs_1} &= \frac{d^4\left(-d\sin\left(\frac{H}{d}\right)+H\cos\left(\frac{H}{d}\right)+H\cosh\left(\frac{H}{d}\right)-d\left(\cos\left(\frac{H}{d}\right)+2\right)\sinh\left(\frac{H}{d}\right)\right)}{4f^2\kappa\left(\cos\left(\frac{H}{d}\right)+\cosh\left(\frac{H}{d}\right)\right)}, \\
H_{fs_2} &= \frac{11d^5\sin\left(\frac{2H}{d}\right)+d^4\left(4\cosh\left(\frac{H}{d}\right)\left(5d\sin\left(\frac{H}{d}\right)+2H\cos\left(\frac{H}{d}\right)\right)+8H\right)}{128f^2\kappa\left(\cos\left(\frac{H}{d}\right)+\cosh\left(\frac{H}{d}\right)\right)^2}, \\
H_{fs_3} &= \frac{d^5\left(20\cos\left(\frac{H}{d}\right)\sinh\left(\frac{H}{d}\right)-\left(\cos\left(\frac{2H}{d}\right)-11\right)\sinh\left(\frac{2H}{d}\right)+\sin\left(\frac{2H}{d}\right)\left(-\cosh\left(\frac{2H}{d}\right)\right)\right)}{128f^2\kappa\left(\cos\left(\frac{H}{d}\right)+\cosh\left(\frac{H}{d}\right)\right)^2}.
\end{aligned} \tag{3.51}$$

Chapter 4

Energy Cascades and Loss of Balance in a Re-entrant Channel Forced by Wind Stress and Buoyancy Fluxes

A large fraction of the kinetic energy in the ocean is stored in the 'quasi-geostrophic' eddy field. This 'balanced' eddy field is expected, according to geostrophic turbulence theory, to transfer energy to larger scales. In order for the general circulation to remain approximately steady, instability mechanisms leading to 'loss of balance' (LOB) have been hypothesized to take place so that the eddy kinetic energy (EKE) may be transferred to small scales where it can be dissipated. We examine the kinetic energy pathways in fully resolved direct numerical simulations of flow in a flat-bottomed re-entrant channel, externally forced by surface buoyancy fluxes and wind stress, in a configuration that resembles the Antarctic Circumpolar Current. The flow is allowed to reach a statistical steady state at which point it exhibits both a forward and an inverse energy cascade. Flow interactions with irregular bathymetry are excluded so that bottom drag is the sole mechanism available to dissipate the upscale EKE transfer. We show that EKE is dissipated preferentially at small scales near the surface via frontal instabilities associated with LOB and a forward energy cascade rather than by bottom drag after an inverse energy cascade. This is true both with and without forcing by the wind. These results suggest that LOB caused by frontal instabilities near the ocean surface could provide an efficient mechanism, independent of boundary effects, by which EKE is dissipated. Ageostrophic anticyclonic instability is the dominant frontal instability mechanism in our simulations. Symmetric instability is also important in a 'deep convection' region, where it can be sustained by buoyancy loss.

4.1 Introduction and Motivation

The general circulation of the ocean is forced by surface fluxes of momentum, heat, and fresh water at basin scales. A large fraction of the kinetic energy (E_k) associated with the large scale forcing must be dissipated at molecular scales in order for the circulation to remain approximately steady. The E_k pathways across this wide range of scales remain poorly understood (*Ferrari and Wunsch*, 2009). Possible routes to dissipation include non-linear internal wave interactions in the interior, instability of geostrophic motions, and direct interactions with side and bottom boundaries (*Müller et al.*, 2005; *Ferrari and Wunsch*, 2010). About 90% of the E_k in the oceans is stored in the geostrophic eddy field (*Ferrari and Wunsch*, 2009) and, given this large fraction, we focus here on the 'instability' pathway to dissipation.

Geostrophic eddies are formed, primarily, via baroclinc instability of large-scale ocean currents that are in approximate thermal wind balance (*Gill et al.*, 1974). These geostrophic currents and eddies are considered 'balanced' in the sense that they are in geostrophic and hydrostatic balance and the associated velocity and buoyancy fields are entirely determined by the potential vorticity (*Ford*, 1993). The quasi - two dimensional geostrophic-eddy field is expected, based on geostrophic turbulence theory, to transfer energy to larger scales (*Salmon*, 1980). Kinetic energy dissipation, however, is observed to take place at small scales (*Wunsch and Ferrari* 2004 and references therein). Instability mechanisms leading to a ‘loss of balance’ are therefore hypothesized to take place in order that some of the kinetic energy of the geostrophic eddies (EKE) may be transferred to small scales where it can be dissipated.

Recent numerical studies (*Capet et al.*, 2008c; *Molemaker et al.*, 2010) have suggested that ‘loss of balance’ due to sub-mesoscale instabilities can provide an efficient route to small-scale dissipation. To explore this hypothesis, we pose an idealized problem of flow in a flat-bottomed re-entrant channel, externally forced by surface buoyancy fluxes and wind stress, in a configuration that resembles the Antarctic Circumpolar Channel (ACC). The flow is allowed to reach a statistical steady state at which point it exhibits both forward and inverse energy cascades. Flow interactions with irregular bathymetry are excluded so that bottom drag is the sole mechanism available to dissipate the upscale energy cascade. This simple setting allows us to compare the E_k energy pathways along two main routes; the ‘inverse’ route - in which EKE is transferred to larger scales where it is dissipated via bottom drag; and the ‘forward’ route - in which EKE cascades to small dissipative scales, presumably via ‘loss of balance’. We analyze these competing routes to dissipation for two different forcing scenarios and evaluate the relative efficiency of each pathway.

Capturing both the inverse and forward pathways while computing kinetic energy dissipation accurately requires a wide range of scales to be resolved and is a challenging numerical task. We are therefore forced to make compromises in the problem setup. We evaluate the validity of our numerical simulations in representing realistic oceanic flows based on five non-dimensional parameters (see §4.2 for details) and find them to be in quantitative agreement with the oceanic dynamical regime. In addition, we diagnose the mean buoyancy structure and the mean and eddy driven circulations and find them to be in qualitative agreement with zonal-mean theories of the ACC (see §4.3 for details). This suggests that understanding the physical mechanisms illuminated by this process study is helpful in improving our dynamical understanding of real ocean phenomena.

This chapter is organized as follows: in §4.2 we discuss the problem setup; in §4.3 we describe the overall flow features; in §4.4 we show the E_k balance; in

§4.5 we provide spectral analyses of velocity variance, E_k equation, and E_k fluxes; in §4.6 we evaluate 'loss of balance' in relation to EKE dissipation; finally, in §4.7 we provide a summary and discussion.

4.2 Problem setup

We consider an idealized ocean basin on an f plane in a rectangular channel of volume V uniform depth H, with zonal and meridional dimensions $L_x = L_y$. The vertical coordinate is $-H \leq z \leq 0$, and density is expressed as $\rho = \rho_0(1 - g^{-1}b)$, where b is the buoyancy. The corresponding Cartesian, Boussinesq equations are:

$$\frac{D\boldsymbol{u}}{Dt} + f\hat{\boldsymbol{k}} \times \boldsymbol{u} = -\nabla p + b\hat{\boldsymbol{k}} + \nu\boldsymbol{\nabla}^2\boldsymbol{u} - rf_{bot}(z)(u\hat{\boldsymbol{\imath}} + v\hat{\boldsymbol{\jmath}}), \tag{4.1a}$$

$$\frac{Db}{Dt} = \kappa\nabla^2 b, \tag{4.1b}$$

$$\boldsymbol{\nabla} \cdot \boldsymbol{u} = 0. \tag{4.1c}$$

The pressure is $\rho_0 p$, $f > 0$ is the Coriolis frequency, κ is the diffusivity, ν is the kinematic viscosity, r [s^{-1}] is the coefficient of bottom drag, $f_{bot}(z)$ is a near-bottom localization function discussed in the appendix, and $\hat{\boldsymbol{\imath}}, \hat{\boldsymbol{\jmath}}, \hat{\boldsymbol{k}}$ are the unit vectors in the zonal (x), meridional (y), and vertical (z) directions. No-penetration conditions $\boldsymbol{u}\cdot\hat{\boldsymbol{n}} = 0$, are imposed on the top, bottom and meridional sides, where $\boldsymbol{u} = (u, v, w)$ and $\hat{\boldsymbol{n}}$ is the outward normal to the surface of V. The flow is taken to be periodic in the zonal direction. Free-slip and no scalar flux conditions are prescribed on the bottom and meridional sides.

Our analysis is based on two direct numerical simulations (DNS) in the configuration described above. The first simulation, hereafter referred to as 'Buoyancy Forced' (BF), is forced at the surface solely by a buoyancy flux of the form

$$\kappa\frac{\partial b}{\partial z}|_{z=0} = B_{max}\mathcal{F}_b(y) = B_{max}\left(\mathrm{e}^{-(y/(\lambda_y))^2} - \mathrm{e}^{-([y-L_y]/(\lambda_y))^2}\right), \tag{4.2}$$

where B_{max} [m^{2}s^{-3}] is the magnitude of the maximal buoyancy flux applied at the surface and $\lambda_y = L_y/8$; (4.2) corresponds to supplying positive buoyancy anomalies near $y = 0$ and negative buoyancy anomalies near $y = L_y$, as is shown in figure 4.2.

The second simulation, hereafter referred to as ‘Wind and Buoyancy Forced’ (WBF), is forced by the same buoyancy flux but, in addition, a surface stress

$$\rho_0 \tau \hat{\boldsymbol{i}} = \mu \frac{\partial u}{\partial z}|_{z=0} = \rho_0 \tau_{max} \mathcal{F}_\tau(y) = \rho_0 \tau_{max} \sin(\pi y / L_y) \hat{\boldsymbol{i}} \equiv \rho_0 \tau_s \qquad (4.3)$$

is applied at the top, where μ is the dynamic viscosity and $\rho_0 \tau_{max}$ [N m^{-2}] is the magnitude of the maximal surface stress. The Ekman pumping $-f^{-1}\partial\tau/\partial y$ associated with (4.3) correspond to downwelling positively buoyant fluid near $y = 0$ and upwelling negatively buoyant fluid near $y = L_y$ (see figure 4.2). This configuration resembles the ACC in the sense that the wind stress curl acts to increase available potential energy and is therefore ‘eddy-favoring’ (*Cessi*, 2007).

Both simulations were run for ~ 0.25 of a diffusive time (H^2/κ) by which Eq. (4.8a) has reached a statistical steady state (figure 4.5). Time averages and all analyses presented in this paper are based on the last 0.05 diffusive time, during which all physical variables were stored every 6.5 inertial periods (f^{-1}) for a total of 58 snapshots. Throughout the manuscript we present probability distribution functions (PDFs) and cumulative distribution functions (CDFs) of various diagnostic parameters computed for mean and total quantities at selected regions of the domain. The PDFs and CDFs are computed using all grid points in the specified domain for all snapshots. For example, if a PDF is computed based on the entire volume V than the total number of samples is $65 \times 1025 \times 1024 \times 58 \sim O(10^9)$. The PDFs in figures 4.1, 4.4 and 4.17 are normalized to lie between zero and one.

The model equations (4.1) for both simulations are solved using the non-hydrostatic three dimensional pseudo-spectral model **flow_solve**. See appendix 4.8 for more details on the model and problem setup.

Throughout the paper $\langle () \rangle$ denotes a volume average, $\widehat{()}$ denotes a spatial average over the horizontal area $A = L_x \times L_y$, $\overline{()}^x$ denotes an average over the zonal length L_x, $\overline{()}^t$ denotes a time average and eddies (denoted by $'$) are defined as perturbations from both time and zonal averages (denoted by $\overline{()}$). Note that at statistical steady state $\overline{()} \approx \overline{()}^x$.

In order to compare our simulations to the ocean we compute, at steady state, the resulting Rossby number Ro, the Ekman number Ek, and the Burger number Bu, defined as

$$Ro = \frac{\overline{\zeta}}{f}, \qquad Ek = \frac{\nu \overline{u}_{zz}}{f \overline{u}}, \qquad Bu = \left(\frac{R_d}{L_y}\right)^2, \tag{4.4}$$

where ζ is the vertical component of vorticity, subscripts denote derivatives and R_d is the Rossby deformation radius. Two additional non-dimensional numbers are required to completely define our problem and we choose the externally determined parameters

$$Pr = \frac{\nu}{\kappa}, \qquad \alpha = \frac{H}{L_y}, \tag{4.5}$$

where Pr is the Prandtl number and α is the aspect ratio.

The non-dimensional numbers (4.4, 4.5) for the WBF simulation presented in this paper are

$$Ro \approx 0.025, \qquad Ek \approx 0.007, \qquad Bu \approx 10^{-2}, \qquad Pr = 7, \qquad \alpha = \frac{1}{15}. \tag{4.6}$$

The value for Ek represents the mean computed in the interior ($0.8 < y/H < 14.2$, $0.06 < z/H < 0.94$) away from the boundaries were frictional effects are expected to be important ($Ek \sim 0.1$ there). 90% of the Ek values are below 0.02. The value for Ro represents the mean computed over the entire domain. 90% of the values are below 0.05. The analyses shown in figures 4.8 and 4.10 help us estimate the ratio R_d/L_y as $O(10^{-1})$ (see §4.5.2 and 4.5.3 for details) and the corresponding Bu as $O(10^{-2})$. Our simulations are thus well within the dynamical regime of the ocean with respect to all of the non-dimensional numbers aside from the aspect ratio which is one to two orders of magnitude larger than that of typical ocean basins.

In order to verify that our simulations are in hydrostatic balance at basin scales as well as mesoscales we follow *Molemaker et al.* (2010) who have suggested a measure to asses the degree of which the solutions are in hydrostatic balance using the parameter

$$\mathcal{E}_{hydro} = \frac{|-\partial_z p + b|}{|\partial_z p| + |b| + \mu}, \tag{4.7}$$

where $\mu = (\partial_z p)_{rms} + b_{rms}$ is added to the denominator of (4.7) to exclude situations with locally weak vertical pressure gradients of being identified as significantly unbalanced. Regions where $\mathcal{E}_{hydro} \approx 0$ are thus considered to be hydrostatically balanced and regions where $\mathcal{E}_{hydro} \approx 1$ are considered highly non-hydrostatic. Figure 4.1 shows the probability density function (PDF) of $\mathcal{E}_{hydro}$ computed over the entire volume. 99% of the values are smaller than $0.015, 0.04$ for BF, WBF respectively indicating that the flow is hydrostatically balanced at all scales. A similar analysis using the time and zonal mean fields $\partial_z \bar{p}, \bar{b}$ (not shown) indicates that 99% of the mean $\mathcal{E}_{hydro}$ values are below $0.005, 0.009$. These results ensure that the flow in our simulations is hydrostatically balanced at nearly all scales of motion. Figures 4.13, 4.14 (panel e) show that hydrostatic balance is partially lost ($\mathcal{E}_{hydro} \sim O(0.1)$) at the sharp, near surface sub-mesoscale fronts that develop at the edges of the mesoscale eddies (see §4.6 and 4.7 for discussion).

The volume averaged kinetic (E_k) and potential (E_p) energy equations for the model (4.1) take the form

$$\frac{d\langle E_k\rangle}{dt} \equiv \frac{1}{V}\frac{d}{dt}\left(\frac{1}{2}\int |\boldsymbol{u}|^2\,\mathrm{d}V\right) = \langle wb\rangle - \epsilon - \epsilon_d + \frac{1}{H}\widehat{\boldsymbol{u}_s\cdot\tau_s}, \tag{4.8a}$$

$$\frac{d\langle E_p\rangle}{dt} \equiv \frac{1}{V}\frac{d}{dt}\left(\int -zb\,\mathrm{d}V\right) = -\langle wb\rangle + \frac{\kappa}{H}\Delta\widehat{b}, \tag{4.8b}$$

where $\epsilon = \nu\langle|\boldsymbol{\nabla}\boldsymbol{u}|^2\rangle$, $\epsilon_d = r\langle|\boldsymbol{u}_{bot}|^2\rangle$, $\Delta\widehat{b} = \widehat{b}(0) - \widehat{b}(-H)$, $\boldsymbol{u}_{bot}$ and $\boldsymbol{u}_s$ are the horizontal velocities (u, v) evaluated at the bottom and surface respectively and, at steady state, $\langle wb\rangle = \langle\bar{w}\bar{b}\rangle + \langle\overline{w'b'}\rangle$ is the reversible conversion term between kinetic and potential energies associated with the mean and the eddies respectively. Similarly the Laplacian EKE dissipation is $\epsilon' = \nu\langle|\boldsymbol{\nabla}\boldsymbol{u}'|^2\rangle$ and EKE dissipation due to bottom drag is $\epsilon'_d = r\langle|\boldsymbol{u}'_{bot}|^2\rangle$. In the following sections we will evaluate the relative efficiency of the 'inverse' to 'forward' routes by comparing the reservoirs of ϵ, ϵ' and ϵ_d, ϵ'_d.

The spectral representation of the E_k equation is derived by taking the co-spectra of the dot product of $\boldsymbol{u}$ and (4.1a) to give

$$\frac{1}{2}\frac{\partial}{\partial t}\{\boldsymbol{u}\}_k\{\boldsymbol{u}\}_k^{\diamond} = \mathcal{R}[-\{\boldsymbol{u}\}_k\{(\boldsymbol{u}\cdot\nabla)\boldsymbol{u}\}_k^{\diamond} + \{w\}_k\{b\}_k^{\diamond} + \{\boldsymbol{u}\}_k\{\mathcal{D}\}_k^{\diamond} + \{\boldsymbol{u}\}_k\{\mathcal{T}\}_k^{\diamond}], \tag{4.9}$$

where $\{\,\}_k$ denotes a Fourier transform, $^{\diamond}$ denotes a complex conjugate, and $\mathcal{R}$ denotes the real part. The terms $\mathcal{D}, \mathcal{T}$ denote the dissipation (both Laplacian and bottom drag) and wind input respectively.

4.3 Overall flow features

Figure 4.2 (left) shows the time averaged buoyancy field for BF. The specified flux boundary condition (4.2) corresponds to buoyancy gain near $y = 0$ and buoyancy loss near $y = L_y$. Figure 4.3 shows the time and zonal-mean isopycnal height (top), Eulerian-mean streamfunction $\overline{\psi}$ (middle), and residual streamfunction ψ_{res} (streamfunction computed in buoyancy space and interpolated back to $\boldsymbol{z}$-space). The residual streamfunction $\psi_{res} \approx \overline{\psi} + \psi^*$ provides a useful framework for understanding buoyancy transport associated with the mean flow ($\overline{\psi}$) and the eddies (ψ^*) *Wolfe* (2014). For BF the solutions consist of a plume (deep convection region) near $y/H = 15$ and a thermocline near $y/H = 0$. The residual streamfunction, ψ_{res}, is much larger than the Eulerian-mean streamfunction $\overline{\psi}$, indicating that buoyancy is mainly transported by the eddies (denoted by wavy arrows in figure 4.2, left). The depth of the thermocline is set by the interaction between the deep convection and the baroclinic eddies (*Barkan et al.*, 2013).

Figure 4.2 (right) shows the time averaged zonal velocity field (u) for WBF. The spatial structure of the zonal jet is shown as well as the Ekman upwelling ($y \approx L_y$) and downwelling ($y \approx 0$) regions associated with the surface wind stress curl (4.3). The thermocline depth in this case is determined by the balance between the wind induced Ekman flow and the baroclinic eddies (*Marshall and Radko*, 2003). Figure 4.3 shows that the thermocline, near $y/H = 0$ is deeper than in BF. Near $y/H = 15$ the interaction between the deep convection, wind induced upwelling and baroclinic eddies sets the isopycnal structure. The Eulerian-mean streamfunction $\overline{\psi}$, associated in WBF with the wind induced Ekman flow (thermally indirect), is much stronger than the viscously driven one in BF. The magnitudes of ψ_{res} and $\overline{\psi}$ are similar for WBF, but the circulation is reversed. This illustrates the eddies' tendency to counteract the Ekman flow and produce a thermally-direct flow. For nearly adiabatic flow in a channel configuration ψ_{res} is expected to decrease as κ decreases (hence the name 'residual'), a well known result from GCM simulations of the ACC (*Marshall and Speer 2012* and references therein). Note that in the thermocline region ($0 \leq y/H \leq 6$) $\psi_{res} \approx 0$ suggesting that the flow is approximately adiabatic there. In order to assess how adiabatic our interior flow is for WBF we examine the departure of the time and zonally averaged buoyancy equation 4.1b from

$$\partial_y(\overline{v\,b}) + \partial_z(\overline{w\,b}) = 0, \tag{4.10}$$

using the parameter

$$\mathcal{E}_{adiab} = \frac{|(\partial_y\overline{v\,b}) + \partial_z(\overline{w\,b})|}{|\partial_y(\overline{v\,b})| + |\partial_z(\overline{w\,b})| + \mu}, \tag{4.11}$$

where $\mu = \partial_y(\overline{v\,b})_{rms} + \partial_z(\overline{w\,b})_{rms}$. Analogously to (4.7), regions where $\mathcal{E}_{adiab} = 0$ are completely adiabatic and regions where $\mathcal{E}_{adiab} = 1$ are completely diabatic. The PDF of the interior $\mathcal{E}_{adiab}$ (e.g. in the domain $0.8 < y/H < 14.2\,, 0.06 < z/H < 0.94$) is plotted in figure 4.4. 90% of the values are below 0.05, indicating that diffusivity is negligible in the interior of our domain in agreement with zonally averaged theories of the ACC. Note that typical stratification values produced in the WBF simulation are lower than in the ACC, $N/f \sim 5$ compared with ~ 25 (*Garabato et al.*, 2004). In reality the thermal structure of the ACC depends on bathymetric detail, lateral exchanges with the basin to the north and the shelf dynamics at the Antarctic margin. None of these processes is included in our model, which are presumably necessary to quantitatively match observations.

4.4 Kinetic energy balance

Figure 4.5 shows the terms in (4.8a) demonstrating that, in both cases, the E_k reservoir has reached a statistical steady state. The ratio $\overline{\mathrm{E}_{\mathrm{k}_{\mathrm{WBF}}}}^t/\overline{\mathrm{E}_{\mathrm{k}_{\mathrm{BF}}}}^t = 7.1$ illustrating that the E_k reservoir is much larger for WBF. The ratio $\overline{\epsilon}^t/\overline{\epsilon_{\mathrm{d}}}^t$ is 1.8 for BF and 0.27 for WBF. Bottom drag thus provides a much larger sink for E_k in WBF.

Figure 4.6 shows the decomposition of $\langle wb\rangle, \epsilon, \epsilon_d$ in (4.8a) into the mean and eddy components. For BF the vertical buoyancy flux is accomplished by the eddies ($\langle\overline{w'b'}\rangle \gg \langle\bar{w}\bar{b}\rangle$) and 80 % of the total E_k is EKE. For WBF $\langle\bar{w}\bar{b}\rangle \approx -\langle\overline{w'b'}\rangle$. The wind generates available E_p (APE) by tilting the isopycnals ($\langle\bar{w}\bar{b}\rangle < 0$) and the eddies release APE via baroclinic instability and restratify the fluid

($\langle \overline{w'b'} \rangle > 0$). Note that both of these terms are equal in magnitude to the total dissipation of EKE ($\epsilon' + \epsilon'_d$) and to the vertical buoyancy flux by the Ekman velocity $w_E = -(2f)^{-1} d\tau_s/dy$. In this simulation most of the wind work is used to form a barotropic jet in the zonal direction (figure 4.2). The energy associated with this jet ($\sim 75\%$ of the total E_k) is dissipated by bottom drag ($\langle \overline{\epsilon}_d \rangle$). Only a small fraction of the wind work ($\langle \overline{w_E} \bar{b} \rangle$), sometimes referred to as 'useful wind work' (*Cessi et al.*, 2006), is expended in generating APE and thus available to drive baroclinic eddies. Accordingly, the ratio $\overline{\mathrm{EKE}_{\mathrm{WBF}}}^t / \overline{\mathrm{EKE}_{\mathrm{BF}}}^t = 2.25$, smaller than for the total fields. This result suggests a way to evaluate the relative importance of wind to surface buoyancy forcing by comparing their role in generating EKE. For BF figure 4.6 and (4.8b) suggest that, at steady state, $\langle wb \rangle \sim \langle \overline{w'b'} \rangle = H^{-1}\kappa\Delta\widehat{b} \leq H^{-1}\kappa b_{\mathrm{max}}$, where b_{max} is the maximal specific buoyancy difference. We therefore propose the non-dimensional number

$$S_{EKE} = \frac{\langle \overline{W_{Ek}}\, \bar{b} \rangle}{H^{-1}\kappa\Delta\widehat{b}} \sim \frac{\tau_{max}\alpha}{f\kappa} \tag{4.12}$$

as a measure for the relative importance of wind to buoyancy forcing in generating EKE in the ocean. For a typical ocean basin with $\alpha = 10^{-3}$, $\kappa = 10^{-5}\, m^2 s^{-1}$, $f = 10^{-4}\, s^{-1}$, and $\tau = 10^{-4}\, m^2 s^{-2}$ (corresponding to a wind stress of $0.1\, Nm^{-2}$) $S_{EKE} \sim 100$, illustrating that buoyancy fluxes provide only 1% of EKE compared with the useful wind work. In the WBF simulation $S_{EKE} \sim 6$, suggesting that our wind forcing is much weaker than that of the ACC (see §4.7 for discussion).

The ratio $\overline{\epsilon'}^t / \overline{\epsilon'_{\mathrm{d}}}^t = 1.6$ for BF and 1.67 for WBF. This is the main result of this paper, demonstrating that both with and without mechanical forcing a large fraction of EKE dissipation is established independent of bottom drag. This suggests that, in both cases, the 'forward route' to dissipation is more effective than the 'inverse route' in removing eddy kinetic energy once the flow has reached a quasi-steady state. It remains to be shown that the Laplacian EKE dissipation (ϵ') is directly linked to a forward energy cascade and loss of balance.

4.5 Spectral analysis

4.5.1 Horizontal velocity wavenumber spectra

Figure 4.7 shows the time averaged horizontal velocity (u, v) wavenumber spectra in the k_x (black) and k_y (gray) directions, computed both near the surface (solid lines) and at depth (dashed line). For both BF and WBF the surface spectral shapes are nearly flat at low wavenumbers, exhibit a rolloff and become linear over more than a decade of wavenumbers, and then steepen further at higher wavenumber where horizontal isotropy is lost and the flow becomes more three-dimensional (the horizontally isotropic regions are gray shaded). The spectral shapes at depth closely resemble those at the surface, although the spectral level is reduced by about a decade over the entire wavenumber range (in WBF the amount of energy at the lowest meridional wavenumber is independent of depth, a signature of the barotropic zonal jet).

For BF the spectral slope after the rolloff is close to k^{-3} whereas in WBF it is closer to k^{-2}. A k^{-3} spectral slope is typically associated with an enstrophy inertial subrange in quasi-geostrophic turbulence theory (*Salmon*, 1980). A k^{-2} spectral slope has previously been observed in submesoscale resolving simulations (*Capet et al.*, 2008a, figure 6) and was interpreted as an indication of a significant amount of kinetic energy in the submesoscale range. This suggests that the energy reservoir in the wavenumber band associated with submesoscale features is larger for WBF.

4.5.2 Kinetic energy spectral balance

Figure 4.8 shows the individual terms in the spectral energy balance (4.9). The co-spectra are vertically integrated, time averaged and are computed as a function of the horizontal wavenumber $k_h = \sqrt{k_x^2 + k_y^2}$. Solid lines denote total fields and dashed lines denote eddy fields.

For BF there is very little difference between total and eddy fields. Positive $\{w\}_k\{b\}_k^\diamond$ (blue line) illustrates the release of APE by baroclinic instability. The peak around $k_h L_y \sim 5$ corresponds to the most unstable baroclinic mode, k_{bc} (vertical dashed lines on the right panels), and can be used to approximate the effective Rossby radius of deformation wavenumber k_d. Note that, in effect, k_d is probably a few times larger than k_{bc} (for the classical *Eady* (1947) baroclinic instability analysis $k_d \approx 3.9 k_{bc}$). The green line is the momentum advection term $(+\{\boldsymbol{u}\}_k \{(\boldsymbol{u} \cdot \nabla)\boldsymbol{u}\}_k^\diamond)$ which, by definition, is identically zero when integrated over the entire wavenumber range. It thus only describes a redistribution of energy across wavenumbers. Note that the transition between negative and positive energy flux divergence occurs around k_{bc}. The Laplacian EKE dissipation term (black line) and the EKE dissipation due to bottom drag (red line) extract roughly the same amount of energy for $k_h L_y < 7$. However for higher wavenumbers Laplacian EKE dissipation exceeds bottom drag EKE dissipation.

In contrast, for WBF there is a clear difference between total and eddy fields at low wavenumbers ($k_h L_y < 2.5$), where most of the energy is in the mean flow. Wind work (magenta line) supplies energy at large scales, primarily to the barotropic zonal jet (figure 4.2) whose energy is dissipated by bottom drag (red line). Negative values of $\{w\}_k \{b\}_k^\diamond$ (blue line) indicate the generation of APE by the wind, corresponding to negative $\langle \bar{w}\bar{b} \rangle$ values in figure (4.6). For $k_h L_y > 2.5$ the energy is mainly in the eddy field and the picture resembles qualitatively that of BF. Quantitatively, the reservoir of E_k is larger (note the different y-axis range between top and bottom panels), and k_{bc} is slightly larger as well. Assuming $k_d \approx 2k_{bc}$, which is less than the 3.9 value in the classical *Eady* (1947) problem, results in $k_d L_y \approx 10$. This means that our domain contains roughly 10 Rossby radii of deformation, leading to our estimate of the Bu in (4.4) as being $O(10^{-2})$. Bottom drag EKE dissipation exceeds Laplacian dissipation in the range $k_h L_y < 10$. However as in BF, for higher wavenumbers the EKE dissipation by bottom drag is smaller. Note that the observed elevated Laplacian dissipation at small horizontal wavenumbers (large horizontal scales) implies that anisotropic motions with small vertical scales are being dissipated.

4.5.3 Kinetic energy spectral fluxes: forward and inverse cascades

Forward and inverse energy transfers can be expressed explicitly in terms of the E_k spectral flux

$$\Pi(k) = \int_0^k \mathcal{R}[\{\boldsymbol{u}\}_k \{(\boldsymbol{u}\cdot\nabla)\boldsymbol{u}\}_k^{\diamond}]\, dk'. \tag{4.13}$$

As before the co-spectra are depth integrated, time averaged and are computed as a function of the horizontal wavenumber k_h. Figures 4.9 and 4.10 show $\Pi(k_h)$ for BF and WBF respectively (top right panels). By definition $\Pi(0) = \Pi(k_{h_{max}}) = 0$. Positive/negative slopes ($\partial\Pi/\partial k_h$) indicate wavenumber bands where the flux is divergent/convergent. As a result, regions where $\Pi(k_h) > 0$ denote regions of forward energy transfer and regions where $\Pi(k_h) < 0$ denote regions of inverse energy transfer. Wavenumber bands denoted by a, b and c thus correspond to scales of motion that exhibit forward, inverse and, forward energy transfers respectively. Also displayed are the depth averaged enstrophy ζ^2 (top left panels) and bandpass filtered enstrophies corresponding to wavenumber bands a, b and c (the applied filters excluded narrow wavenumber bands around the zero crossings).

For BF band a is associated with large-scale motions in the deep convection region. Band b corresponds to 'meso-scale' geostrophic eddies which, in agreement with geostrophic turbulence theory, are seen to transfer energy to larger scales. Note that EKE dissipation due to both bottom drag and Laplacian dissipation have maxima ($k_hL_y = 4.2$) near the transition wavenumber ($k_hL_y \sim 3.5$) between regions a and b (figure 4.8 top). Our interpretation is that the maximum in Laplacian EKE dissipation is an energy sink associated with the forward transfer in the deep convection region and the maximum in bottom drag EKE dissipation corresponds to the arrest of the inverse energy cascade associated with the geostrophic eddies. Band c corresponds to the sharp fronts that develop at the edges of the eddies and deep convection filaments and we argue in §4.6 that the flow features in this wavenumber range are associated with loss of balance.

For WBF (figure 4.10) the dynamics associated with wavenumber bands b and c and the corresponding bandpass filtered enstrophies are qualitatively similar to BF. Quantitatively the ratio of forward to inverse energy fluxes is larger than in BF suggesting that loss of balance at these scales is more vigorous in WBF. This is in agreement with the shallower spectral slope of WBF compared with that of BF (figure 4.7). The dynamics in band a are now dominated by the large-scale wind-driven jet. As indicated by figure 4.8 (bottom left) the total kinetic energy at these scales (associated with the zonal jet) is removed by bottom drag (solid red line). As in BF we interpret the maximum bottom drag EKE dissipation (dashed red line in bottom right panel) observed in the transition wavenumber between bands a and b ($k_h L_y = 4.2$) to be associated with the halting of the inverse energy cascade. Laplacian dissipation (dashed black line) is more evenly distributed across wavenumber with a much broader maximum than in BF. We note however, that inferring dynamics solely from spectral fluxes can be misleading, particularly in situations where the energy transfers are non-local in wavenumber space.

4.6 Loss of balance

Figures 4.11 and 4.12 show snapshots of the Richardson number $Ri = N^2/(u_z^2 + v_z^2)$ and the Rossby number $Ro = \zeta/f$ (panels a and b). Positive $O(1)$ values of Ro and Ri are observed in the fronts that develop at the edges of the larger-scale eddies and in the filaments within the deep convection zone. These positive $O(1)$ values indicate regions of ageostrophic motion (*Thomas et al.*, 2008) and correspond spatially to elevated levels of EKE and Laplacian E_k dissipation (panels c and d). The correlation between small-scale dissipation and ageostrophic motions suggests that loss of balance (LOB) is related to a forward energy cascade at frontal scales corresponding to the wavenumber band (c) in figures 4.9 and 4.10.

McWilliams and Yavneh (1998); *McWilliams* (2003); *Molemaker et al.* (2005) suggested criteria for LOB based on the change of type of the balanced equations, from elliptic to hyperbolic, which occurs under any of the following conditions:

i. N^2 changes sign (becomes negative);

ii. The absolute vorticity in isopycnal coordinates $A = f + \zeta$ changes sign (becomes negative for $f > 0$);

iii. Change of sign of $A - |S|$ (becomes negative for $f > 0$), where $S^2 = (u_X - v_Y)^2 + (v_X + u_Y)^2$ is the variance of the horizontal strain rate in isopycnal coordinates.

iv. The Richardson number $Ri < 1/4$.

The physical mechanisms suggested to be associated with these LOB conditions are convective instability (CI) for condition i, inertial instability (INI) or symmetric instability (SI) for condition ii, anticyclonic-ageostrophic instability (AAI) for condition iii (*Müller et al.*, 2005) and classical Kelvin-Helmholtz instability (KHI) for condition iv (*Miles*, 1961; *Howard*, 1961). Note that for flow in hydrostatic balance

$$AN^2 \equiv PV = (\nabla \times \boldsymbol{u})_H \cdot \nabla_H b + (f + \zeta)\frac{\partial b}{\partial z}, \tag{4.14}$$

where PV is the potential vorticity and the subscript H denotes horizontal components. Condition ii can thus be expressed as the change in sign of PV (becomes negative for $f > 0$). As discussed in *Hoskins* (1974); *Bennetts and Hoskins* (1979) if the PV is negative due to the horizontal components, PV_H, (first term on the right hand side of 4.14) the instability is of type SI and if the PV is negative due to the vertical components, PV_V (second term on the right hand side of 4.14) the instability is of type INI. We will thus distinguish between INI and SI when examining condition ii. Note that, according to ii and iii above, if the condition for SI or INI is satisfied, the condition for AAI must also be satisfied because $A - |S| \leq A$.

Other forms of sub-mesoscale instabilities are clearly present in our numerical simulations. Mixed layer instability (MLI) (*Fox-Kemper et al.*, 2008) is an obvious one as indicated by the $O(1)$ Richardson number values in panel a of figures 4.11 and 4.12. MLI is important for the restratification of the mixed layer (*Boccaletti et al.*, 2007) and may develop into finite amplitude mixed layer eddies that can lead to intense frontogenesis, a precondition for LOB. Nevertheless, it is a 'balanced' instability that doesn't lead directly to LOB (*Molemaker et al.*, 2005;

Thomas et al., 2008), i.e. additional instability mechanisms, such as the ones described above, must take place for LOB to occur. The indirect pathways to LOB due to MLI and other balanced phenomena are therefore assumed to be accounted for by the instability mechanisms i-iv above.

(*Capet et al.*, 2008b) have suggested an assessment for the degree of balance based on the departure of the divergence of the horizontal momentum equation (*McWilliams*, 1985) from

$$-\nabla \cdot (\boldsymbol{u}_H \cdot \nabla_H \boldsymbol{u}_H) + f\zeta = \nabla_H^2 p, \tag{4.15}$$

using the parameter

$$\mathcal{E} = \frac{|\nabla \cdot (\boldsymbol{u}_H \cdot \nabla_H \boldsymbol{u}_H) - f\zeta + \nabla_H^2 p|}{|\nabla \cdot (\boldsymbol{u}_H \cdot \nabla_H \boldsymbol{u}_H)| + f|\zeta| + |\nabla_H^2 p| + \mu}, \tag{4.16}$$

where the H subscripts denote horizontal velocities and gradients. The term $\mu = f\zeta_{rms} + (\nabla_H^2 p)_{rms}$ is added to the denominator of (4.16) to exclude situations with locally weak force divergences from being identified as significantly unbalanced. Regions where $\mathcal{E} \approx 0$ are thus considered highly balanced and regions where $\mathcal{E} \approx 1$ are considered highly unbalanced.

Figures 4.13 and 4.14 show surface slices of the conditions for LOB (i-iii) in BF and WBF respectively. The contour plot in figures 4.11 and 4.12 (panel a) shows condition iv for LOB. Regions where $N^2 < 0$ are not plotted in conditions ii-iv. For SI only regions where the $PV < 0$ and $PV_V > 0$ are plotted. Similarly, for INI only regions where the $PV < 0$ and $PV_H > 0$ are plotted.

Qualitatively, in BF, on large-scales LOB occurs due to CI in the deep convection region near $y/H > 12$ (figure 4.13, panel a). At smaller scales, within the deep convection region LOB occurs in some locations due to SI (panel b), and more extensively due to AAI, as indicated by the fine, blue filaments in panel (c). The condition for INI is never satisfied (panel d). The condition KHI is rarely satisfied, as indicated by the hardly visible black contours in figure 4.11 (panel a).

In WBF, LOB due to SI and more so due to AAI occurs over a much greater portion of the domain, extending throughout the thermocline region ($y/H < 5$). The condition for INI is ,again, never satisfied. LOB due to CI is still observed in the deep convection region (now $y/H > 10$) and, in addition, across the jet ($6 < y/H < 9$) at much smaller scales. In both flows, there are regions, especially near fronts, where $PV \sim A > 0$ but $A - |S| < 0$, emphasizing the importance of elevated strain variance in triggering LOB in these locations. The condition KHI is satisfied more extensively as well, primarily in the jet region (contour lines in figure 4.12, panel a). Note, however, that the level of EKE in the jet region is low compared with levels at the thermocline and deep convection regions (figure 4.12, panel c). Visually, regions of unbalanced, non-hydrostatic flow (figure 4.14, panels e and f) correspond spatially to the regions of elevated Laplacian dissipation shown in panel d of figure 4.12. This is consistent with the notion that the forward energy cascade at frontal scales (wavenumber band c in figures 4.9 and 4.10) and the corresponding Laplacian dissipation are dynamically linked with LOB.

Figure 4.15 shows the CDF of (4.16), denoted by $F(\mathcal{E})$, computed based on the full zonal and meridional extents in the range $0.92 \leq z/H \leq 1$ (black) and $0.3 \leq z/H \leq 0.6$ (gray). For both BF and WBF, higher values of $\mathcal{E}$ are more probable near the surface, indicating that LOB is more likely to occur there than in the interior.

Figure 4.16 shows the time- and zonal-mean Laplacian EKE dissipation ($\overline{\epsilon'}$). For BF $\overline{\epsilon'}$ occurs primarily near the surface and is concentrated in the deep convection region. This agrees with figure 4.15 and the fact that LOB primarily occurs within the deep convection region (figure 4.13).

For WBF, $\overline{\epsilon'}$ is most intense near the surface (dashed line) in the thermocline region and to a lesser extent in the deep convection region with a weak signature at depth. Interestingly, little $\overline{\epsilon'}$ is observed in the jet region in agreement with figure 4.12 (panel c). This observation, together with the spatial structure of Laplacian dissipation and LOB instability mechanisms (figure 4.12 (panel d) and 4.14), suggests that LOB leads to the observed forward energy cascade at frontal scales and the consequent small-scale EKE dissipation.

In order to quantify which of the LOB instabilities is most probable we have computed the cumulative distribution functions (CDFs) of each of the LOB conditions (i-iv). In both simulations, the CDFs were computed near the top

$(0.92 \leq z/H \leq 1)$ extending over the full zonal and merdional extents. For WBF we have also computed the CDFs in the same vertical and zonal ranges however limiting the meridional extent to the thermocline region. Table 4.1 summarizes the results of the CDF analysis. Figure 4.17 shows the CDFs for the WBF simulations.

For BF, in agreement with figure 4.13, CI is the most probable instability condition followed by AAI and SI. The conditions for INI and KHI are essentially never satisfied (for INI the probability is, in fact, identically zero).

For WBF, the probability for all conditions increases by an order of magnitude, however the condition for INI is rarely satisfied. CI is the most probable instability condition followed by AAI ,SI and KHI. In the thermocline region however, the probability for AAI exceeds all other conditions by an order of magnitude. The reduction in CI is clear from figure 4.14 (panel a) which shows that $N^2 > 0$ in the thermocline region. CI is thus most probable in the jet and convection regions. SI is a 'forced' instability and can only be sustained if it is maintained by winds and/or buoyancy fluxes (*Thomas and Lee*, 2005). Otherwise, SI will tend to restratify the surface layer and adjust the background flow to a state of marginal stability with $PV \approx 0$, thus damping itself out (*Taylor and Ferrari*, 2009). This is clearly seen in the PDFs of SI (inset in figure 4.17), where the most probable PV values are positive and very close to zero. The reduction in the probability of SI in the thermocline region compared with the entire domain suggests that it is sustained, primarily, by buoyancy loss in the deep convection region. Finally, as depicted in figure 4.12 (panel a, contours), the Richardson number is less than a quarter primarily in the jet region. This explains the reduction in the probability for KHI within the thermocline region.

4.7 Summary and discussion

We have investigated two idealized DNS of channel flow with different external forcing: one forced solely by surface buoyancy fluxes (BF) and the other by both surface buoyancy fluxes and wind stress (WBF). In both experiments there are two possible routes to E_k dissipation: upscale energy cascade leading to dissipation due to bottom drag (the inverse route), and downscale energy cascade, catalyzed by loss of balance (LOB), leading to Laplacian dissipation at small scales (the forward route).

In WBF, a strong barotropic zonal jet is directly forced by the wind stress. As a result, the total kinetic energy reservoir is seven times larger than in BF. Only a fraction of that wind work however, i.e. 'useful wind work' (*Cessi et al.*, 2006), is converted to available potential energy and then drained to excite geostrophic eddies. Consequently, the *eddy* kinetic energy (EKE) reservoir in WBF is only twice that of BF. Furthermore, in both simulations, the amount of EKE dissipation due to Laplacian dissipation at small scales (ϵ') exceeds that due to bottom drag (ϵ'_d), suggesting that the forward route dominates. Interestingly, the ratio between ϵ' and ϵ'_d is about 1.6 in both cases.

Analyses of the Rossby number, Richardson number, violation of the different balance constraints, and of E_k spectral fluxes indicate that ϵ' is directly linked to ageostrophic motions ($Ro \geq 1$, $Ri \leq 1$) that undergo LOB instabilities and exhibit a forward energy cascade. Spatial maps of time and zonal mean EKE dissipation are correlated with regions of LOB at frontal (submeso) scales. As a result, for BF, EKE dissipation is strongest in the upper domain within the deep convection region. For WBF, where the forward energy cascade at submesoscales and the degree of LOB are much larger, EKE dissipation is still strongest near the surface (e.g. in the 'surface layer'), and particularly within the thermocline region. In both cases a CDF of the parameter quantifying the degree of LOB (4.16) indicates that LOB occurs much more frequently in the surface layer than in the interior.

Analyses of the CDFs and spatial maps of the different LOB conditions (§4.6) which lead to the forward energy transfers indicate that, in BF, convective instability (CI) is most probable on the large scales followed by ageostrophic anticyclonic instability (AAI) and to a lesser extent symmetric instability (SI), both of which act at submeso scales. Inertial instability (INI) and Kelvin Helmholts instability (KHI) are essentially never found. All instability mechanisms in this case take place within the deep convection region.

For WBF, the probability for all conditions is increased by an order of magnitude compared with BF. In addition, different instabilities are more/less probable at different meridional regions. In the deep convection region ($10 < y/H$) CI is most probable at large scales, followed by AAI and SI which act at submeso scales. In the jet region ($6 < y/H < 9$), CI, AAI and KHI are all diagnosable, although the amount of EKE there is very low. In the thermocline region ($y/H < 5$), where most of the EKE is found and where most of the EKE dissipation takes place, AAI is the most probable instability, exceeding all others by an order of magnitude. This suggests that AAI is a more prevalent mechanism for LOB at these submeso scales. It is important to note that due to our model output frequency ($\approx 6.5 \times f^{-1}$) we may underestimate the importance of SI which equilibrates on much faster time scales than AAI, thereby wiping itself out as it resets PV to zero. Nevertheless, we argue that it is the lack of external forcing needed to sustain symmetric instability that causes the probability reduction in the thermocline region. The fact that in the deep convection region where buoyancy loss can sustain SI the probabilities are high, supports this argument.

It is noteworthy that a variety of balanced processes, such as mixed layer instability, are important to catalyze frontogenesis and thus precondition the flow to be more susceptible to LOB. Nevertheless, additional instability mechanisms, such as the ones described above, must take place for LOB to occur. Therefore, we have not explicitly analyzed all possible preconditioning processes and assumed LOB to be accounted for by the specific instability mechanisms listed in §4.6.

4.7.1 Oceanographic implications

The numerical challenge of resolving the wide range of scales necessary to capture both forward and inverse energy cascades while computing dissipation accurately is considerable, particularly for an externally forced problem that requires a long time to equilibrate. We therefore had to make compromises in the problem setup. The results of such an exercise are intended to provide insight into the physics of nearly balanced flows that are dynamically similar to oceanic flows and that drive both up- and down-scale energy cascades. Similarity to oceanic flows has been demonstrated by diagnosing the quasi-steady simulations to be nearly hydrostatically balanced and with small characteristic values of the Rossby, Burger and Ekman numbers. Though the nearly adiabatic nature of the WBF simulation and the overall thermal structure in the thermocline region are in reasonable qualitative agreement with flow in the ACC (*Marshall and Speer* 2012 and references therein), the strength of the stratification produced in the simulation is weaker than that observed. This is partially due to processes associated with bathymetric detail, and lateral exchange with other basins that are not included in our model. Whether or not higher stratification would alter the relative transfer rates of the forward and inverse energy cascades by suppressing certain frontal instability mechanism is not clear. In the deep convection zone the dynamics are perhaps more relevant to weakly stratified regions subject to deep convection such as the Labrador Sea (*Jones and Marshall*, 1997) .

The 'useful wind work' concept lead us to propose the non-dimensional parameter S_{EKE} (4.12) to account for the relative contribution of wind to buoyancy forcing to EKE generation. $S_{EKE} \sim 100$ for representative ACC parameters, suggesting that wind forcing is responsible for most of the EKE generation, with buoyancy forcing providing only 1%. In our WBF simulation S_{EKE} is much smaller (~ 6). Figure 4.12 (panels a and b) shows that wind forcing greatly increases/decreases the Ro/Ri values at the fronts. This suggests that higher S_{EKE} values may, in fact, lead to higher/lower values of Ro/Ri, i.e. stronger ageostrophic motions, which will have even greater susceptibility to LOB and forward energy cascade.

One can better relate our simulations to ocean scales based on our approximation $k_d L_y \approx 10$ (see §4.5.2 for detail), meaning that the domain in our simulations contains roughly ten Rossby radii of deformation. This estimate is in agreement with the enstrophy structures associated with bandpass filter (b) in figures 4.9 and 4.10. Our horizontal grid spacing is thus $\approx R_d/100$ which for high latitudes ($R_d = 15 - 25\,km$) would be about $150 - 250\,m$. The vertical resolution needs to be sufficient to resolve the elevated EKE dissipation in the surface 'mixed' layer (dashed line in figure 4.16). In our case, seven grid points were required to properly resolve the surface layer. Note that a low-order finite difference model would require many more grid points than a spectral model to accurately resolve the same flow features. Finally, figure 4.14 (panel e) shows that hydrostatic balance is partially lost in the sharp frontal features that develop at the edge of the barocllinic eddies. This suggests that non-hydrostatic dynamics may be important at these small scales and can affect the energy pathways and LOB instabilities, as has previously been noted by *Mahadevan* (2006). *Magaldi and Haine* (2014), for example, have found the amount of strain variance to be much larger in non-hydrostatic vs. hydrostatic simulations, a feature that would undoubtedly increase the likelihood for AAI.

Figure 4.18 shows horizontal and vertical slices of a local region around a representative front in WBF (rectangular box in figure 4.12). Panel (a) shows the buoyancy field at the front with the predominantly geostrophic flow (solid arrows) in the vicinity of the high pressure, positively buoyant eddy. Panels (c) and (e) show the vertical velocity and EKE dissipation (log-scale) in the same region. EKE dissipation is strongest at the front and correspond well to downwelling regions. Vertical slices of the same fields at $x/H = 5.2$ are shown in panels (b), (d) and (f). As expected from classical theory (*Hoskins and Bretherton*, 1972), ageostrophic circulation with downwelling on the cold side of the front and upwelling on the warm side is observed. The correlation between elevated dissipation and downwelling is found all thorough the thermocline region. The largest values of dissipation however, are confined to the surface layer (dashed line), as expected from figure 4.16.

Although we do not attempt to perform a thorough analysis of all possible mechanisms that may lead to downwelling and small-scale dissipation, our results suggest that AAI may play an important role in this process. Understanding the dynamics associated with AAI is an active area of research (*Menesguen et al.*, 2012). It has been previously identified in high-resolution numerical studies of variable configurations and complexities (*Mahadevan and Tandon*, 2006; *Capet et al.*, 2008b; *Molemaker et al.*, 2010), although its significance as a mechanism leading to LOB was not quantified.

The fact that EKE is dissipated preferentially at small scales near the surface, rather than at large scales via bottom drag suggests that the 'forward route' associated with LOB may provide an important route to dissipation for the kinetic energy stored in the geostrophic eddy field. Although we do not incorporate LOB mechanisms associated with topographic interactions, except as a parametrized bottom drag, the spatial structure of small-scale EKE dissipation suggests that LOB caused by frontal instabilities near the ocean surface can be very efficient, independent of boundary effects.

It has been shown in models (*Chen and Kamenkovich*, 2013) and in observations (*Zajaczkovski and Gille*, 2014) that baroclinic eddies in the ACC are typically generated in localized regions downstream of topography. Whether this localization would affect the degree of LOB or the instability mechanisms leading to it is unclear. Furthermore, *Nikurashin et al.* (2013) have demonstrated in numerical simulations that include realistic Southern Ocean topography that topographically generated internal waves play an important role in the total E_k dissipation. However, because they did not distinguish between mean and eddy fields it is hard to evaluate what fraction of the internal waves was excited by the mean flow and what fraction by the eddies. In the ocean, LOB due to both frontal instability near the surface and internal wave generation near topography may provide a route leading to EKE dissipation. To our knowledge, no study has yet quantified which of the routes dominates.

Other phenomena such as down-front winds (*Thomas and Lee*, 2005) and convection due to the diurnal cycle (*Taylor and Ferrari*, 2010) may trigger or suppress certain frontal instability mechanisms. In addition, inertial gravity waves (*Thomas*, 2012) and Stokes drift associated with the surface gravity wave field (*McWilliams and Fox-Kemper*, 2013) may affect the frontal processes and complicate the picture further. These complexities, however, only emphasize the importance of understanding the physics of fronts, which lie at the cusp between balanced and unbalanced motions near the ocean surface.

4.8 Acknowledgments

RB would like to thank George Carnavalle for useful discussion on spectral fluxes. This work was supported by the National Science Foundation, grant numbers OCE-0926481 and OCE-1259580. XSEDE computing resources at the National Institute of Computational Sciences, University of Tennessee were made available under grant TG-OCE120004. This chapter has been published in: **Barkan, R.**, Winters, K. B., and Llewellyn Smith, S. G. (2015). Energy Cascades and Loss of Balance in a Re-entrant Channel Forced by Wind Stress and Buoyancy Fluxes. *J. Phys. Oceanogr.*, 45, 272-293.

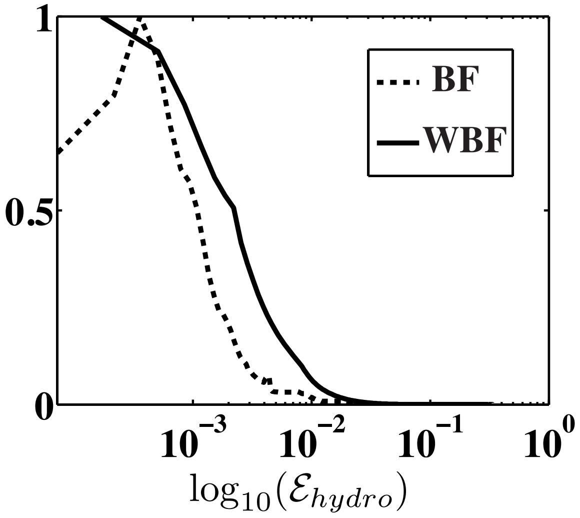

Figure 4.1: PDF of (4.7) for BF (dashed) and WBF (solid) computed over the entire volume. PDF is normalized by the maximal number of observed samples so that values range from 0 to 1.

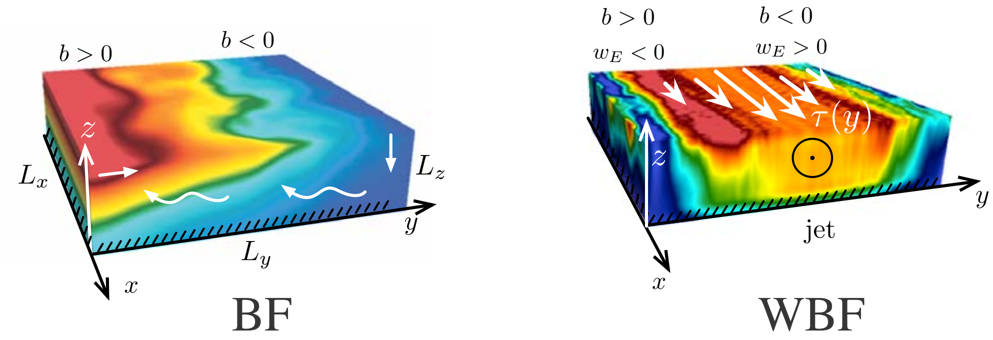

Figure 4.2: Time-averaged buoyancy field for BF (left). Straight white arrows indicate the sense of the buoyancy driven circulation, wavy arrows illustrate the importance of baroclinic eddies in transporting buoyancy meridionally. Time-averaged zonal velocity u for WBF (right). The wind induced barotropic jet is in the positive $\boldsymbol{x}$-direction. $w_E = f^{-1}\hat{\boldsymbol{k}} \cdot \nabla \times \tau_s = -f^{-1}d\tau_s/dy$ indicate the Ekman upwelling and downwelling regions. Note that $f > 0$.

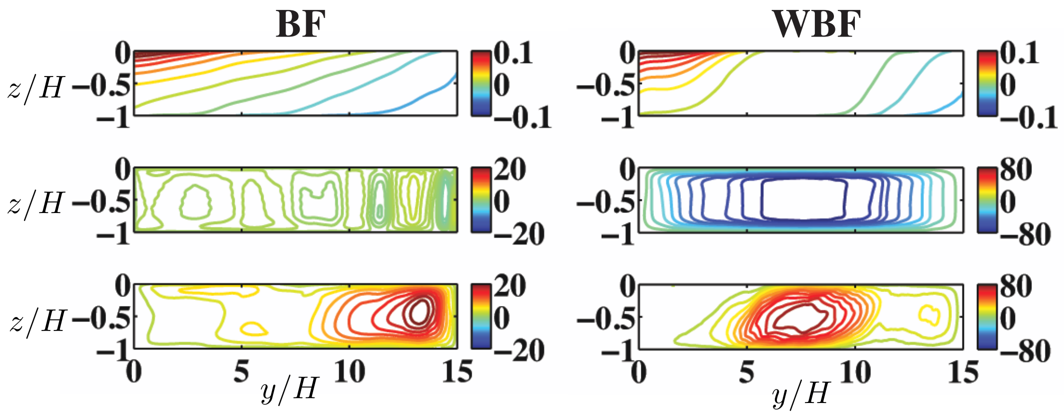

Figure 4.3: Time- and zonal-mean isopycnal height normalized by $B_{max}H/\kappa$ (top), Eulerian-mean streamfunction $\overline{\psi}$ normalized by κ (middle) where $(\overline{v}, \overline{w}) = (-\overline{\psi}_z, \overline{\psi}_y)$, and residual streamfunction ψ_{res} normalized by κ (bottom).

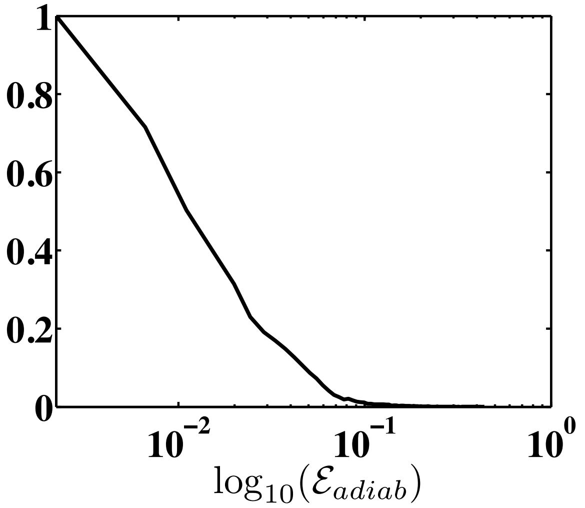

Figure 4.4: PDF of (4.11) for WBF computed in the range $(0.8 < y/H < 14.2\,, 0.06 < z/H < 0.94)$. PDF is normalized by the maximal number of observed samples so that values range from 0 to 1.

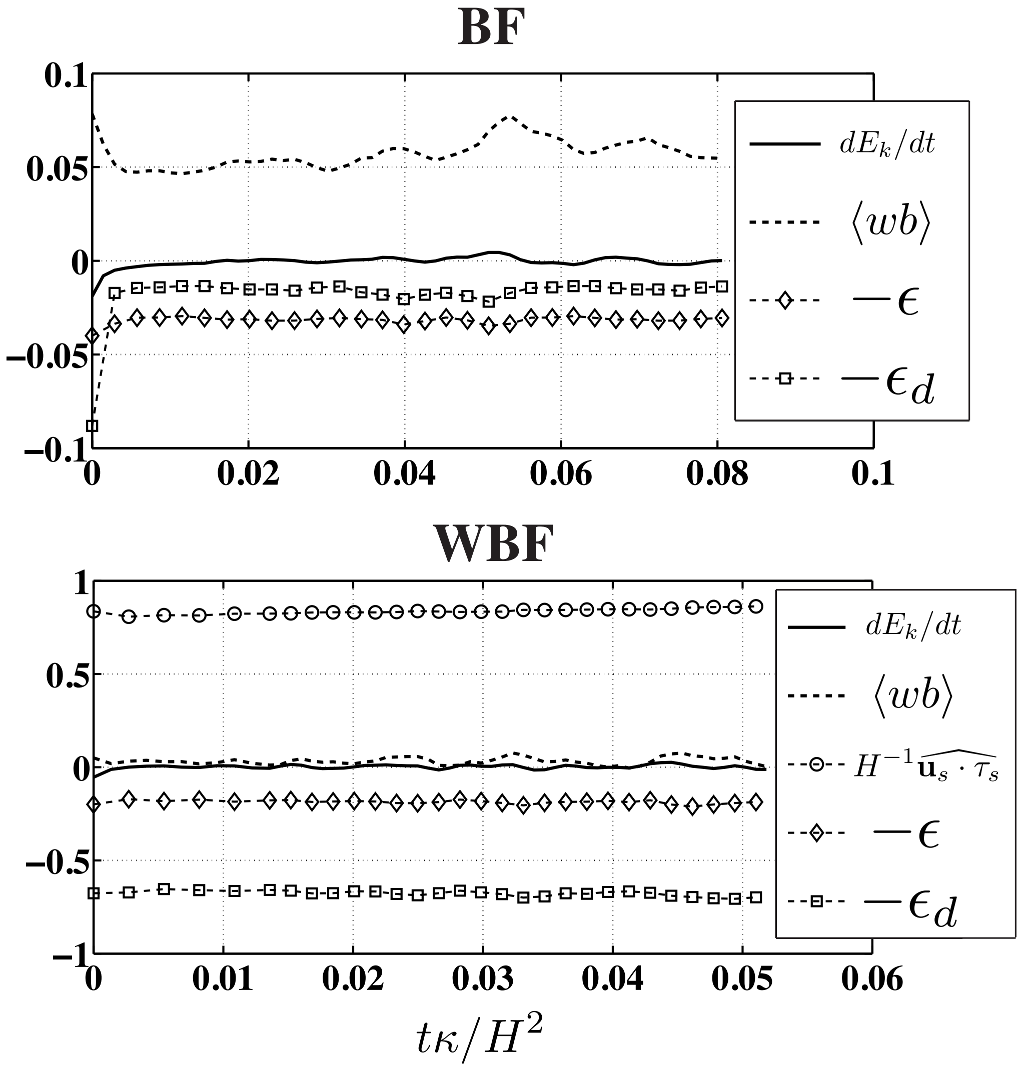

Figure 4.5: The terms in (4.8a) normalized by B_{max}.

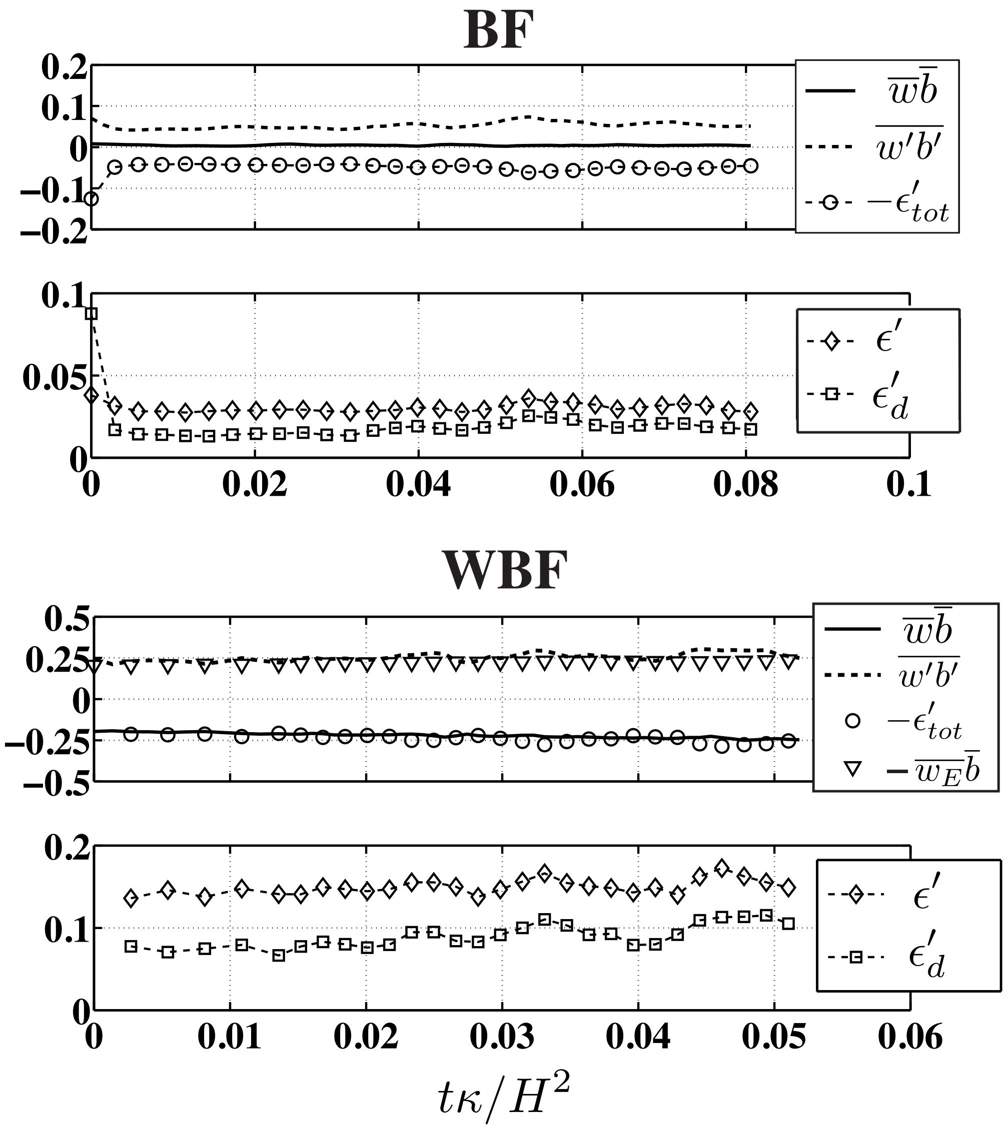

Figure 4.6: The decomposition of $\langle wb\rangle, \epsilon, \epsilon_d$ in (4.8a) into the mean and eddy components. The Ekman velocity is $w_E = -(2f)^{-1}d\tau_s/dy$. $\epsilon'_{tot} = \epsilon' + \epsilon'_d$. All fields are normalized by B_{max}.

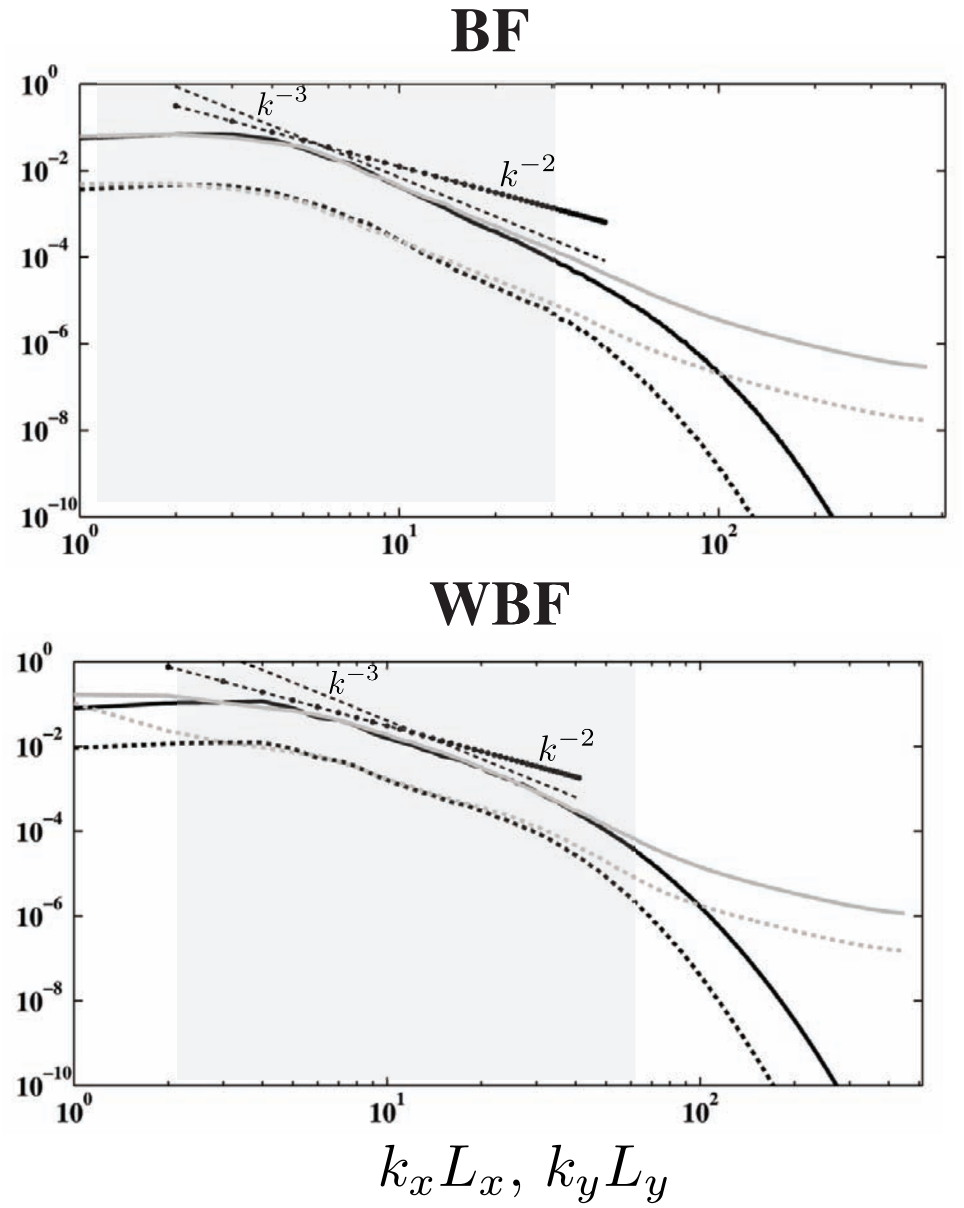

Figure 4.7: $\boldsymbol{y}$ averaged horizontal velocity wavenumber spectra (black) and $\boldsymbol{x}$ averaged horizontal velocity wavenumber spectra (gray) depth-averaged in the ranges $0.85 < z/H < 1$ (solid lines) and $0.3 < z/H < 0.45$ (dashed lines). Straight lines indicate -2 (dot-dashed) and -3 (dashed) spectral slopes. The shaded gray rectangles indicate the wavenumber range where the flow is approximately isotropic. Spectra are normalized by $B_{max}L_y/f$.

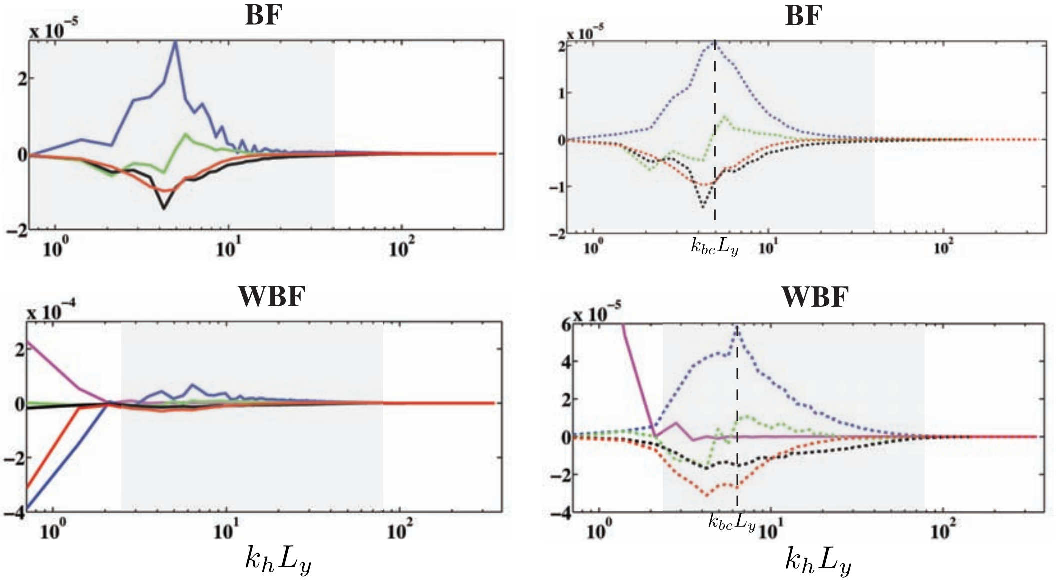

Figure 4.8: E_k balance in spectral space (eq. 4.9). Terms are conversion to/from potential energy (blue), advective flux divergence (green), bottom drag dissipation (red), Laplacian dissipation (black) and wind work (magenta). Solid lines denote total fields and dashed lines denote eddy fields. Shaded gray boxes correspond to the wavenumber range in figure (4.7) where the flow is isotropic. Vertical dashed lines denote the most unstable baroclinic mode. All terms are normalized by $B_{max}L_y^2$.

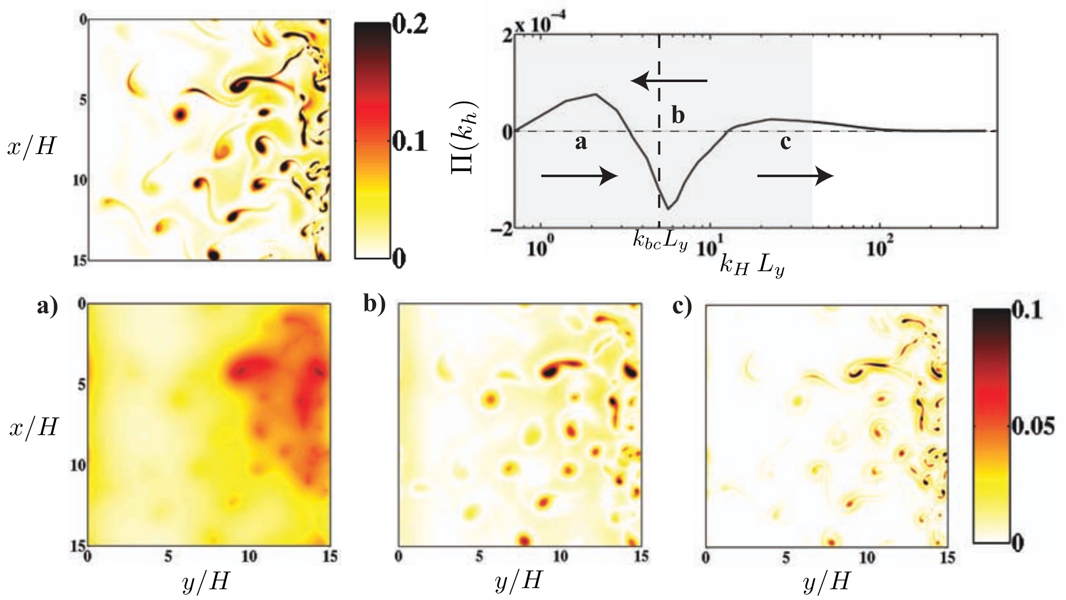

Figure 4.9: Spectral E_k flux $\Pi(k_h)$ (4.13) normalized by B_{max} (top right). Shaded gray boxes correspond to the wavenumber range in figure (4.7) where the flow is isotropic. The vertical dashed line denotes the most unstable baroclinic mode. A snapshot of the depth averaged enstrophy $(\zeta/f)^2$ (top left) where $\zeta \equiv v_x - u_y$ is the vertical vorticity. Panels a, b and c (bottom) correspond to bandpass filtered enstrophy in the horizontal wavenumber range indicated on the spectral flux plot. BF simulation.

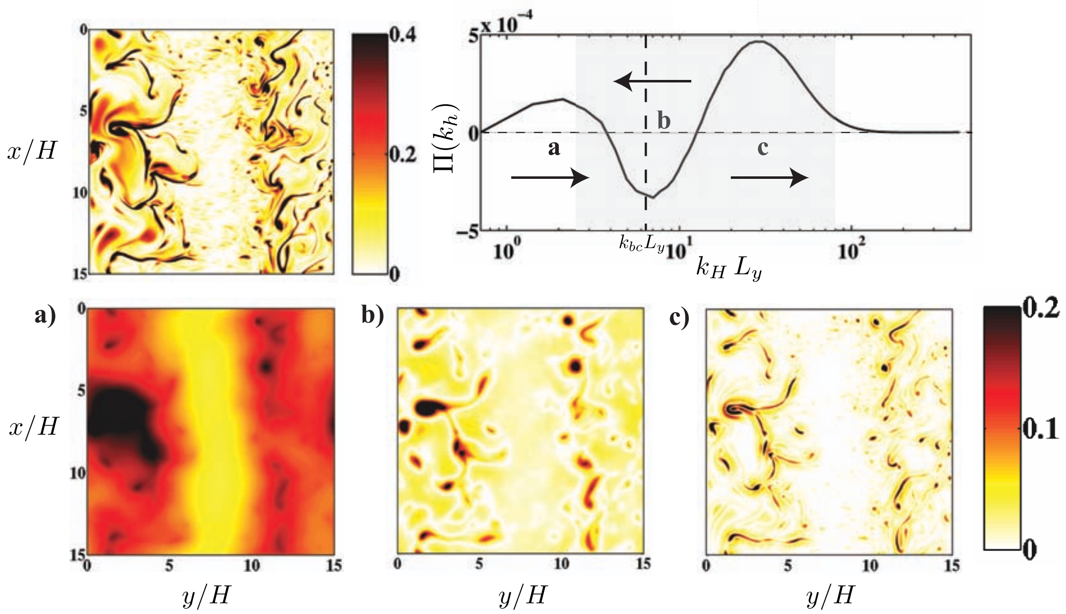

Figure 4.10: Same as figure 4.9 for WBF simulation.

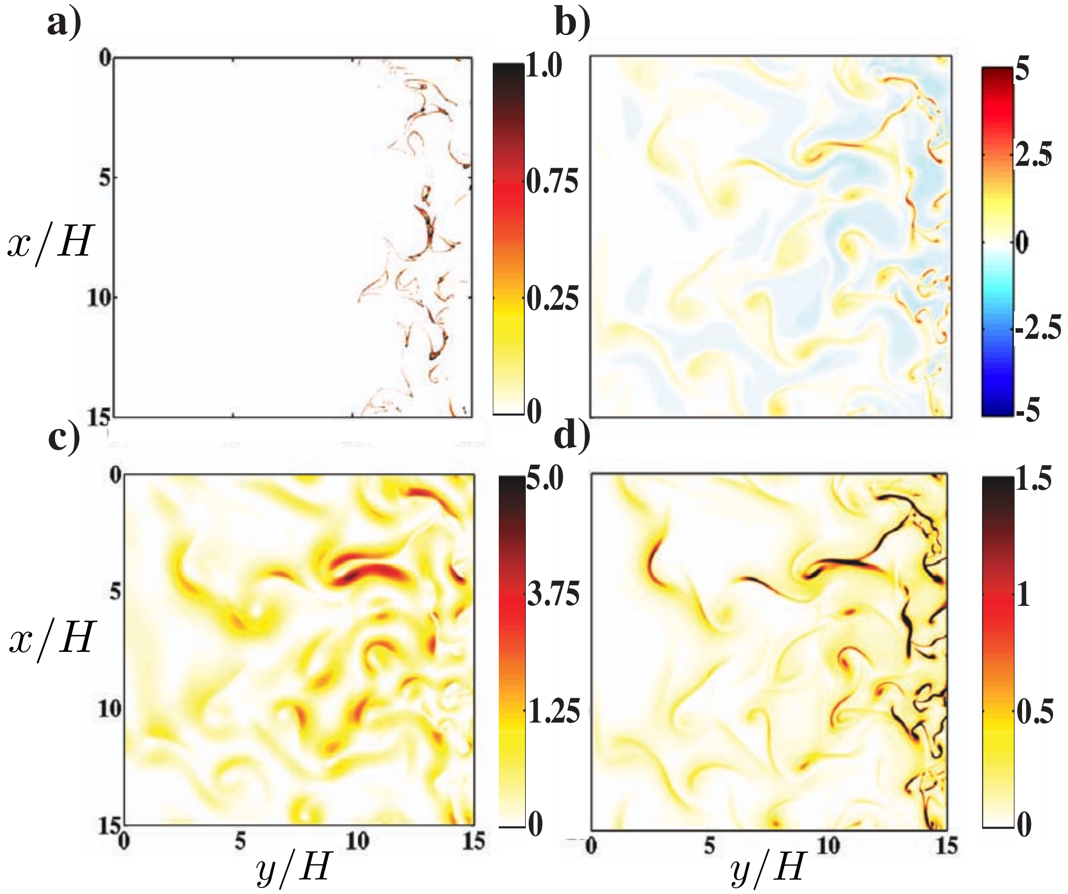

Figure 4.11: a) Richardson number $Ri = N^2/(u_z^2 + v_z^2)$ where colors show the range [0 1] and contours (hardly visible) show the range [0 1/4]. b) Vertical vorticity normalized by f. c) EKE normalized by $(B_{max}H)^{2/3}$. d) E_k dissipation normalized by B_{max}. All fields are computed just below the surface ($z/H = 0.97$) for a representative snapshot of the BF simulation.

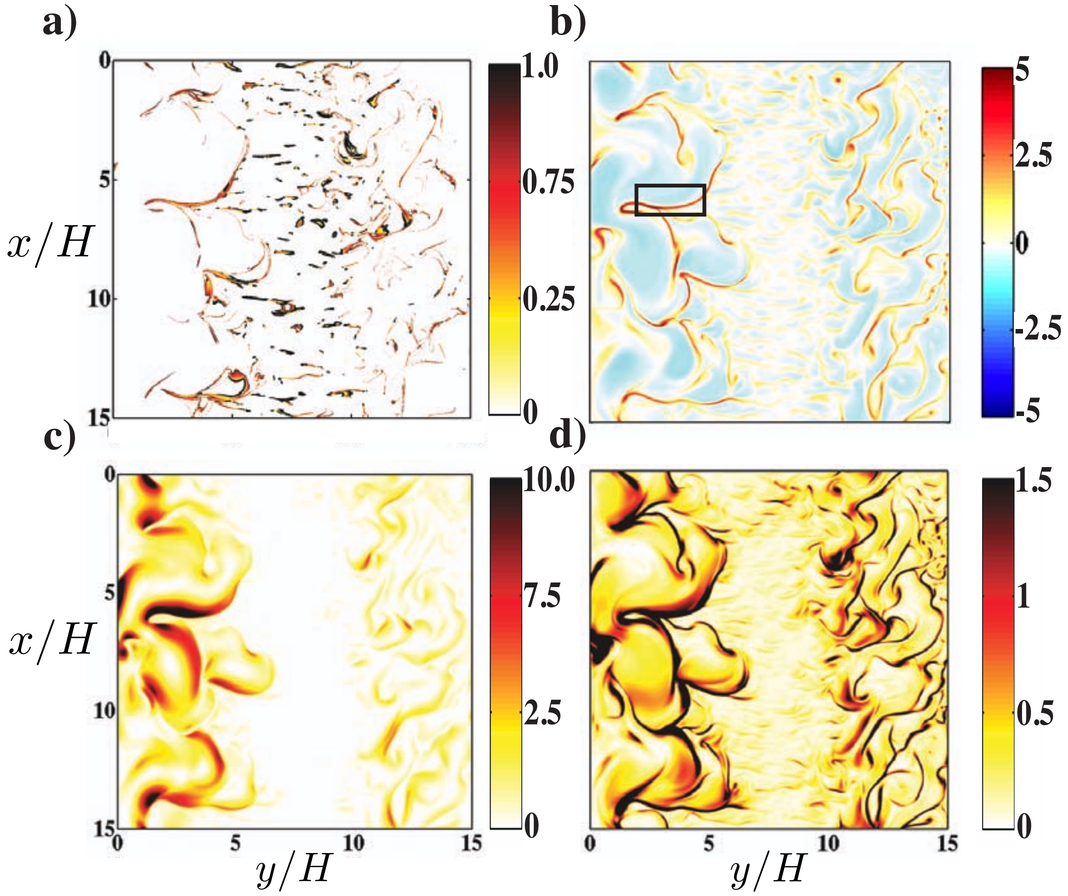

Figure 4.12: Same as figure 4.11 for WBF. Note the different colorbar range in c).

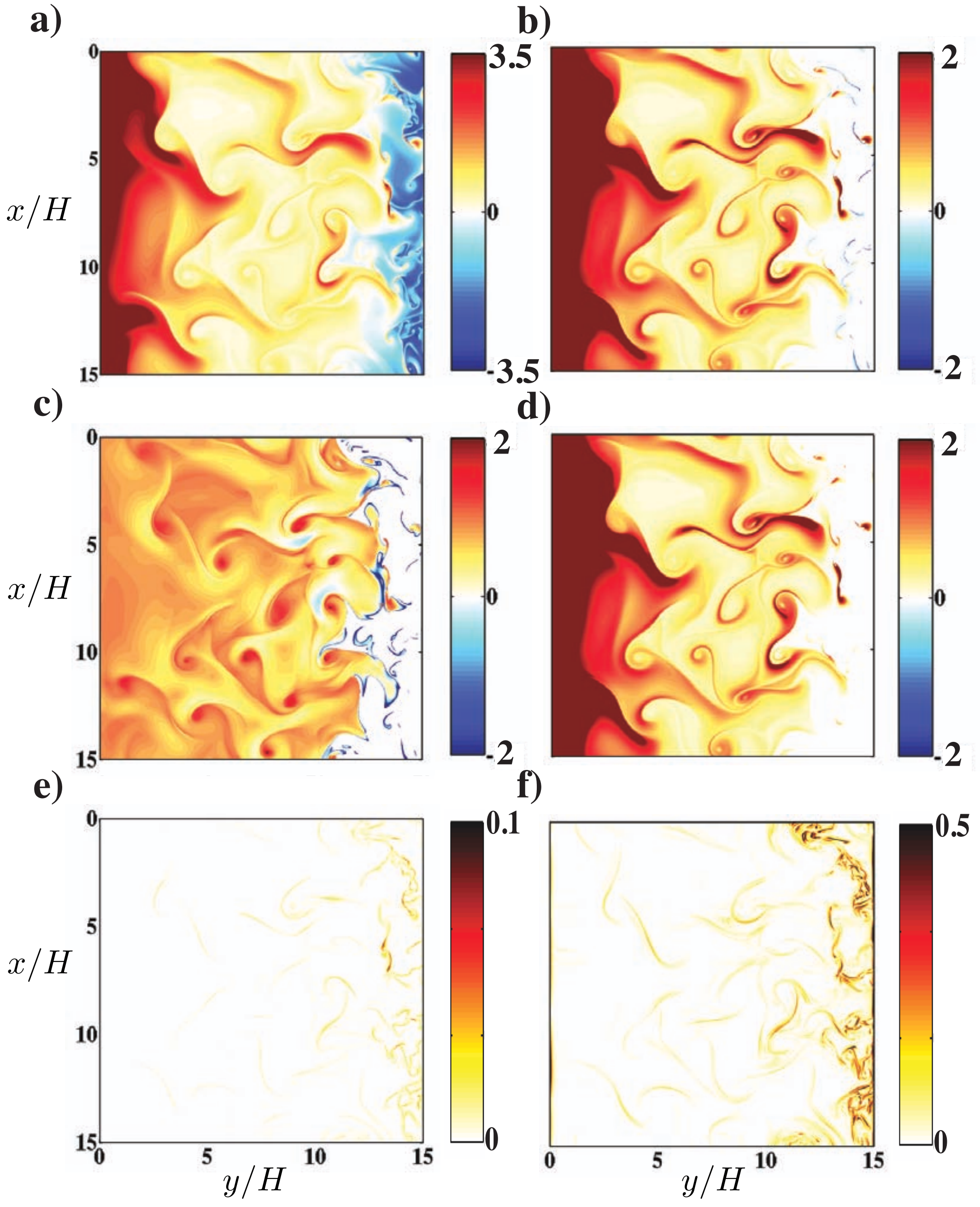

Figure 4.13: Horizontal slices of a) $(N/f)^2$, b) PV/f^3 associated with symmetric instability (see text for detail) , c) $(A-|S|)/f$, d) PV/f^3 associated with inertial instability (see text for detail), e) $\mathcal{E}_{hydro}$ (4.7), f) $\mathcal{E}$ (4.16). Regions where $N^2<0$ are excluded from panels b, c, and d. All fields are computed just below the surface ($z/H=0.97$) for the same snapshot as in figure (4.11) for BF.

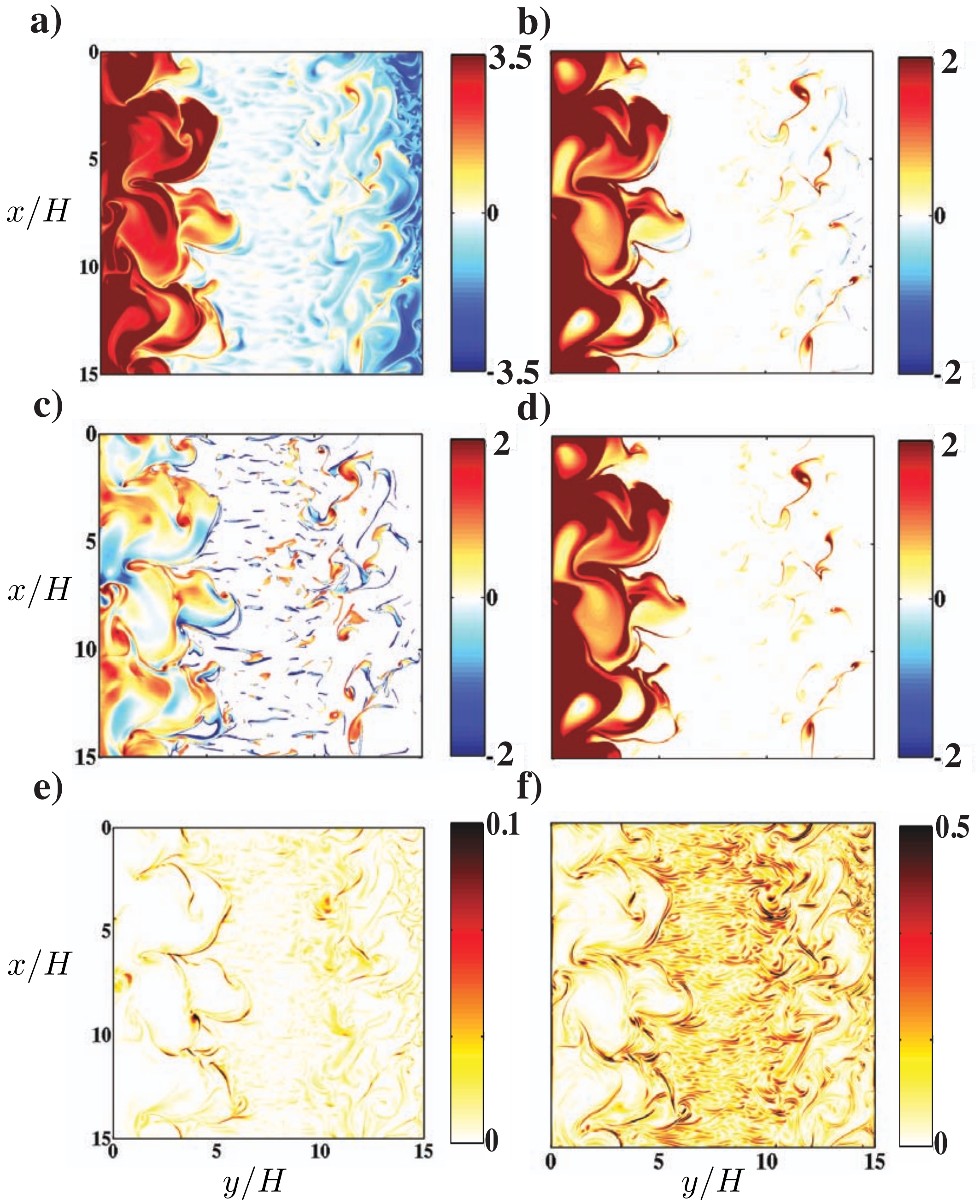

Figure 4.14: Same as figure (4.13) for WBF.

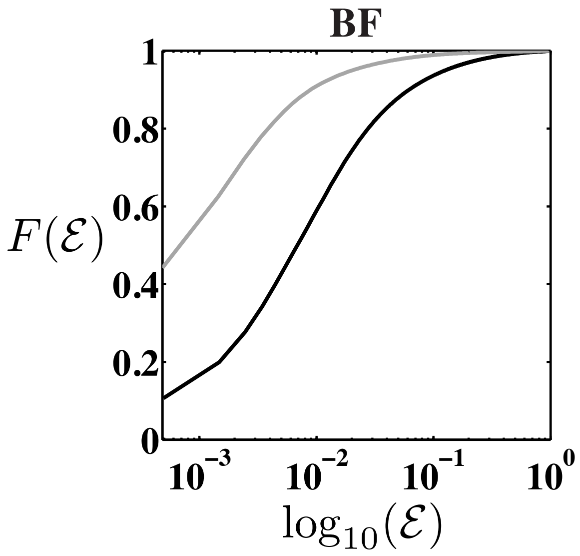

Figure 4.15: CDF of $\mathcal{E}$ (4.16) computed over the entire horizontal area in the range $0.92 \leq z/H \leq 1$ (black) and $0.3 \leq z/H \leq 0.6$ (gray).

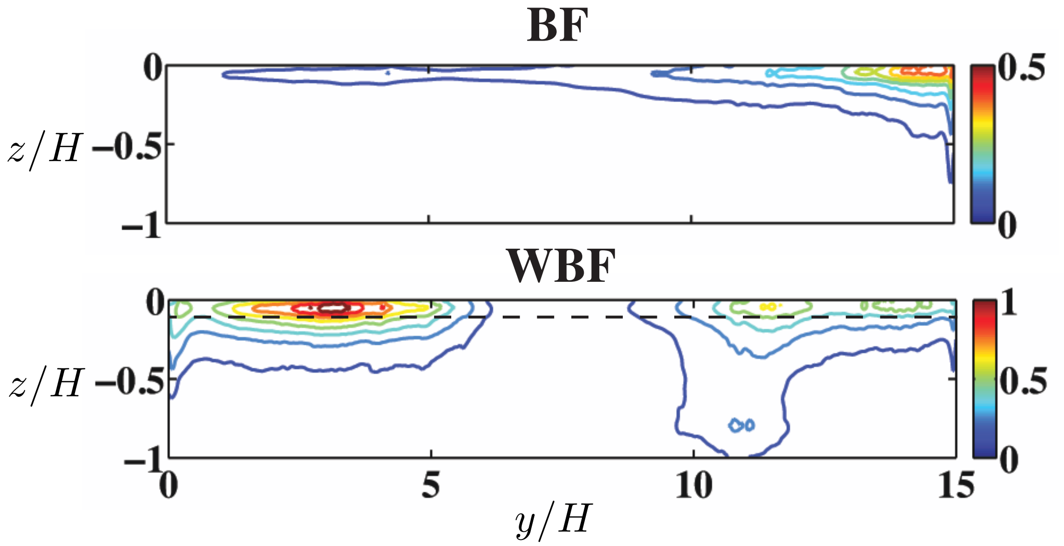

Figure 4.16: Time and $\boldsymbol{x}$ averaged EKE dissipation. The dashed horizontal line in the bottom panel denotes the base of the surface layer. Note the different colorbar ranges.

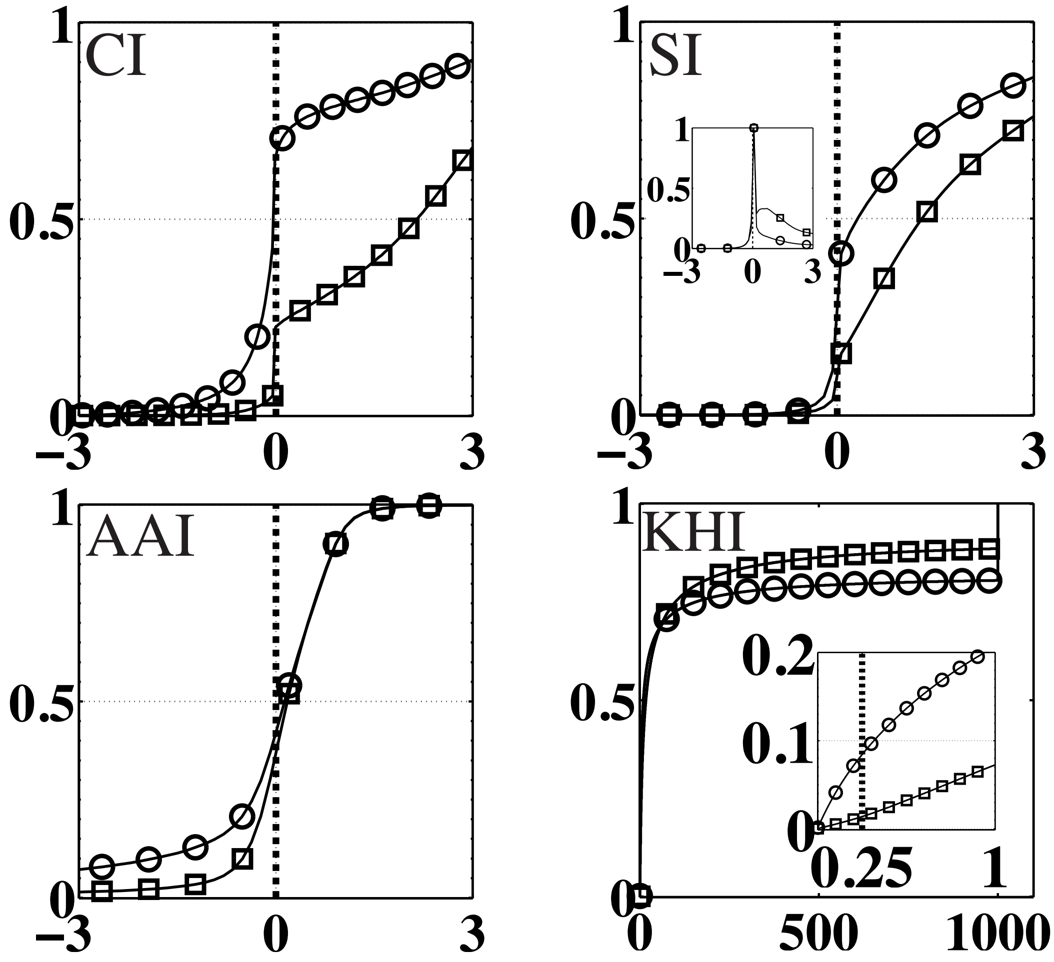

Figure 4.17: CI: CDF of $(N/f)^2$; SI: CDF of PV/f^3 associated with SI; AAI: PDF of $(A - |S|)/f$; KHI: CDF of Ri (see text and table 4.1 for details on how the probabilities were computed).
Circles: CDF computed near the top of the domain ($0.92 \leq z/H \leq 1$). Squares: CDF computed near the top of the domain ($0.92 \leq z/H \leq 1$) in the thermocline region ($0 < y/H < 5$). Note that the bin resolution is much higher than shown by the symbols.
For SI the corresponding PDFs are also shown (inset). For KHI, Ri values greater than a thousand were set to 1000 to decrease the bin resolution needed to resolve the range $0 \leq Ri \leq 1$ (inset). The vertical dashed lines denote the transition values to instability (refer to table 4.1 for actual values). WBF simulation.

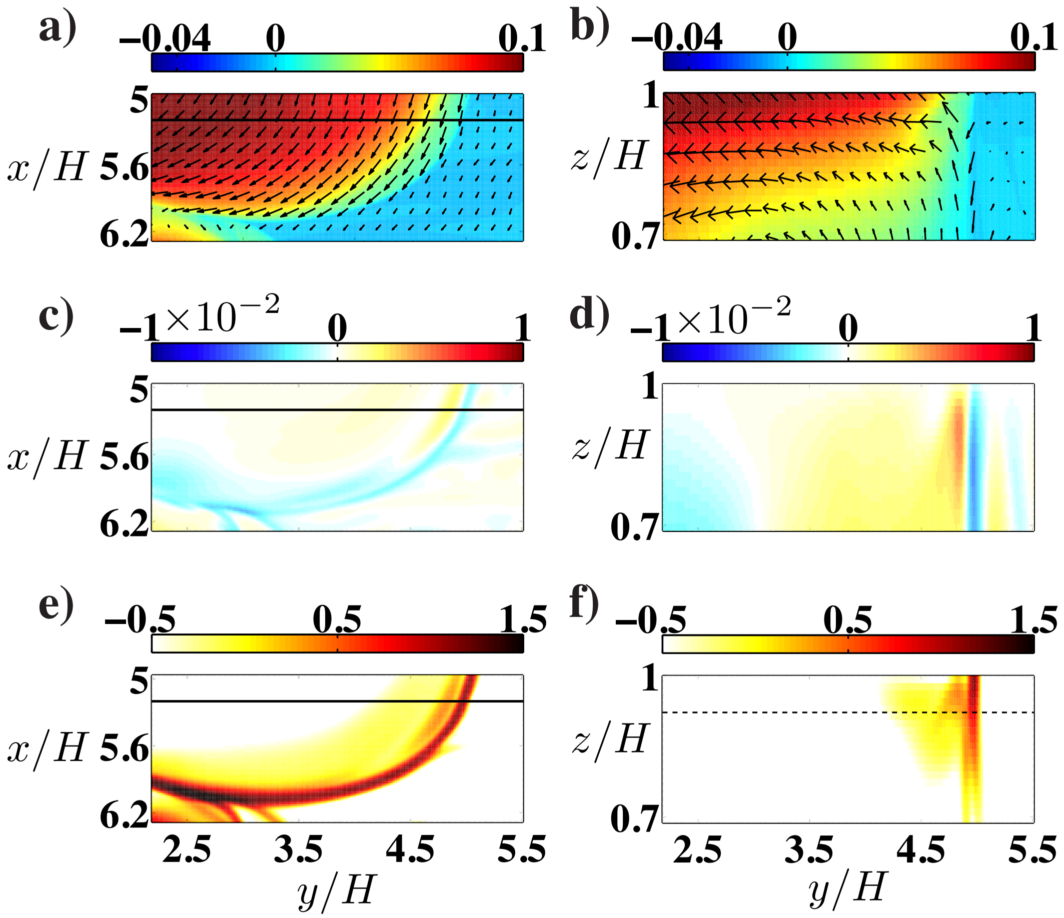

Figure 4.18: A local region (rectangular box in figure 4.12) showing a typical submesoscale frontogenesis in WBF: (a),(b) buoyancy normalized by $B_{max}H/\kappa$. (c),(d) vertical velocity normalized by $B_{max}H/(\kappa f)$. (e),(f) Log of Laplacian EKE dissipation normalized by B_{max}. Left panels are in the (x, y) plane. Right panels are in the (y, z) plane corresponding to the solid lines in (a)-(c). Solid black arrows in (a),(b) denote velocity vectors. Horizontal dashed line in (f) indicates the base of the surface layer (see figure 4.16).

Table 4.1: The probability (P) of conditions i-iv in the BF and WBF simulations. CI: $P(N^2 < 0)$. SI: $P(PV < 0 \cap PV_V > 0 \cap N^2 > 0)$. INI: $P(PV < 0 \cap PV_H > 0 \cap N^2 > 0)$. AAI: $P(A - |S| < 0 \cap N^2 > 0)$. KHI: $P(Ri < 0.25 \cap N^2 > 0)$. PV_H and PV_V are the horizontal and vertical components of the potential vorticity (4.14). CDFs are computed based on the entire zonal and meridional extents in the range $(0.92 \leq z/H \leq 1)$. WBF - thermocline: $(0.92 \leq z/H \leq 1)$ and $(0 < y/H < 5)$.

Instability Type	BF	WBF	WBF - thermocline
CI	0.098	0.648	0.055
SI	0.012	0.113	0.038
INI	0	0.003	0.003
AAI	0.041	0.371	0.303
KHI	0.003	0.084	0.014

Table 4.2: Parameters used in the numerical simulations. For BF $\tau_{max} = 0$.

Symbol	Value	Description
L_x, L_y	$15m$	Domain size
H	$1m$	Domain depth
f	$2.17 \times 10^{-3}\, s^{-1}$	Coriolis parameter
$\rho_0 \tau_{max}$	$2.36 \times 10^{-3}\, Nm^{-2}$	Wind stress magnitude
B_{max}	$1.38 \times 10^{-11}\, m^2 s^{-3}$	Buoyancy-flux magnitude
r	$2.18 \times 10^{-4}\, s^{-1}$	Bottom drag parameter
κ	$2.71 \times 10^{-7}\, m^2 s^{-1}$	Diffusivity
ν	$1.90 \times 10^{-6}\, m^2 s^{-1}$	Viscosity
dx, dy, dz	$0.015\, m$	Grid spacing

4.9 Appendix: Details of the Numerical Simulations

The model equations (4.1) are solved using the non-hydrostatic three dimensional pseudo-spectral model **flow_solve** (*Winters and de la Fuente*, 2012) on an equally spaced grid with $(nz \times ny \times nx) = (65 \times 1025 \times 1024)$ grid points. The grid spacing is $dx = dy = dz$, ensuring that non-hydrostatic motions are completely resolved.

The fixed-flux boundary condition (4.2) is implemented using a body force in (4.1b)

$$\frac{Db}{Dt} + \cdots = \mathcal{F}_{top}\,\mathcal{F}_b(y) \equiv \frac{B}{\sigma_b}\sqrt{\frac{2}{\pi}}\mathrm{e}^{-(z/(\sqrt{2}\sigma_b))^2}\mathcal{F}_b(y), \tag{4.17}$$

where $\sigma_b = dz$, and $\mathcal{F}_b(y)$ is defined in (4.2). In the limit of infinite resolution ($dz \to 0$) the inhomogeneity in the boundary condition is exactly exchanged for inhomogeneity in the governing equation (*Winters and de la Fuente*, 2012) so that (4.17) and (4.2) are identical. The corresponding maximal surface buoyancy flux $B_{max} = 2\int_{-H}^{0}\mathcal{F}_{top}\,dz = 2B$. Note that $\int_0^{L_y}\mathcal{F}_b(y)\,dy = 0$ to ensure mass conservation.

Similarly the surface stress (4.3) is applied as a body force in the zonal momentum equation

$$\frac{Du}{Dt} + \cdots = \mathcal{F}_{ml}(z)\mathcal{F}_\tau(y) \equiv \frac{T}{\sigma_\tau}\sqrt{\frac{2}{\pi}}\mathrm{e}^{-(z/(\sqrt{2}\sigma_\tau))^2}\mathcal{F}_\tau(y), \tag{4.18}$$

where $\mathcal{F}_\tau(y)$ id defined in (4.3). The width $\sigma_\tau = 6dz$ is chosen to distribute the stress induced momentum over a resolvable thin layer near the top of thickness $O(6dz)$, effectively specifying the thickness of the surface boundary layer. The corresponding maximal wind stress $\tau_{max} = (\rho_0)^{-1}\int_{-H}^{0}\mathcal{F}_{ml}\,dz = T/\rho_0$.

The form of the bottom drag $f_b(z)$ in (4.1a) is

$$f_b(z) = \frac{H}{\sigma_\tau}\sqrt{\frac{2}{\pi}}e^{-([z+H]/(\sqrt{2}\sigma_d))^2}, \tag{4.19}$$

where $\sigma_d = 6\,dz$, which smoothly confines the action of the drag term to a thin but well resolved near-bottom layer, thus imposing the thickness of the bottom boundary layer. The magnitude of the bottom drag was set to be $r = \mathcal{C}H^{-1}\sqrt{\nu f/2}$, where the constant $\mathcal{C} = 4.8$ was chosen such that the associated wavenumber $k_r \sim (r^3/E_{k_{flux}})^{1/2}$, with $E_{k_{flux}}$ a representative kinetic energy flux in the simulations, was smaller than the deformation wavenumber k_d and larger than the domain wavenumber $k_{domain} = 1/\sqrt{L_x^2 + L_y^2}$. This ensures that the simulations reach a steady state (figure 4.5) while allowing for a reasonable wavenumber band over which an inverse energy cascade takes place (see figures 4.9, and 4.10). In oceanic simulations, typical linear drag values values are $O(10^{-7} - 10^{-6})$ (*Cessi et al.*, 2006) and the ratio r/f is $O(10^{-3} - 10^{-2})$. In our simulations $r/f \sim O(10^{-1})$. This is because our domain is relatively small which means we must have a larger magnitude of bottom drag in order to halt the inverse cascade before the eddies reach the domain size. Our results should therefore not be sensitive to the choice of bottom drag magnitude as long as the associated wavenumber satisfies $k_{domain} < k_r < k_d$.

In order to verify that all simulated fields were resolved down to the buoyancy variance dissipation scale, the spectra of the second derivative (highest derivative in the equations of motion) of buoyancy in each direction were analyzed. The value of Pr was 7 for both simulations, so the buoyancy field exhibits the smallest scales in these simulations and the second derivative of buoyancy is the hardest computed field to resolve. The decay in the spectra of the second derivative down to the highest wavenumber was the criterion used to ensure sufficient resolution. Table 4.2 provides the dimensional scales of the variables used to set up the simulations. Finally, the Kolmogorov micorscale $l_{ko} = (\nu^3/EKE_{flux})^{1/4}$ based on the EKE flux measured in our WBF simulation (figure 4.6) is $l_{ko} \approx 3\,dy$. This is an indication that dissipative scales are adequately resolved. Furthermore, it illustrates that the forward cascade is reasonably inertial with peak values being $\approx 13 l_{ko}$ (figure 4.10).

Chapter 5

Concluding Remarks

This dissertation examines the forcing mechanisms, energy sources and routes to dissipation of the general oceanic circulation through the use of idealized process-based physics models.

In Chapter 2, we derived a positive definite available potential energy density $\mathcal{E}_a$ in Boussinesq fluid flows that exactly integrates to the available potential energy E_a in eq. (1.7). The derivation follows closely *Lorenz's* (1955) interpretation of available potential energy based on an adiabatic sorting of fluid parcels. $\mathcal{E}_a$ can be used to construct spatial maps of local contributions to E_a for numerical simulations and interpreted in a similar manner to the easily computable spatial maps of kinetic energy density.

In Chapter 3, we examined the extent to which buoyancy forcing alone can drive an energetic overturning circulation and sustain a deep thermocline. We focused on the effects rotation has on the horizontal convection (HC) model described in Section 1.1.1 with respect to the overall thermal structure and buoyancy transport mechanisms, the overturning circulation, and the flow energetics. We showed that the steady state solution of rotating horizontal convection (RHC) is substantially different than that of HC. In RHC geostrophic eddies dominated the vertical and horizontal buoyancy fluxes as well as the energy reservoirs and exchange terms, leading to elevated stratification and a deeper thermal boundary layer compared with non-rotating 'eddy-less' HC. Furthermore, the statistically steady solutions exhibited characteristics of *geostrphic turbulence*, a much better representation of large-scale oceanic flows and emphasized the interactions between deep convection plumes and gesotrophic eddies as means of obtaining deep stratification.

In chapter 4, we explored the kinetic energy pathways and cascades in the RHC model as well as in a model externally forced by wind stress. We chose a flat-bottomed re-entrant channel geometry and a forcing configuration that resembles that of the ACC. The simulated flow was allowed to reach a statistical steady state at which point it exhibited both a forward and an inverse energy cascade. Flow interactions with irregular bathymetry were intentionally excluded so that bottom drag was the sole eddy kinetic energy (EKE) sink of the *boundary route* discussed in Section 1.1.3. We showed that EKE is dissipated preferentially at small scales near the surface via frontal instabilities associated with 'loss of balance' and a forward energy cascade rather than by bottom drag after an inverse energy cascade. This is true both with and without forcing by the wind. These results suggest that submesoscale instabilities near the ocean surface can efficiently catalyze EKE dissipation independent of boundary effects.

The research presented in chapter 4 of this thesis poses more questions than answers in regards to the role submesoscale phenomena may play in the general circulation of the ocean:

i. Most importantly, how much EKE is dissipated globally in the ocean via the *instability route* ?
   If this is indeed a large fraction, it raises doubts regarding the validity and applicability of climate models that neither resolve nor parametrize such submesoscale effects.

ii. Are there certain regions in the oceans that are more susceptible to submesoscale instabilities than others ?
   Should one expect any difference between, say, the ACC and the Gulf Stream ?
   Or, is there a certain universal ratio between upward and downward energy cascade, irrespective of boundary and initial conditions, that depends solely on global flow parameters such as the Reynolds, Rossby and Froude numbers ?

iii. Can ‘loss of balance’ and certain submesoscale instabilities be triggered or suppressed by other physical phenomena such as waves ?

The interaction between mescoscale eddies and surface/internal gravity waves is quite unlikely due to the large temporal and spatial scale speration. On the other hand, the energetic submesoscale features that spontaneously develop as the mesoscale eddies are being stirred around have much smaller spatial scales and much faster temporal scales and presumably a higher likelihood to interact with the surrounding wave fields.

In the near future, we intend to investigate whether an energetic Near-Inertial wave field may augment the forward energy cascade by catalyzing certain mechanism leading to LOB.

Regardless of what the answers to some of these questions may turn out to be, we believe that submesoscale oceanography will lead to the discovery of new interesting physics in the years to come.

Chapter 6

Bibliography

Andrews, D. (1981). A note on potential energy density in a stratified incompressible fluid. *J. Fluid Mech.*, 107:227–236.

Andrews, D. G. and McIntyre, M. E. (1976). Planetary waves in horizontal and vertical shear: The generalized eliassen-palm relation and the mean zonal acceleration. *J. Atmos. sci.*, 33:2031–2048.

Andrews, D. G. and McIntyre, M. E. (1978). Generalized eliassen palm and charney-drazin theorems for waves on axisymmetric mean flows in compressible atmospheres. *J. Atmos. sci.*, 35:175–185.

Barkan, R., Winters, K. B., and Smith, S. G. L. (2013). Rotating horizontal convection. *J. Fluid. Mech.*, 723:556–586.

Beardsley, R. C. and Festa, J. F. (1972). A numerical model of convection driven by a surface stress and non-uniform horizontal heating. *Journal of Physical Oceanography*, 2:444–455.

Bennetts, D. A. and Hoskins, B. J. (1979). Conditional symmetric instability - a possible explanation for frontal rainbands. *Q. J. R. Met. Soc.*, 105:945–962.

Boccaletti, G., Ferrari, R., and Fox-Kemper, B. (2007). Mixed layer instabilities and restratification. *J. Phys. Oceangr.*, 37:2228–2250.

Bryan, K. and Cox, M. D. (1967). A numerical investigation of oceanic general circulation. *Tellus.*, 19:54–80.

Capet, X., McWilliams, J. C., Molemaker, M. J., and Shchepetkin, A. F. (2008a). Mesoscale to submesoscale transition in the california current system. part i: Flow structure, eddy flux, and observational tests. *J. Phys. Ocean.*, 38:29–43.

Capet, X., McWilliams, J. C., Molemaker, M. J., and Shchepetkin, A. F. (2008b). Mesoscale to submesoscale transition in the california current system. part ii: Frontal processes. *J. Phys. Ocean.*, 38:44–64.

Capet, X., McWilliams, J. C., Molemaker, M. J., and Shchepetkin, A. F. (2008c). Mesoscale to submesoscale transition in the california current system. part iii: Energy balance and flux. *J. Phys. Ocean.*, 38:2256–2269.

Cessi, P. (2007). Regimes of thermocline scaling: The interaction of wind stress and surface buoyancy. *J. Phys. Ocean.*, 37:2009–2021.

Cessi, P. and Fantini, M. (2004). The eddy-driven thermocline. *J. Phys. Oceanogr.*, 34:2642–2658.

Cessi, P., Young, W. R., and Polton, J. A. (2006). Control of large-scale heat transport by small-scale mixing. *J. Phys. Ocean.*, 36:1877–1894.

Charney, J. G. (1971). Geostrophic turbulence. *J. Atmos. Sci.*, 28:1087–1095.

Chen, C. and Kamenkovich, I. (2013). Effects of topography on baroclinic instability. *J. Phys. Oceangr.*, 43:790–804.

Chiu-Webster, S., Hinch, E. J., and Lister, J. (2008). Very viscous horizontal convection. *J. Fluid Mech.*, 611:395–426.

Coman, M. A., Griffiths, R. W., and Hughes, G. O. (2006). Sandströms experiments revisited. *J. Mar. Res.*, 64:783–796.

Eady, E. (1947). Long waves and cyclone waves. *Tellus*, 1:33–52.

Ferrari, R. and Wunsch, C. (2009). Ocean Circulation Kinetic Energy - Reservoirs, Sources and Sinks. *Ann. Rev. Fluid Mech.*, 41:253–282.

Ferrari, R. and Wunsch, C. (2010). The distribution of eddy kinetic and potential energies in the global ocean. *Tellus A*, 62:92–108.

Ford, R. (1993). *Gravity wave generation by vortical flows in a rotating frame.* PhD thesis, Cambridge.

Fox-Kemper, B., Ferrari, R., and Hallberg, R. W. (2008). Parameterization of mixed layer eddies. Part I: Theory and diagnosis. *J. Phys. Oceangr.*, 38:1145–1165.

Garabato, A. N., Polzin, K. L., King, B. A., Heywood, K. J., and Visbeck, M. (2004). Widespread intense turbulent mixing in the southern ocean. *Science*, 303:210–213.

Gill, A. E., Green, J. S. A., and Simmons, A. J. (1974). Energy partition in the large - scale ocean circulation and the production of mid - ocean eddies. *Deep - Sea Res.*, 21:499–528.

Hazewinkel, J., Paparella, F., and Young, W. R. (2012). Stressed horizontal convection. *J. Fluid. Mech.*, 692:317–331.

Henning, C. and Vallis, G. K. (2004). The effects of mesoscale eddies on the main subtropical thermocline. *J. Phys. Oceanogr.*, 34:2428–2443.

Hignett, P., Ibbetson, A., and Killworth, P. D. (1981). On rotating thermal convection driven by non - uniform heating from below. *J. Fluid. Mech.*, 109:161–187.

Holliday, D. and McIntyre, M. E. (1981). On potential energy density in an incompressible stratified fluid. *J. Fluid Mech.*, 107:221–225.

Hoskins, B. J. (1974). The role of potential vorticity in symmetric stability and instability. *Q. J. R. Met. Soc.*, 100:480–482.

Hoskins, B. J. and Bretherton, F. (1972). Atmmospheric frontogenesis models: mathematical formulation and solution. *J. Atmos. Sci.*, 29:11–37.

Howard, L. N. (1961). Note on a paper of john w. miles. *J. Fluid Mech.*, 10:509–512.

Hughes, G. O. and Griffiths, R. W. (2008). Horizontal convection. *Annu. Rev. Fluid. Mech.*, 40:185–208.

Hughes, G. O., Hogg, A. M., and Griffiths, R. W. (2009). Available potential energy and irreversible mixing in the meridional overturning circulation. *J. Phys. Oceanogr.*, 39:3130–3146.

Ilicak, M. and Vallis, G. K. (2012). Simulations and scaling of horizontal convection. *Tellus A.*, 64:18377.

Jeffreys, H. (1925). On fluid motions produced by differences of temperature and humidity. *Q. J. R. Met. Soc.*, 51:347–356.

Jones, H. and Marshall, J. (1997). Restratification after deep convection. *J. Phys. Oceangr.*, 27:2276–2287.

Killworth, P. D. and Manins, P. C. (1980). A model of confined thermal convection driven by nonuniform heating from below. *J. Fluid Mech.*, 98:587–607.

King, E. M., Stellmach, S., Noir, J., Hansen, U., and Aurnou, J. M. (2009). Boundary layer control of rotating convection systems. *Nature*, 457:301–304.

Kraichnan, R. H. (1967). Inertial ranges in two-dimensional turbulence. *Physics of Fluids.*, 7:1417–1423.

Lorenz, E. N. (1955). Available potential energy and the maintenance of the general circulation. *Tellus.*, 7:157–167.

Magaldi, M. G. and Haine, T. W. N. (2014). Hydrostatic and non-hydrostatic simulations of dense waters cascading o? a shelf: the east greenland case. *Deep Sea Research*, page submitted.

Mahadevan, A. (2006). Modeling vertical motion at ocean fronts: Are nonhydrostatic effects relevant at submesoscales? *Ocean Model.*, 14:222–240.

Mahadevan, A. and Tandon, A. (2006). An analysis of mechanisms for submesoscale vertical motion at ocean fronts. *Ocean Model.*, 3:241–256.

Marshall, J., Jones, H., Karsten, R., and Wardle, R. (2002). Can eddies set ocean stratification? *J. Phys. Oceanogr.*, 32:26–38.

Marshall, J. and Radko, T. (2003). Residual - mean solutions for the antarctic circumpolar current and its associated overturning circulation. *J. Phys. Ocean.*, 33:2341–2354.

Marshall, J. and Schott, F. (1999). Open-ocean convection: observations, theory and models. *Rev. Geophys.*, 37:1–64.

Marshall, J. and Speer, K. (2012). Closure of the meridional overturning circulation through southern ocean upwelling. *Nat. Geosci.*, 5:171–180.

McWilliams, J. C. (1985). A uniformly valid model spanning the regimes of geostrophic and isotropic, stratified turbulence: Balanced turbulence. *J. Atmos. Sci.*, 42:1773–1774.

McWilliams, J. C. (2003). Diagnostic force balance and its limits. In Fuentes, O. V., Sheinbaum, J., and Ochoa, J., editors, *Nonlinear processes in geophysical fluid dynamics*, pages 287–304. Kluwer.

McWilliams, J. C. and Fox-Kemper, B. (2013). Oceanic wave-balanced surface fronts and filaments. *J. Fluid Mech.*, 730:464–490.

McWilliams, J. C. and Yavneh, I. (1998). Fluctuation growth and instability associated with a singularity in the balanced equations. *Phys. Fluids.*, 10:2587–2596.

Menesguen, C., McWilliams, J. C., and Molemaker, M. (2012). An example of ageostrophic instability in a rotating stratifieded flow. *J. Fluid Mech*, 711:599–619.

Miles, J. W. (1961). On the stability of heterogeneous shear flows. *J. Fluid Mech.*, 10:496–508.

Molemaker, M. J. and McWilliams., J. C. (2010). Local balance and cross-scale flux of available potential energy. *J. Fluid Mech.*, 645:295–314.

Molemaker, M. J., McWilliams, J. C., and Capet, X. (2010). Balanced and unbalanced routes to dissipation in an equilibrated Eday flow. *J. Fluid. Mech.*, 654:35–63.

Molemaker, M. J., McWilliams, J. C., and Yavneh, I. (2005). Baroclinic instability and loss of balance. *J. Phys. Ocean.*, 35:1505–1517.

Mullarney, J. C. Griffiths, R. W. and Hughes, G. O. (2004). Convection driven by differential heating at a horizontal boundary. *J. Fluid Mech.*, 516:181–209.

Müller, P., McWilliams, J. C., and Molemaker, M. J. (2005). Routes to dissipation in the ocean: The 2d/3d turbulence conundrum. In Simpson, H. B. J. and Sündermann, J., editors, *Marine Turbulence*, pages 397–405. Cambridge University Press.

Munk, W. H. (1966). Abyssal recipes. *Deep-Sea Res.*, 13:707–730.

Munk, W. H. and Wunsch, C. (1998). Abyssal recipes ii: energetics of tidal and wind mixing. *Deep-Sea Res.*, 45:1977–2010.

Nikurashin, M. and Vallis, G. A. (2012). A theory of the interhemispheric meridional overturning circulation and associated stratification. *J. Phys. Ocean.*, 42:1652–1667.

Nikurashin, M., Vallis, G. K., and Adcroft, A. (2013). Routes to energy dissipation for geostrophic flows in the southern ocean. *Nature Geoscience*, 6:48–51.

Osborn, T. R. (1980). Estimates of the local-rate of vertical diffusion from dissipation measurements. *J. Phys. Oceanogr.*, 10:8389.

Paparella, F. and Young, W. R. (2002). Horizontal convection is nonturbulent. *J. Fluid Mech.*, 466:205–214.

Park, Y. G. and Whitehead, J. A. (1999). Rotating convection driven by differential bottom heating. *J. Phys. Oceanogr.*, 29:1208–1220.

Peltier, W. and Caulfield, C. (2003). Mixing efficiency in stratified shear flows. *Annu. rev. Fluid. Mech.*, 35:135–167.

Perez-Perez, E., Read, P., and Moroz, I. (2010). Assessing eddy parameterization schemes in a differentially heated rotating annulus experiment. *Ocean Modeling*, 32:118–131.

Plumb, R. and Ferrari, R. (2005). Transformed eulerian-mean theory. part i: nonquasigeostrophic theory for eddies on a zonal-mean flow. *J. Phys. Oceanogr.*, 35:165–174.

Robinson, A. and Stommel, H. (1959). The oceanic thermocline and the associated thermohaline circulation. *Tellus*, 11:295–308.

Rossby, T. (1965). On thermal convection driven by non - uniform heating from below: an experimental study. *Deep - Sea Res.*, 12:9–16.

Rossby, T. (1998). Numerical experiments with a fluid heated non-uniformly from below. *Tellus*, 50:242–257.

Roullet, G. and Klein, P. (2009). Available potential energy diagnosis in a direct numerical simulation of rotating stratified turbulence. *J. Fluid Mech.*, 624:45–55.

Salmon, R. (1980). Baroclinic instability and geostrophic turbulence. *Geophys. Astrophys. Fluid Dyn.*, 15:165–211.

Salmon, R. (1998). Lectures on geophysical fluid dynamics. In *Lectures on geophysical fluid dynamics*. Oxford University Press.

Sandström, J. W. (1908). Dynamishce versuche mit merrwasser. *Ann. Hydrogr. Marit. Meteorol.*, 36:6–23.

Sandström, J. W. (1916). Meteorologische studien im schwedischen hochgebirge. *Göteb. Kungl. Vetensk. Vitterh. Handl.*, 17:1–48.

Scotti, A., Beardsley, R., and Butman, B. (2006). On the interpretation of energy and energy fluxes of nonlinear internal waves: an example from massachusetts bay. *J. Fluid Mech.*, 561:103–112.

Scotti, A. and White, B. (2011). Is horizontal convection really non-turbulent? *Geophys. Res. Lett.*, 38:L21609.

Smith, K. S., Boccaletti, G., Hennings, C. C., Marinov, I., Tam, C. Y., Held, I. M., and Vallis, G. K. (2002). Turbulent diffusion in the geostrophic inverse cascade. *J. Fluid Mech.*, 469:13–48.

Smith, R. (1976). Longitudinal dispersion of a buoyant contaminant in a shallow channel. *J. Fluid Mech.*, 78:677–688.

Stern, M. E. (1975). Ocean circulation physics. In Stern, M. E., editor, *Ocean Circulation Physics*. Academic Press.

Stewart, K. D. (2012). *The effect of sills and mixing on the meridional overturning circulation*. PhD thesis, Australian National University.

Stommel, H., Arons, A. B., and Faller, A. J. (1958). Some examples of stationary planetary flow patterns in bounded basins. *Tellus*, 10:179187.

Stone, P. H. (1966). On non-geostrophic baroclinic instability. *J. Atmos. Sci.*, 23:390–400.

Tailleux, R. (2009). On the energetics of turbulent mixing, irreversible thermodynamics, boussinesq models, and the ocean heat engine controversy. *J. Fluid Mech.*, 638:339–382.

Tailleux, R. and Rouleau, L. (2010). The effect of mechanical stirring on horizontal convection. *Tellus*, 62:138–153.

Taylor, J. and Ferrari, R. (2009). The role of secondary shear instabilities in the equilibration of symmetric instability. *J. Fluid Mech*, 622:103–113.

Taylor, J. and Ferrari, R. (2010). Buoyancy and wind-driven convection at mixed layer density fronts. *J. Phys. Oceangr.*, 40:1222–1242.

Thomas, L. N. (2012). On the effects of frontogenetic strain on symmetric instability and inertia-gravity waves. *J. Fluid Mech.*, 711:620–640.

Thomas, L. N. and Lee, C. M. (2005). Intensification of ocean fronts by down-front winds. *J. Phys. Ocean.*, 35:1086–1102.

Thomas, L. N., Tandon, A., and Mahadevan, A. (2008). Submesoscale processes and dynamics. In Hecht, M. and Hasumi, H., editors, *Ocean Modeling in and Eddying Regime*, volume 177, pages 17–38. AGU Geophysical Monograph Series.

Thompson, A., Heywood, K., Schmidtko, S., and Stewart, A. L. (2014). Observational evidence of an eddy overturning at the antarctic margins. *Nat. Geosci.*, 7:879–884.

Thompson, A. F. and Garabato, C. N. (2014). Equilibration of the antarctic circumpolar current by standing meanders. *J. Phys. Oceang.*, 44:1811–1828.

Vallis, G. K. (2006). Atmospheric and oceanic fluid dynamics. In *Atmospheric and Oceanic Fluid Dynamics*. Cambridge University Press.

Welander, P. (1971). The thermocline problem. *Phil. Tran. R. Soc. Lond. A.*, 270:415–421.

Whalen, C. B., Talley, L. D., and MacKinnon, J. A. (2012). Spatial and temporal variability of global ocean mixing inferred from argo profiles. *Geophys. Res. Lett.*, 39:L18612.

Whitehead, J. A. (1981). Laboratory models of circulation in shallow seas. *Phil. Tran. R. Soc. Lond. A.*, 302:583–595.

Whitehead, J. A. and Wang, W. (2008). A laboratory model of vertical ocean circulation driven by mixing. *J. Phys. Oceanogr.*, 38:1091–1106.

Winters, K. B. and Barkan, R. (2013). Available potential energy density for boussinesq fluid flow. *J. Fluid Mech.*, 714:476–488.

Winters, K. B. and de la Fuente, A. (2012). Modelling rotating stratified flows at laboratory-scale using spectrally-based dns. *Ocean Model.*, 49:47–59.

Winters, K. B., Lombard, P., Riley, J., and D'Asaro, E. A. (1995). Available potential energy and mixing in density stratified fluids. *J. Fluid Mech.*, 289:115–128.

Winters, K. B. and Young, W. R. (2009). Available potential energy and buoyancy variance in horizontal convection. *J. Fluid Mech.*, 629:221–230.

Wolfe, C. L. (2014). Approximations to the ocean's residual overturning circulation in arbitrary tracer coordinates. *Ocean Model.*, 75:20–35.

Wolfe, C. L. and Cessi, P. (2010). What sets the strength of the mid-depth stratification and overturning circulation in eddying ocean models? *J. Phys. Oceanogr.*, 40:1520–1538.

Wood, R. B. and McIntyre, M. E. (2010). A general theorem on angular-momentum changes due to potential vorticity mixing and on potential-energy changes due to buoyancy mixing. *J. Atmos. Sci.*, 67:1261–1273.

Wunsch, C. and Heimbach, P. (2012). The global zonally integrated ocean circulation, 19922006: Seasonal and decadal variability. *J. Phys. Oceangr.*, 39:351–368.

Zajaczkovski, U. and Gille, S. T. (2014). 4-dimensional structure of the southern ocean inferred from argo floats and altimeter data. *J. Geophys. Res.*, page submitted.